UNIVERSIDADE DA CORUÑA

Hybrid organic-inorganic materials with phase transitions for solid-state cooling and solar thermal energy storage

Jorge Salgado Beceiro

Doctoral Thesis

A Coruña 2021

Hybrid organic-inorganic materials with phase transitions for solid-state cooling and solar thermal energy storage

Jorge Salgado Beceiro

Doctoral Thesis UDC | 2021

Directors:

Dra. Socorro Castro García

Dr. Manuel Sánchez Andújar

Departamento de Química, Facultad de Ciencias

Centro de Investigaciones Científicas Avanzadas (CICA)

Programa de doctorado regulado por el RD 99/2011:

Química Fundamental y Medioambiental

Memoria presentada en la Facultad de Ciencias de la Universidade da Coruña por **Jorge Salgado Beceiro** para optar al Grado de Doctor en Química por la Universidade da Coruña.

A Coruña, Octubre 2021

Doctorando

Jorge Salgado Beceiro

Directores

Socorro Castro García   Manuel Sánchez Andújar

Dra. Socorro Castro García, Profesora Titular de Universidad, y **Dr. Manuel Sánchez Andújar**, Profesor Titular de Universidad, pertenecientes al Área de Química Inorgánica de la Universidade da Coruña.

Hacen constar:

Que la presente memoria titulada "Hybrid organic-inorganic materials with phase transitions for solid-state cooling and solar thermal energy storage" ha sido realizada bajo su dirección por el Graduado en Química Jorge Salgado Beceiro en el Área de Química Inorgánica dependiente del Departamento de Química y, habiendo sido concluida, autorizan su presentación para optar al Grado de Doctor en Química con mención de Doctor Internacional.

A Coruña, Octubre 2021

Dra. Socorro Castro García   Dr. Manuel Sánchez Andújar

Adicada a todos quenes facedes que
o fogar sexa cada momento ao voso
lado e non un lugar físico.

Agradecimientos

Son muchas las personas a las que les estoy agradecido por toda la ayuda que me han brindado a lo largo de estos años de tesis.

Las primeras personas a las que agradezco y siempre agradeceré el apoyo en este camino por la ciencia son mis directores, los doctores Socorro Castro García y Manuel Sánchez Andújar. Gracias por adoptarme en este maravilloso grupo y guiarme ante cada obstáculo, siempre dando solución a cada problema y los mejores consejos, tanto humana como científicamente. Es un lujo haber tenido unos directores que siempre estaban ahí para todo. ¡Gracias!

Quiero agradecer al Ministerio de Ciencia, Innovación y Universidades su colaboración en la financiación del proyecto MAT2017-86453-R, que ha permitido la realización de esta tesis doctoral.

Estoy muy agradecido también a todo el grupo de investigación, tanto actual como histórico. El doctor Alberto García Fernández es un gran culpable de mi gusto por la investigación, ha sido otro guía imprescindible en todo este camino, culpable también de alguna resaca tras celebrar algún logro o lamentar un fracaso, pero siempre a mi lado. Otro gran compañero en estos años ha sido su tocayo, Alberto Cuquejo, que en las buenas y en las malas siempre ha estado (además de en cada café que nos tomamos en el CICA). Han venido nuevos y maravillosos compañeros, cuya ayuda ha sido vital para esta tesis. Gracias Javi por estar siempre dispuesto a todo, son pocas las personas que conozco que teniendo tanto trabajo entre manos decidan ayudarte en cualquier momento sin demora, gracias. Gracias también a Nacho por tener siempre una mano que echar y tan buena actitud en todo momento. Estoy muy agradecido también a la Prof. María Antonia Señarís y al Dr. Juan Manuel Bermúdez por toda su ayuda y apoyo en el mundo de la investigación, cada conversación con ellos es una sabia lección sobre cómo proceder ante las adversidades del mismo.

Quiero dar las gracias a toda la gente que forma los equipos técnicos del CICA, SAI y Facultad de Ciencias de la UDC, así como la Unidad de RX de la USC.

Gracias también al Dr. Francisco Rivadulla, del Departamento de Química-Física de la USC.

I want to thank the people from the Department of Materials Science of the Cambridge University, specially Dr. Enric Stern and Dr. Xavier Moya.

I want to thank too Dr. Anthony E. Philips and Dr. Richard Dixey from the School of Physics and Astronomy of the Queen Mary University of London.

I want to thank Dr. Ariel Nonato and Dr. Rosivaldo Xavier Silva for their help and support during their stay at the UDC. It was a pleasure to work together and keep collaborating with such great scientifics.

I am very grateful to Prof. Mari-Ann Einarsrud and Dr. Julian Walker for welcoming me to their group at the NTNU for a pre-doctoral stay. They helped and supported me in every moment of

Resumo

A presente *tese de doutoramento* céntrase no estudo de materiais híbridos orgánicos-inorgánicos con transicións de fase para aplicacións de refrixeración en estado sólido e almacenamento de enerxía.

Dada a importancia de substituír os compostos perigosos, tóxicos e/ou contaminantes empregados en ditas aplicacións, este traballo céntrase na selección, deseño e síntese de materiais con unidades orgánicas e inorgánicas que poidan proporcionar transicións de fase altamente enerxéticas e outras propiedades funcionais, fundamentais para sistemas enerxéticos como a refrixeración en estado sólido e o almacenamento de enerxía. Estudouse a estrutura química e as propiedades funcionais (calóricas, eléctricas e magnéticas) para analizar o comportamento dos materiais e contemplar opcións innovadoras dada a multi-sensibilidade a diferentes estímulos (temperatura, presión ou campo eléctrico).

Como resultado desta investigación, a perovskita híbrida $[(CH_3)_4N]Mn(N_3)_3$ e os cristais plásticos híbridos $[(CH_3)_3(CH_2Cl)N]FeCl_4$, $[(CH_3)_3(CH_2Cl)N]GaCl_4$ e $[(CH_3)_3S]FeCl_4$ reportanse como materiais barocalóricos prometedores para aplaciós de refrixeración en estado sólido. Ademais, $[(CH_3)_3(CH_2Cl)N]GaCl_4$ e $[(CH_3)_3S]FeCl_4$, que son materiais novos reportados nesta *tese*, presentan propiedades calóricas, eléctricas e magnéticas moi interesantes e axeitadas para aplicacións de almacenamento de enerxía térmica solar e a posibilidade de combinalas con almacenamento de enerxía eléctrica para sistemas multi-funcionais. Os resultados aquí presentados son unha aportación para o desenvolvemento de sistemas sostibles e respectuosos co medio ambiente para o uso e almacenamento de enerxía.

Resumen

La presente *tesis doctoral* se centra en el estudio de materiales híbridos orgánicos-inorgánicos con transiciones de fase para aplicaciones de refrigeración en estado sólido y almacenamiento de energía.

Dada la importancia de sustituir los compuestos peligrosos, tóxicos y/o contaminantes empleados en tales aplicaciones, este trabajo se centra en la selección, diseño y síntesis de materiales con unidades orgánicas e inorgánicas que puedan proporcionar transiciones de fase altamente energéticas y otras propiedades funcionales, fundamentales para sistemas energéticos como la refrigeración en estado sólido y el almacenamiento de energía. Se estudió la estructura química y las propiedades funcionales (calóricas, eléctricas y magnéticas) para analizar el comportamiento de los materiales y contemplar opciones innovadoras dada la multi-sensibilidad a diferentes estímulos (temperatura, presión o campo eléctrico).

Como resultado de esta investigación, la perovskita híbrida $[(CH_3)_4N]Mn(N_3)_3$ y los cristales plásticos híbridos $[(CH_3)_3(CH_2Cl)N]FeCl_4$, $[(CH_3)_3(CH_2Cl)N]GaCl_4$ y $[(CH_3)_3S]FeCl_4$ se reportan

como materiales barocalóricos prometedores para aplicaciones de refrigeración en estado sólido. Además, $[(CH_3)_3(CH_2Cl)N]GaCl_4$ y $[(CH_3)_3S]FeCl_4$, que son materiales nuevos reportados en esta *tesis*, presentan propiedades calóricas, eléctricas y magnéticas muy interesantes y adecuadas para aplicaciones de almacenamiento de energía térmica solar y la posibilidad de combinarlas con almacenamiento de energía eléctrica para sistemas multi-funcionales. Los resultados aquí presentados son una aportación para el desarrollo de sistemas sostenibles y respetuosos con el medio ambiente para el uso y almacenamiento de energía.

Abstract

The present *Ph.D. Thesis* is focused on the study of hybrid organic-inorganic materials with phase transitions for solid-state cooling and energy storage applications.

Given the importance of substituting the dangerous, toxic and/or polluting compounds employed in such applications, this work is centered in the selection, design and synthesis of materials with organic and inorganic units that can provide high-energetic phase transitions and other functional properties, fundamental for energy systems such as solid-state cooling and energy storage. The chemical structure and functional properties (caloric, electric and magnetic) were studied to analyze the performance of the materials and contemplate innovative options given by the multi-sensitivity to different stimuli (temperature, pressure or electric field).

As result of this research, the hybrid perovskite $[(CH_3)_4N]Mn(N_3)_3$ and the hybrid plastic crystals $[(CH_3)_3(CH_2Cl)N]FeCl_4$, $[(CH_3)_3(CH_2Cl)N]GaCl_4$ and $[(CH_3)_3S]FeCl_4$ are reported as promising barocaloric materials for solid-state cooling. Furthermore, $[(CH_3)_3(CH_2Cl)N]GaCl_4$ and $[(CH_3)_3S]FeCl_4$, which are new materials reported in this *thesis*, revealed very interesting caloric, electric and magnetic properties suitable for solar thermal energy storage applications and the possibility of combining them with electrical energy storage for multi-functional systems. The results here presented are an input to the development of sustainable and environmentally-friendly systems for the use and storage of energy.

Index

Preface

The current management of energy is ruining the planet.

There is an undeniable evidence that our society's way of life, especially during the last century, is having a considerable impact on the planet on which we live. Many of the changes we are seeing in the atmosphere are directly related to society's use of energy. However, the problem is not the use of energy, but the systems employed to generate and store it. Recent reports of the International Energy Agency set the current heating and cooling applications as a ~40% and ~8% (respectively) of the global contributions of CO_2 emissions.[1,2] Temperature control is always one of the most important challenges in several technological activities. A recent example of this is the commercial battle for the vaccine against the COVID-19, whose cold chain represents around the 80% of the vaccination costs.[3]

More generally, the global demand for heating, ventilation, air conditioning, and refrigeration (HVAC&R) in residential and industrial settings is growing rapidly. Most of these systems employ technologies such as electric resistances, gas-combustion or vapor-compression. Electric resistances are very expensive; and gas-combustion and vapor-compression involve the use of greenhouse, toxic and/or flammable gases with high risks of leakage and security for the users. On this context, it was recently reported by the International Renewable Energy Agency that renewable power systems, considering heat and cold storage systems, can provide ~90% of the reduction in energy-related CO_2 emissions by 2050.[4]

In the last years, solid-solid phase change materials (SS-PCMs) have been studied as an ecologic alternative for energy conversion and/or storage in HVAC&R systems. SS-PCMs are compounds that exhibit reversible phase transitions from a solid-state phase to a different solid-state phase, induced by an external stimulus (temperature, pressure, electric and/or magnetic field). These phase transitions involve thermal changes that can be employed in refrigeration, heating or thermal energy storage.[5,6]

In this context, it is highlighted the importance of studying SS-PCMs in depth, both in terms of their physico-chemical and functional properties. Up to date, the main studied materials for HVAC&R applications are of organic nature.[7,8] However, organic materials that have been demonstrated to have properties suitable for energy applications have some disadvantages such as low decomposition points, flammability or low reversibility for cooling applications. These drawbacks can be avoided by combining organic and inorganic parts in the so-called hybrid organic-inorganic materials. The presence of inorganic units, such as transition metals, can give more thermal stability and provide new functional properties (dielectric, magnetic, optical, etc.).[9] Interestingly, these properties could be combined in multi-sensitive materials, making these compounds multi-functional for a wide range of applications.

Where to start?

The research group where this doctoral thesis was carried out has a wide experience in Solid State Chemistry and Materials, with decades of experience in the study of materials based on the perovskite structure, both metallic solids and organic-inorganic hybrid perovskites. Those organic-inorganic hybrid perovskites, with a general formula ABX_3 combine organic molecules (part A)

with metallic atoms (part B) linked by organic/inorganic ligands (part X). Just before this thesis was started, the group discovered the first barocaloric hybrid perovskite, [TPrA][Mn(dca)$_3$][10] (TPrA: tetra-propylammonium, dca: dicyanamide), and reported the great potential of this family for solid-state refrigeration.[11]

In this context, the present doctoral thesis started by studying, as **first objective**, the barocaloric properties of different hybrid perovskites (some new, and others already known but studied for other purposes).

During the progress of our investigations, another interesting type of compounds was reported by other groups as great barocaloric materials: the so-called organic plastic crystals (PCs) like neopentylglycol.[12] PCs are a group of compounds characterized by undergoing phase transitions from a solid state to a PC state before melting, keeping the crystallinity but with orientational and conformational degrees of freedom.[13] Then, taking advantage of the experience of our group in hybrid materials, it was decided to study the barocaloric effect of hybrid organic-inorganic PCs, which have never been studied for solid-state cooling, and it was proposed as the **second objective** of the thesis. In those hybrid PCs, formed by organic cations and inorganic anions, the presence of metallic atoms can always provide functional properties such as dielectric, ferroelectric and/or magnetic switching. Furthermore, hybrid PCs were reported as promising TES materials, due to the energetic phase transitions they can undergo.[14] So, as **third objective** of this doctoral thesis, hybrid PCs were also studied for TES applications, including the analysis of some of their additional functional properties, such as dielectric, ferroelectric and magnetic behavior.

With this background, the main objective of this doctoral thesis can be summarized as the **design, synthesis and characterization of hybrid organic-inorganic materials for solid-state cooling and energy storage applications**.

The memory of this work was organized taking into account all the obtained results for the marked objectives and has the following order:

Chapter 1 contains an introductory section about the solid-state cooling technology and thermal energy storage, and also about the hybrid materials and the phase changes, important for both technologies.

Chapters 2, 3 and 4 are presented as research publications of the reported works. Chapter 5 has the same format, but it is not published yet.

Chapter 2 covers the study of a barocaloric hybrid perovskite, [(CH$_3$)$_4$N]Mn(N$_3$)$_3$, for solid-state cooling.

In **Chapter 3,** it is presented a new hybrid plastic crystal, [(CH$_3$)$_3$S]FeCl$_4$, with its structural characterization and the study of its properties for thermal and electric energy storage, in addition to its magnetic behavior.

Chapter 4 contains the barocaloric study of the [(CH$_3$)$_3$S]FeCl$_4$ and [(CH$_3$)$_3$(CH$_2$Cl)N]FeCl$_4$ plastic crystals for solid-state cooling.

Chapter 5 contains a complete study of the hybrid [(CH$_3$)$_3$(CH$_2$Cl)N]GaCl$_4$ plastic crystal for solid-state cooling, and also for thermal energy storage; its dielectric properties and its response to an electric field were also studied and reported in this chapter.

Chapter 6 contains the general conclusions of the work presented in this *doctoral thesis*.

Annexe I contains a summary of the *Ph.D. Thesis* in Spanish.

Annexe II contains the patents, publications in scientific journals, communications in specialized events and collaborations during this research.

This doctoral thesis was elaborated within the **Environmental and Fundamental Chemistry Ph.D. Program** of the **University of A Coruña (UDC)**. The investigation was carried out with a research contract with the project MAT2017-86453-R (Ministerio de Ciencia, Innovación y Universidades + Fondos FEDER). Most of the work was carried out at the Advanced Scientific Research Center (*Centro de Investigaciones Científicas Avanzadas*-CICA), within the *Química Molecular y de Materiales* (QUIMOLMAT) research group of the UDC. Part of this thesis was developed in collaboration with the *Functional Materials and Materials Chemistry* (FACET) group of the Norges Teknisk-Naturvitenskaplige Universitet (NTNU) of Trondheim, Norway during a 3-month predoctoral stay from March 1st to June 1st 2021. It was a virtual stay, in the context of a special arrangement for the emergency due to de COVID-19 situation that occurred during the corresponding months in Norway and Spain.

References

1   Heating - Fuels & Technologies - IEA, https://www.iea.org/fuels-and-technologies/heating, (accessed 14 July 2021).

2   Cooling - Fuels & Technologies - IEA, https://www.iea.org/fuels-and-technologies/cooling, (accessed 14 July 2021).

3   J. Wang, Y. Peng, H. Xu, Z. Cui and R. O. Williams, *AAPS PharmSciTech*, 2020, 21, 1–12.

4   IRENA, *Innovation Outlook: Thermal Energy Storage*, 2020.

5   D. Boldrin, *Appl. Phys. Lett.*, 2021, 118, 170502.

6   K. Pielichowska and K. Pielichowski, *Prog. Mater. Sci.*, 2014, 65, 67–123.

7   A. Aznar, P. Lloveras, M. Barrio, P. Negrier, A. Planes, L. Mañosa, N. Mathur, X. Moya and J. L. Tamarit, *J. Mater. Chem. A*, 2020, 8, 639–647.

8   R. K. Sharma, P. Ganesan, V. V Tyagi, H. S. C. Metselaar and S. C. Sandaran, *Energy Convers. Manag.*, 2015, 95, 193–228.

9   W. Li, Z. Wang, F. Deschler, S. Gao, R. H. Friend and A. K. Cheetham, *Nat. Rev. Mater.*, 2017, 2, 16099.

10   J. M. Bermúdez-García, M. Sánchez-Andújar, S. Castro-García, J. López-Beceiro, R. Artiaga and M. A. Señarís-Rodríguez, *Nat. Commun.*, 2017, 8, 15715.

11   J. M. Bermúdez-García, M. Sánchez-Andújar and M. A. Señarís-Rodríguez, *J. Phys. Chem. Lett.*, 2017, 8, 4419–4423.

12   P. Lloveras, A. Aznar, M. Barrio, P. Negrier, C. Popescu, A. Planes, L. Mañosa, A. Avramenko, N. D. Mathur, X. Moya and J. Tamarit, *Nat. Commun.*, 2019, 10, 1803.

13   J. Timmermans, *J. Phys. Chem. Solids*, 1961, 18, 1–8.

14   D. Li, X. M. Zhao, H. X. Zhao, L. S. Long and L. S. Zheng, *Inorg. Chem.*, 2019, 58, 655–662.

Chapter 1

Introduction

Chapter 1

Index

1.1. Phase change materials for solid-state cooling

1.1.1. Cooling technology: Introduction

In the last few years, refrigeration systems represented more than the 20% of global energy consumption, according to a recent report of the International Energy Agency.[1] These technologies are present in several scopes (both domestic and industrial), such as the cooling of drinks, food, medicaments, air conditioning, vehicles, electronic devices and so on (see Figure 1-1). Due to the global warming, this consumption is expected to grow and even to be tripled in 2050, which would mean that, for first time in history, more energy is employed for cooling than for heating.[1] But there was a long development of the cooling industry before getting to this point, which started in the XVII century and can be summarized in three big generations of refrigerants (see Figure 1-2).

Figure 1-1. Examples of different uses of refrigeration systems.

First refrigeration studies were made between the 1600s and 1700s, but it was in 1805 when the first cooling system was proposed by Evans.[2] This was the base for the most used technology for refrigeration, vapor-compression, patented in 1834, and which is based in cycles of compression-expansion of gases at low and easy-achievable values of pressure.[3] For the first 100 years, the first generation of the used compounds in this technique included a wide range of compounds, most of them flammable, toxic (or both) and, some of them, highly reactive (propane, ammonia, etc.). Therefore, the primal devices were extremely dangerous to be used at home.[4]

The second generation (1930s – 1990) of cooling compounds, the so-called fluoro-chemicals, started to be used because of their safety and durability respect to the first generation. Since then, chlorofluorocarbons (CFCs) and hydrochlorofluorocarbons (HCFCs) are the most employed families of materials for refrigeration. Nevertheless, in 1987 a group of more than a hundred countries (including the European Union and the United States of America) started to strict their use by signing the Montreal Protocol[5], as well as that of many other ozone-depleting gases, for cooling technologies. There, several arrangements were agreed in order to reduce the use of ozone depleting substances.[6,7] During the following years, 40 gases with the general formula $C_aH_bF_cCl_d$, considered as the most pollutant compounds of the second generation, started to be replaced by other gases with the general formula $C_aH_bF_c$ (avoiding Cl) —less harmful for the environment and named as controlled substances—, which represents the third generation of refrigerants.[4]

From the starting of the application of the Montreal Protocol, most of the refrigeration systems keep using the vapor-compression technique because of the easy operational pressure of the gases

employed since past generations (1-120 bar). A famous example of the used compounds is carbon dioxide (employed since the first generation of refrigerants); its working cycle is between pressures from 80 to 120 bar.[8] Other examples are the hydrofluorocarbons (HFCs), the most used family for cooling in the last decades. The most common HFCs are tetrafluoroethane (R134a), pentafluoroethane (R125), difluoromethane (R32), hexafluoropropane (R236ea) and mixtures of them (like R410A); these gases have operational pressures lower than CO_2, from 3 to 25 bar.[9] Nevertheless, HFCs and CO_2 are considered as greenhouse gases, contributing to the global warming, so their use in refrigeration systems affects negatively to the sustainability of the cooling industry. Also, some of them are flammable and toxic, so their manufacture, handling and transport represents a risk for the environment and even for operators and end-users.[10] In view of this, in 2014, the EU Regulation Mo. 517/2014 declares the prohibition of several non-ecofriendly refrigerants from 2020, 2022 and 2025, including most of the HFCs listed before.[1]
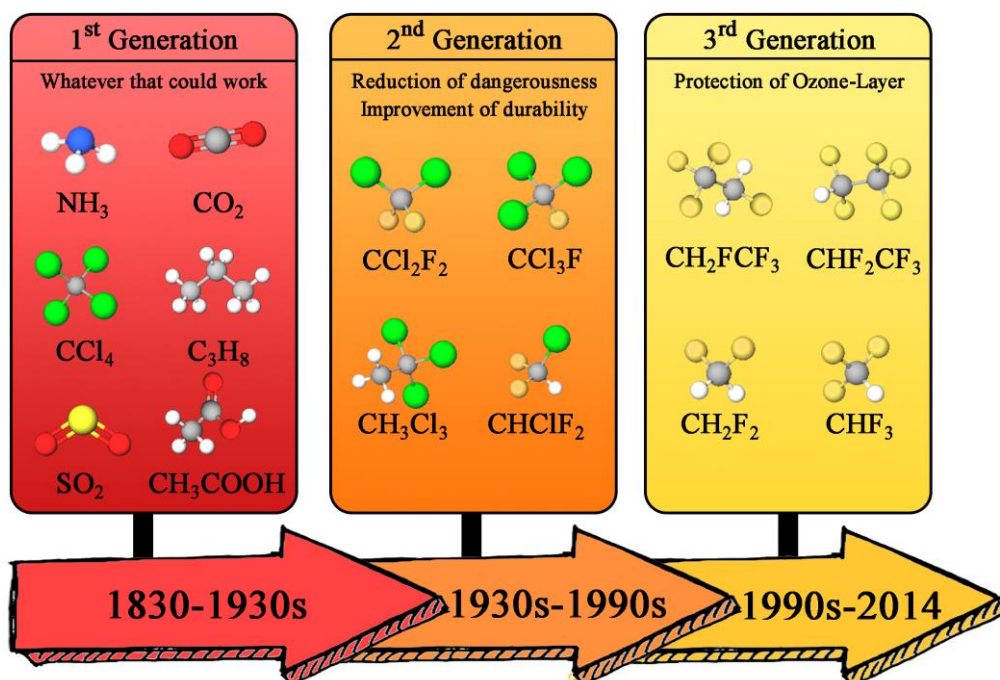
Figure 1-2. Refrigerants progression by generations with some relevant examples of each one.

Given this scenario, where a renovation of materials is necessary in order to achieve new technologies of eco-cooling far from vapor-compression of gases, new environmentally friendly systems have been discovered and studied for the last years, which would represent the fourth and last generation of refrigeration materials so far.[4] The use of *solid state materials* for cooling as alternative to avoid the polluting, toxic and hazardous gases from the refrigeration industry, is very attractive, and has serious advantages over working with fluids: [11,12,13]

- First of all, by using solid materials, it is possible to avoid the emission of volatile fluids that deplete the ozone layer and cause global-warming, which is the main problem of such compounds.
- Costs are considerably reduced when operating with solids. The investment in the safe storage of gases (since most of them are flammable and toxic), their transportation and manipulation, is considerably lower than that made in gases.

- Systems based on solids can be built more compactly, facilitating the fabrication of cooling microsystems, whose interest is increasing due to their implementation in small electronic systems.
- Another advantage is that the solid-state refrigeration technology generates much less noise than fluids technology.

In this context it is interesting to remember the basis of refrigeration based on fluid compression. Figure 1-3 shows a schematic description of a cooling cycle using fluid compression: when pressure is applied to a fluid, it undergoes a phase transition (from gas to liquid state), releasing heat to the environment (this would be the back of a fridge, for example). When pressure is removed, the fluid transforms back to the initial phase absorbing heat from the environment (this step occurs in the inside of the fridge). This cooling cycle takes advantage of the latent heat (that is, the fixed amount of energy per mass that the system either absorbs or releases) derived from the reversible phase transition. Then, the latent heat involved in the process is used to vary and control the temperature of the system.
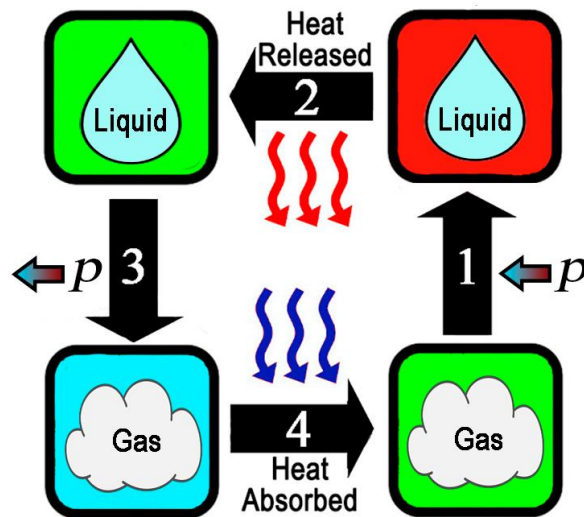
Figure 1-3. Schematic description of a cooling cycle of a fluid-compression system.

Therefore, one of the most interesting options for cooling systems based on fluid compression is the refrigeration based on the compression of solids, making use of solid-to-solid phase transitions (instead of the vapor-liquid phase transitions used in fluid compression). The process is similar to that employed by vapor-compression, but using **barocaloric materials**: materials that undergo solid-to-solid phase transitions induced by isostatic pressure. Going a step further, it is possible to use **caloric materials**: materials which undergo large temperature changes when they are subjected not only to pressure by compression, but also to other external stimuli, such as changes in magnectic, electric or mechanical applied fields. In those cases, solid-to-solid phase transitions are associated with a change in the state of magnetization, polarization, volume or strain of the solid.[14]

Given the variety of external stimuli, **caloric materials** are grouped in different types depending on the type of the external stimulus applied to cause the phase transition (see Figure 1-4). [15]

- **Magnetocaloric**: the external stimuli to induce the caloric effect is a magnetic field.[16–18]
- **Electrocaloric**: an electric field is applied to provoke the caloric effect.[19,20]

- **Mechanocaloric**: the caloric effect is driven by applied pressure. This subfamily can be divided in **elastocaloric** (if the pressure is uniaxial) and **barocaloric** (if the pressure is isostatic).[21–24]
- **Multicaloric**: materials which show more than one type of caloric effect; therefore, they respond to two different external stimuli.[25,26]
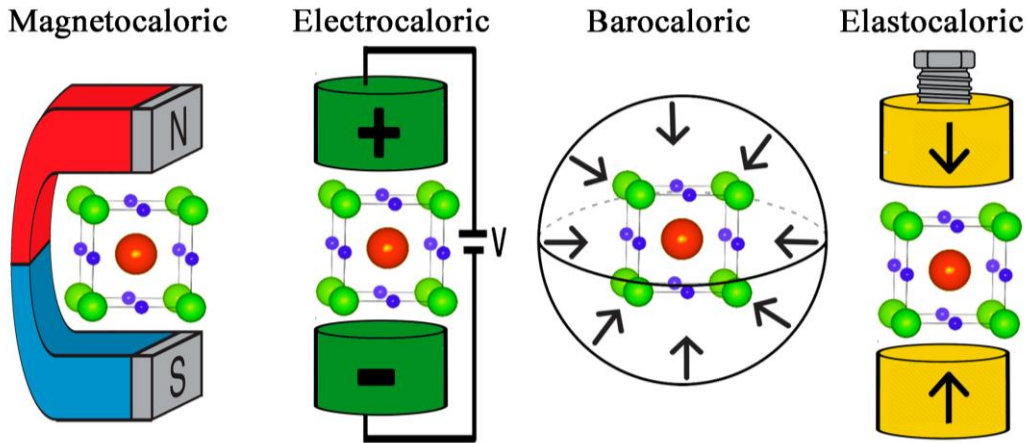
Figure 1-4. Scheme of different types of caloric effect; from left to right: magnetocaloric, electrocaloric, barocaloric and elastocaloric.

In Figure 1-5, it is represented the cooling cycle for solid state refrigeration using the caloric effect, that is analogous to the cooling cycle using fluid compression. Typically, the systems release energy and the temperature increases when the external stimulus is applied; and the reverse process takes place when the external stimulus is released. Therefore, and as shown in the cycle: First, the external field is applied isothermally to the system, which induces a phase transition, leading to heat emission and increasing the temperature. The released heat is transferred, in general, to an external fluid, until the system reaches the initial temperature. Then, the external field is isothermally removed, which induces a phase transition (the material comes back to the initial phase), leading to a heat absorption and a decrease of the temperature of the material. It absorbs energy from an external fluid (which is cooled and used for refrigeration) until the system reaches the initial temperature.[27]
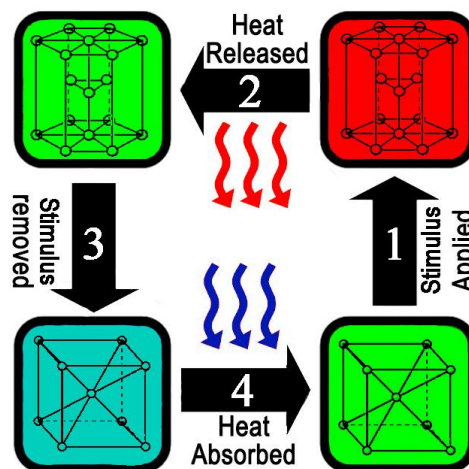
Figure 1-5. Cooling cycle for solid state refrigeration using the caloric effect.

The **caloric response** is generally quantified by the change in entropy that has been induced by the stimuli (i.e. the isothermal application -or removal- of the stimuli; or also by the variation in temperature when the stimuli are adiabatically modified).[28–30]

In view of that cooling cycle, the ideal solids to be used as caloric materials in refrigeration must show a series of requirements, the most important of which can be summarized as follows:

- Large and reversible entropy changes related to a solid-solid phase transition.
- Transition temperature near room temperature for ambient-conditions applications (or a temperature near the area of the application concerned);
- Large stimuli depencence of such transition (i.e. pressure dependence, for barocaloric materials).

In order to understand better the mechanisms of solid-to-solid phase transitions, their thermodynamics, and the methods for quantifying the caloric effect of materials with solid-to-solid phase transitions, we will further study them in the next section.

1.1.2. Solid-solid phase transitions

Any substance of fixed chemical composition can exist in homogeneous forms whose properties can be distinguished, called states. For example, water exists as a gas, a liquid, or a solid (ice) and these three states of matter (solid, liquid, and gas) differ in properties. In general, for the same solid or liquid substance, several distinct arrangements of the atoms, molecules, or particles associated with them can be observed and will correspond to different properties of the solid or liquid state, constituting phases. Phase transitions or changes of state are physical phenomena that are encountered in nature (for example, condensation of drops of water in clouds) or daily life; they are also used in numerous technical systems or industrial processes: evaporation of water in the steam generator of a nuclear power plant is the physical process for activating the turbines in electric generators, or gas condensation is used at cooling devices, etc.
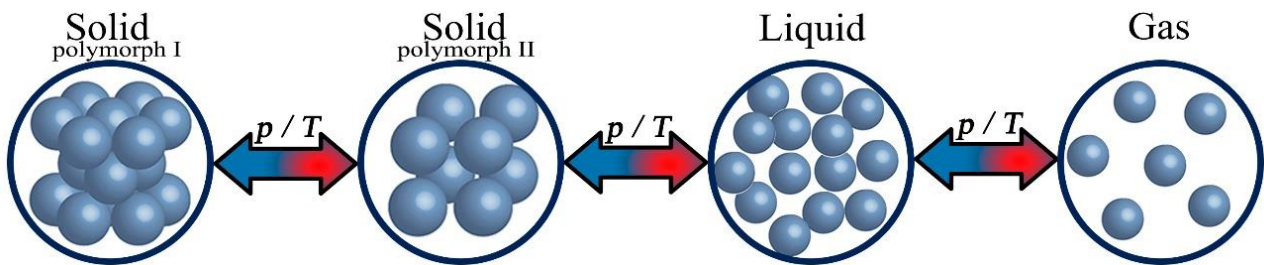
Figure 1-6. Scheme of different phase transitions from solid to gas induced by pressure (p) or temperature (T).

Apart from phase transitions due to changes of state, many solids undergo solid-solid phase transitions associated with structural changes, that are usually transitions between different crystalline forms (polymorphs) of the same compound[31] (as depicted in Figure 1-6). But these solid-solid phase transitions can occur by many more mechanisms.

Solid-solid phase transitions: Microscopic mechanisms

According to mechanisms at the atomic-level, we can say that in a large class of solid-solid phase transitions, the sytem undergoes a symmetry change, involving changes between a low-symmetry phase and a high-symmetry phase when temperature or pressure varies (easily visualized if we consider, for instance, that there are more atomic sites available in high-symmetry polymorphs than in low-symmetry ones).[32]

Nevertheless, the mechanisms of solid-solid phase transitions are complex, and consequently it is their classification. They can be initially classified in two different types: *order-disorder* and *displacive* (or *martensitic*) transitions.[32] *Order-disorder* phase transitions are induced by positional, orientational or electronic disordering. One example is when atoms in a previously random alloy become ordered on specific crystallographic sites, yielding (usually) a larger unit cell.[33] *Martensitic (or displacive)* phase transitions are produced by atomic displacements, without long-range diffusion of atoms, but rather due to some forms of cooperative and homogeneous motion of many atoms, resulting in a change in the crystal structure.[34–37] The typical example is the transition in the steel (Fe/C alloy) between austenite and martensite: while the unit cell of austenite is, on average, a perfect cube, the transformation to martensite distorts this cube by interstitial carbon atoms that do not have time to diffuse out during displacive transformation. However, sometimes it is difficult to differentiate between martensitic and order-disorder mechanisms, because they can coexist.

There are more sub-classifications of the solid-solid phase transitions which can help the understanding of those differences. One of these classifications, which may be useful in the field we are dealing with (calorics), is the one shown in Figure 1-7[38], which shows the main mechanisms of phase transitions found in caloric materials.
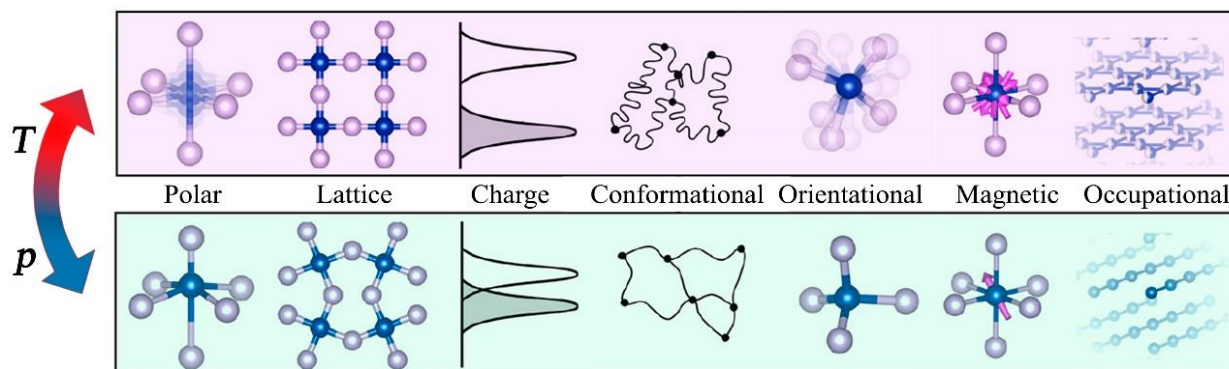
Figure 1-7. Different solid-solid phase transition mechanisms for caloric materials on applying temperature (*T*) or pressure (*p*). High-temperature (and low-pressure) phases are on top.[38]

Very commonly in caloric materials, there are *orientational* transitions, experienced by molecular caloric compounds, which involve a re-ordering of their centers of mass along the phase transition (this is the case, for example, of neopentylglycol, $(CH_3)_2C(CH_2OH)_2$)[39]. *Conformational* transitions are also common, experienced for example when the molecules are long chains, as in the case of caloric polymers (e.g. the GVG polypeptide).[40]

Phase transitions are not always induced only by modification of atomic or molecular arrangements; for example, in the case of ferromagnetism, ferroelectricity or superconductivity, there is a modification of magnetic or electronic structures.

Regarding *magnetic* transitions, there can be two main phase transitions with changes in the magnetic properties. One type are the transitions where the magnetic moments show a re-arrangement along the compound, which can be observed as a change of the tendency of the magnetic susceptibility as a function of the temperature (as for example the transition from a ferromagnetic —or a ferrimagnetic— state to a paramagnetic state, as represented by the Figure 1-8b).[41] Another type of magnetic phase transitions is related with a change in the spin distribution (from low to high, or vice versa) of the metallic atoms of a material (which are known as spin-crossover phase transitions).[42] Often, these magnetic phase transitions can be induced by both temperature and pressure.[43]

For the transitions related to changes in *polarization*, there are dielectric materials whose dielectric properties (as their dielectric constant) suffer abrupt variations involved by dielectric phase transitions that can also be induced by temperature or pressure (see Figure 1-8a). These dielectric transitions can be due to re-arrangements on the polar distribution of the phase, such as ferroelectric-to-paraelectric changes, and can occur in association to an *order-disorder* phase transition.[44]
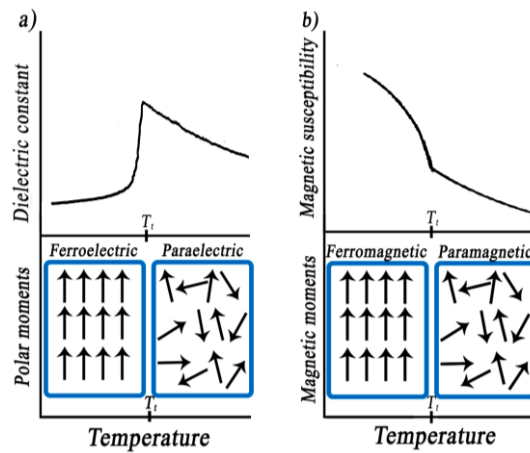
Figure 1-8. Different electric (a) and magnetic (b) properties as a function of temperature along a phase transition. T_t is transition temperature.

Therefore, and as we are seeing, two or more of these mechanisms can converge and be very difficult to differentiate. For example, *orientational* and *occupational* transitions could be considered as transitions between states with different *lattice* or *polar* freedoms. In those mechanisms, there is a symmetry breaking along the phase transition that can be given by a polar displacive transition (as in the dielectric $BaTiO_3$)[45] or an ionic re-ordering (as in $(NH_4)_2SO_4$)[46]. *Magnetic* and *charge* phase transitions can occur in the same material if it has degrees of freedom associated to the electronic structure. There can be a coupling between a change of spin (magnetism) and charge (insulator-metal) that breaks at the transition temperature (as it happens in the metal sulfide $Ni_{1-x}Fe_xS$).[38,47]

Solid-solid phase transitions: Thermodynamics

According to the thermodynamic behaviour, in general, a phase transition is manifested by a series of associated physical events. For most cases, the transition, that can be induced by temperature or pressure, is accompanied by changes in the main state variables of the system: latent heat, entropy, specific volume, heat capacity and compressibility, which we can define as follows: **latent heat (H)** is the heat released or absorbed by a chemical substance or a thermodynamic system during a change of state that occurs without a change in temperature; the variation of latent heat is related to the variation of **entropy (S)**, which can be calculated dividing the latent heat by the **transition temperature (T_t)**; the **specific volume (V)** is the amount of cubic meters occupied by a kilogram of matter; the **heat capacity (C_p)** is defined as the amount of heat that must be supplied to a material to produce a unit change of its temperature; the **compressibility (k_t)** represents the relative volume change of a material under a variation of temperature of pressure.[48]

Phase transitions can take place with or without discontinuity of the state variables. According to P. Ehrenfest, the thermodynamic characteristics of phase transitions can be very different and there are two broad categories of transitions according to thermodynamics: **first-order phase transitions** and **second-order phase transitions**[31] (illustrated in Figure 1-9). When a material is exposed to an increment of temperature (T) or pressure (p), and a phase transition occurs, the equilibrium is achieved at the transition point: transition temperature (T_t) or transition pressure (p_t). At T_t and p_t, the Gibbs free energy (G) of the solid remains continuous, but thermodynamic parameters, such as entropy (S), volume (V) and heat capacity (C_p) can suffer discontinuous

changes. The Gibbs free energy-derivative, which shows a discontinuous variation in the transition, determines the order of the transition (first-order, second-order, etc.).[32]

Thus, in a **first-order phase transition**, entropy (S), volume (V) and latent heat (H) exhibit variations for the first derivative of Gibbs free energy *(G)*, as expressed in equations 1-1:[32]

$$S = -\left(\frac{dG}{dT}\right)_p \quad ; \quad V = \left(\frac{dG}{dp}\right)_T \quad H = \left(\frac{d(\frac{G}{T})}{d(\frac{1}{T})}\right)_T \qquad \text{1-1}$$

In **second-order phase transitions**, thermodynamic potentials and their first-order derivatives are continuous, while second derivatives, referred to the heat capacity (C_p) and the compressibility (k_T) with respect to state variables (p and T) change discontinuously (see equations 1-2).[32]

$$\frac{C_p}{T} = -\left(\frac{d^2G}{dT^2}\right)_p = \left(\frac{dS}{dT}\right)_p \quad ; \quad k_T V = -\left(\frac{d^2G}{dp^2}\right)_T = -\left(\frac{dV}{dp}\right)_T \qquad \text{1-2}$$

Fig. 1-9 illustrates some important thermodynamic characteristics of those first- and second-order phase transitions.
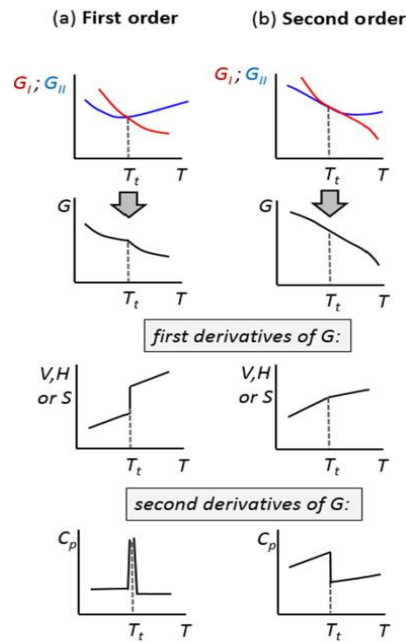
Figure 1-9. Variation of thermodynamic properties for first-order (a) and second-order (b) phase transitions as a function of temperature (*T*). Blue and red curves show the free energy (*G*) of the low (II) and high (I) temperature phases, respectively, which cross at transition temperature (T_t). *V* is specific volume, *H* is latent heat, *S* is entropy and C_p is heat capacity.[31]

For a first-order phase transition, the T_t or p_t value is different in the way of the stimulus is applied. For example, the T_t value can vary if the solid is heated or cooled, or p_t value can vary if the solid is compressed or decompressed. The difference between the values when applying or removing T

or *p* is defined as the *hysteresis*. This effect is generally employed to determine the order in a phase transition (as second-order transitions do not show hysteresis) and its magnitude is mainly dependent on the volume change associated to the transition.[49,50]

Recalling the requirements for **the ideal solids to be used as caloric materials in refrigeration** mentioned in section 1.1.1. —i) large and reversible entropy changes related to a solid-solid phase transition; ii) a transition temperature near the area of application; and iii) large stimuli depencence of such transition—, we add now that solids with first-order phase transitions, but showing hysteresis values as small as possible, will be sougth.

Given the high technological challenges of magneto and electrocaloric materials (which will be described in the section 1.1.3.) this *doctoral thesis* is focused on the study of mechanocaloric materials, where the variable that induces the phase changes is the pressure. More specifically, we will focus on barocaloric materials, in which the research group already has considerable experience.[27,51] The complex analysis of barocaloric phase transitions will be described below.

Experimental determination of barocaloric parameters

In barocaloric (BC) materials, pressure is the thermodynamic variable that induces the phase changes. Taking pressure experiments into account, different phenomena can occur in the phase transition respect to the only-thermally driven, that should be kept in mind in order to understand how to measure experimentally the barocaloric effect:

i) In structural phase transitions, when isobaric pressure is applied, the transition temperature (T_t) increases (direct) or decreases (inverse) as pressure increases. The relationship between pressure and temperature along a phase transition is given by the Clausius-Clapeyron relation[52]:

$$\frac{dT_t}{dp} = \frac{\Delta V}{\Delta S} \qquad\qquad 1\text{-}3$$

where ΔS is entropy change and ΔV is volume variation. It is worth to note that this relation can be calculated easily using the entropy change associated with the phase transition and volume of both polymorphs near the phase transition.

ii) Additionally, when hydrostatic pressure is isothermally applied to a solid, a reversible variation in the volume of the material is induced (*elastic contribution*). This process is associated with an isothermal entropy change.[52] This $\Delta S(p)$ can be estimated by Maxwell relation (equation 1-4):[46]

$$\Delta S(p) = -[m^{-1}\left(dV/dT\right)_{p\ amb}]p \qquad\qquad 1\text{-}4$$

where *p* is pressure, *V* is cell volume, *m* is mass per unit cell, *T* is temperature, and $(dV/dT)_{p\ amb}$ is the volumetric thermal expansion at constant ambient pressure. This contribution depends mainly on the structural flexibility of the solid. For example, in polymers it is very large, and as it depends on the applied pressure, it increases considerably at operational *p*.[53]

To estimate the performance of BC materials it is necessary to carry out different experimental measurements. Two essential techniques are ***Differential Scanning Calorimetry (DSC)*** and,

specially, ***High-Pressure Differential Scanning Calorimetry (HP-DSC)***, which give us more information about the effect of pressure on a phase transition. DSC is a technique based on the detection of the thermal response difference (*heat flow*) between a reference and the sample subjected at the same time to changes in temperature and in pressure (in the case of HP-DSC).[54] To study the BC properties, there are two different methods to operate: i) isobaric mode with constant heating rate (***quasi-direct method***), and ii) isothermal mode with constant pressure rate (***direct method***).[55]

This ***direct method*** is more representative of the behavior of the BC materials during their practical performance. But it is more complex experimentally, because it is very complicated to keep the temperature constant while applying a pressure ramp. Therefore, ***quasi-direct method*** is more common to study the BC properties. Nevertheless, this method demands a complex data conversion of the obtained data under isobaric conditions to isothermal conditions. To perform a proper data conversion, it is necessary to carry out a large number of isobaric experiments at different pressures.

The main characteristics of both methods are summarized below.

i)   *Quasi-direct methodology*:

For this kind of analysis, some isobaric heating-cooling (with constant rate) cycles are measured at different pressures.
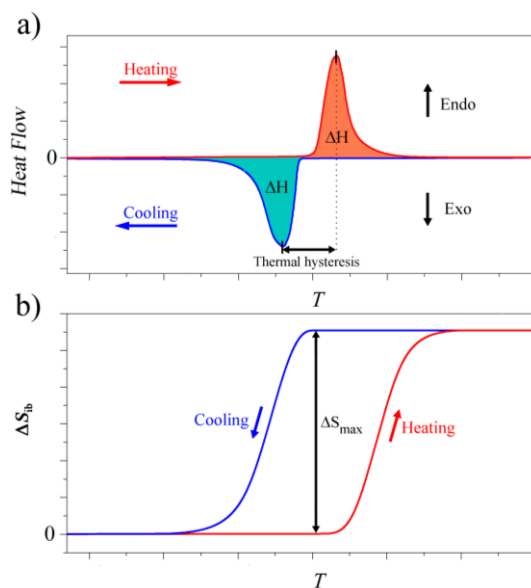
Figure 1-10. (a) *Heat Flow* as a function of temperature (*T*) in a typical DSC experiment; the shaped area represents the enthalpy variation (ΔH); thermal hysteresis is also indicated. (b) Changes in entropy (ΔS_{ib}) as a function of temperature (*T*) obtained from (a).

DSC works with programs that allow precise temperature variation under isobaric conditions, so it is possible to represent the heat flow as a function of temperature (see Figure 1-10a as a representative example). In the graph of heat flow versus temperature (Figure 1-10a) it is possible to appreciate the peaks due to a phase transition. There is an endothermic peak on heating and an exothermic peak on cooling. Thermal hysteresis (typical of first-order phase transitions) can be obtained from this graph as the temperature difference between the exothermic and the endothermic peak. There are two criteria depending on whether the onset of the peak or the maximum peak

temperature is used.[56] In this research, the maximum peak temperature was considered to calculate the transition temperature and the thermal hysteresis.

The enthalpy variation (ΔH) due to the phase transition can be obtained by integrating the area under the heating or cooling curve.

The isobaric entropy change (ΔS_{ib}) as a function of temperature at each pressure is calculated using the following equation:

$$\Delta S_{ib} = \frac{\int_{T1}^{T2} \frac{dQ}{dT} dT}{T} \qquad\qquad 1\text{-}5$$

where dQ is the experimental heat flow at isobaric conditions, dT is the heating rate and T is the temperature.

Once ΔS is calculated, it can be represented as a function of temperature (see Figure 1-10b). In this graph, when a transition occurs, ΔS_{ib} increases to a plateau that sets the maximum achievable value of this parameter.

In addition to conventional DSC experiments, it is possible to couple a high pressure cell to the experimental set-up in order to carry out several isobaric experiments at different pressures, and perform HP-DSC.
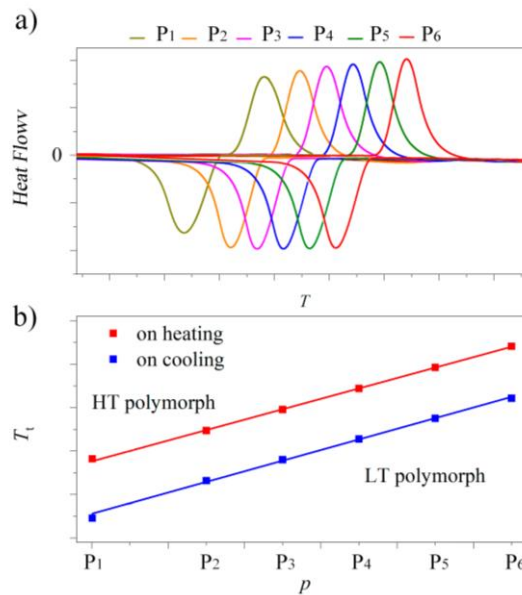
Figure 1-11. (a) Heat Flow as a function of temperature (T) at finite pressures in ascending order from P_1 to P_6. (b) Transition temperatures (T_t) versus pressure (p) obtained from the heat flow peaks on heating and cooling. HT: high-temperature; LT: low-temperature.

The representation of the heat flow as a function of temperature in a typical HP-DSC experiment using quasi-direct methodology is shown in the Figure 1-11a.

Taking into account the displacement of the transition temperature with the applied pressure, it is possible to calculate the ***BC coefficient*** (**dT_t/dp**) experimentally. This coefficient indicates the linear variation of the transition temperature with the applied pressure. The BC coefficient is the slope of the linear representation of T_t versus the applied pressure (see Figure 1-11b). For practical

applications, this BC coefficient should be large in order to reduce the operational pressure of the BC material.[51] The experimental value of the BC coefficient coincides with the obtained by the Clausius-Clapeyron relation (Equation 1-3).
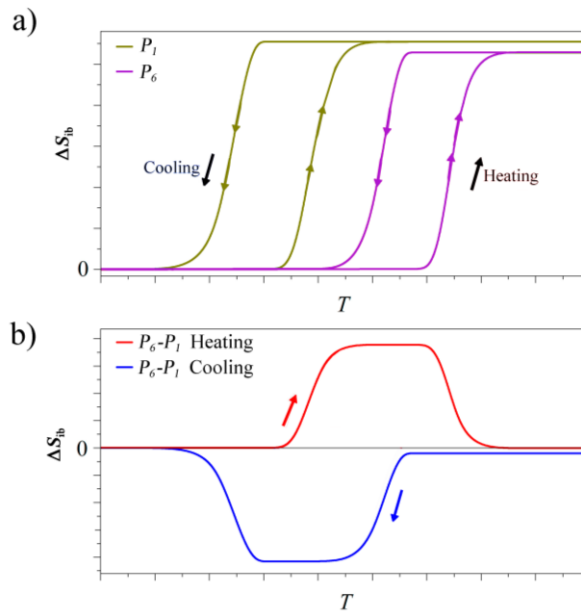
Figure 1-12. (a) Thermally driven isobaric changes in entropy on heating and cooling for P_1 and P_6. (b) Difference between entropy change at P_1 and P_6.

As in a standard DSC experiment, isobaric entropy change is obtained by using equation 1-5, but in this case it is possible to calculate it for each pressure (see Figure 1-12a). As pressure is higher, entropy change is lower. This is due to the *elastic contribution*, which increases with higher pressures, as commented before.
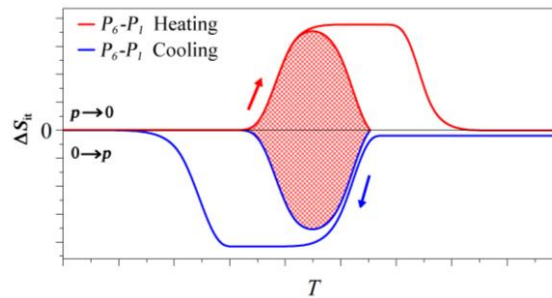
Figure 1-13. Isothermal entropy changes on heating and cooling on applying pressure (0→p) and removing pressure (p→0)for pressures P_1 and P_6. The shaded area represents the reversible isothermal entropy changes.

The following step is the key of the transformation of the isobaric measurements into isothermal results, which gives information about the BC behavior. The difference of ΔS_{ib} between the ambient pressure and each applied pressure (see Figure 1-12b) gives the temperature region where the transition can be provoked reversibly by applying each pressure isothermally (see Figure 1-13), so the isothermal entropy change ΔS_{it} can be calculated.[51]

Therefore, it is possible to improve the thermal region where maximum ΔS can be achieved reversibly by getting higher BC coefficients and by reducing the thermal hysteresis.

It was reported that the reversibility region, essential for caloric refrigeration, heavily depends on the width of the thermal hysteresis (which should be as small as possible). Given this dependence, it is necessary to analyze the adiabatic temperature changes (quasi-direct methods) as well as the isothermal entropy variation (direct methods) under cyclic conditions in order to know the suitability of a caloric material in an applicable way.[57]

It is worth to note that for practical applications it is more useful to estimate the adiabatic temperature changes induced by the applied pressure instead of ΔS. In any case, it is experimentally complex to estimate this temperature change. This drawback can be solved by using the following expression, which transforms the isothermal entropy change into the reversible adiabatic temperature change, ΔT_{rev}:

$$|\Delta T_{rev}(S; p_{atm} \leftrightarrow p)| = |T_C(S; p) - T_H(S; p_{atm})|$$ 1-6

Here, $T_c(S;p)$ is each temperature of the cooling isobaric entropy change at the high pressure and $T_H(S;p_{atm})$ is each temperature of the heating isobaric entropy change at ambient pressure. It must be noted that for using this expression, the heat capacity must be taken into account in the regions before and after the phase transition temperature region.[53]

ii)   Direct methodology:

These experiments are more representative of the behavior of materials in a BC cycle, but are more complex from an instrumental point of view and are, therefore, not common in BC publications.
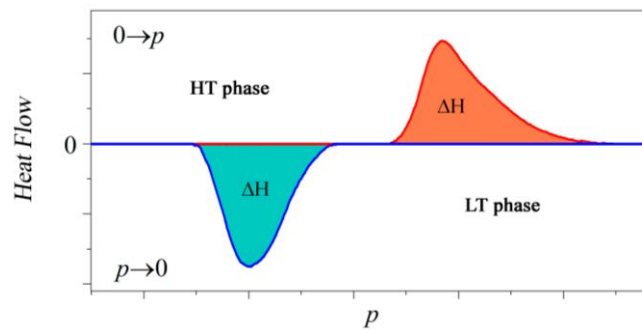
Figure 1-14. *Heat Flow* versus pressure (p) on applying ($0 \rightarrow p$) and removing ($p \rightarrow 0$) pressure in isothermal conditions from the high-temperature (HT) phase to low-temperature (LT) phase.

To perform these analyses, isothermal compression-decompression cycles (at a constant rate) are measured at temperatures above the transition temperature at ambient pressure. Figure 1-14 shows a typical representation of the heat flow as a function of pressure in a HP-DSC experiment. These curves show peaks associated to a phase transition induced by the applied pressure, and the area under each peak is the ΔH of the phase transition.

When isothermal measurements are carried out at different temperatures on a BC material, the transition pressure changes (see Figure 1-15) as it happens in quasi-direct methodology with the transition temperature.

Also, these analyses allow the calculation of the isothermal entropy change by integrating the area of the heat flow-versus-pressure curve and dividing it by the pressure, using the equation 1-7:

$$\Delta S = \frac{\int_{p1}^{p2} \frac{dQ}{dp} \, dp}{p} \qquad \text{1-7}$$

Where p_1 and p_2 are the initial and applied pressure, respectively, and dQ is the experimental heat flow.
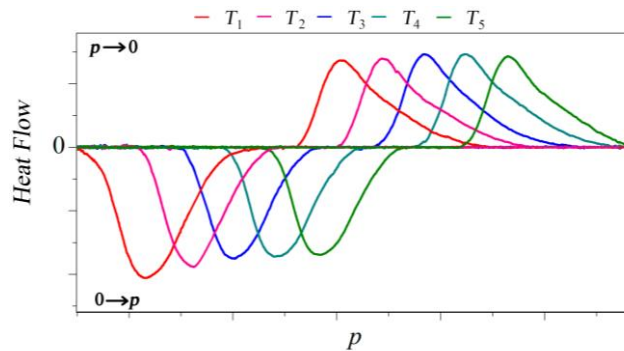
Figure 1-15. Heat Flow versus pressure (p) on applying ($0 \rightarrow p$) and removing ($p \rightarrow 0$) pressure under different isothermal conditions for temperatures in ascending order from T_1 to T_5.

In conclusion: quasi-direct and direct methodology are both valid; however, direct methods are more precise because it is not necessary a conversion of the measurements from isobaric to isothermal, as in quasi-direct methods.

After describing the methodolgy to study the BC effect, the selection of the BC materials to be analyzed for solid-state cooling applications will be contextualized and explained below.

1.1.3. Barocaloric materials: state-of-art

For the last decade, magnetocaloric and electrocaloric systems have been the focus of attention as the alternative to vapor-compression cooling. Nevertheless, these systems involve some characteristics which hinder their application in industry:

- The need to apply magnetic or electric fields that are usually large (in the order of ~5 T and ~500 kV cm^{-1}, respectively) to cause the phase transitions is a technological and also an economic limitation.[58,59]
- The synthesis of most of these materials is usually complex and many of them use rare-earth metals, such as Gd, La, Rh or Sm (inter alia), whose cost is very high.[60–64]

Given this background, mechanocaloric materials seem to be a more technologically and economically accessible alternative. The disadvantage of this family is the difficulty in achieving high values of latent heat compared to magneto and electrocaloric materials, which can achieve high values ($\Delta S \sim 50$ J kg^{-1} K^{-1}).[65,66] However, similar and higher energies were obtained by mechanocaloric materials in recent years.

Different families of materials were studied along the years with a different dominant degree of freedom underpinning the mechanocaloric (MC) effects, which makes their properties classifiable.[38,46,67,68] First studies in mechanocaloric materials started by finding this property in *intermetallic* compounds, as the used as magnetocaloric materials, whose main degree of freedom is magnetic and whose elastocaloric effect was also reported.[37] The possibility of reaching a significant caloric effect inducing the phase transition with pressure instead of a magnetic field would open a new field in solid-state refrigeration.[69] Intermetallic materials with the general formulas Gd$_5$(Ge$_{1-x}$Si$_x$)$_4$[70] or La(Fe$_x$Si$_{1-x}$)$_{13}$[71] are representative examples because of their small hysteresis and large volume changes in their phase transitions. The maximum isothermal entropy change showed by these materials is around 20 J kg^{-1} K^{-1} under pressure cycles of 1 kbar (see Table 1-1).[69]

The next step in the MC research was to look for factors that could increase the phase transition entropy change. It was found that the presence of the NH$_4^+$ cation could cause a bigger disorder in the transitions of fluoride and oxyfluoride structures and, furthermore, turn the transition into ferroelastic. This fact means that these compounds could show barocaloric effect.[72] The compound (NH$_4$)$_3$MoO$_3$F$_3$ is an example of these materials, which shows an entropy change of 55 J kg^{-1} K^{-1} under the large pressure of 5 kbar, and whose behavior under pressure was published in 2011[59] (see Table 1-1). The compound (NH$_4$)$_3$MoO$_3$F$_3$ is one of the first reported *BC hybrid organic-inorganic perovskites* (an interesting type of materials to which we will return later). That work, which compares other similar perovskite-like fluorides and oxyfluorides, reported that the changes of the transition temperatures of phase transitions, the sensitivity to pressure and the entropy variation of phase transitions can be provoked with small chemical changes in the perovskite structure.[59]

The same NH$_4^+$ cation is present in another BC compound studied during the same period, NH$_4$SO$_4$, that has a polar main degree of freedom. This compound reaches a maximum entropy change of 60 J kg^{-1} K^{-1} at a pressure of 1 kbar, but this transition occurs below room temperature.[73] This finding led to the study of other *ionic compounds* as BC materials, such as AgI, which has a similar value of entropy change in its phase transition (see Table 1-1).[74] Even the needed pressure to reach significant values of entropy was high, the synthesis of these ionic compounds is simpler and cheaper than the *intermetallic* BC materials.

Table 1-1. Selected BC parameters of some of the best barocaloric materials reported when this doctoral thesis was in its first year of development (2018/2019). BC, barocaloric; T_t, transition temperature; ΔS, entropy change; ΔT, thermal hysteresis; p, pressure applied for reversibility.

BC Material	Classification	Date (mm/yy)	T_t (K)	ΔS (J Kg^{-1} K^{-1})	ΔT (K)	p (GPa)
$Ni_{49.26}Mn_{36.08}In_{14.66}$[75]	Intermetallic	04/10	293	24	4.5	0.26
$(NH_4)_3MoO_3F_3$[59]	Hybrid perovskite	01/11	297	55	15	0.5
$Gd_5Si_2Ge_2$[76]	Intermetallic	16/12	270	11	1.1	0.2
$Gd_5Si_2Ge_2$[69]	Intermetallic	01/13	255	21.0	4	0.1
$LaFe_{11.33}Co_{0.47}Si_{1.2}$[69]	Intermetallic	01/13	237	11.4	1	0.1
$Fe_{49}Rh_{51}$[77]	Intermetallic	06/14	308	12.5	8.1	0.11
Mn_3GaN[78]	Intermetallic	10/14	285	22	4.8	0.09
$(NH_4)_2SO_4$[73]	Ionic salt	11/15	219	60	8	0.1
$[TPrA]Mn(dca)_3$[51]	Hybrid perovskite	06/17	330	37.0	5.0	0.007
AgI[74]	Ionic salt	11/17	435	64	25	0.25
Natural Rubber[79]	Polymer	12/17	303	17	10	0.43
$[TPrA]Cd(dca)_3$[80]	Hybrid perovskite	08/18	385	11.5	1.4	0.007
$(CH_3)_2C(CH_2OH)_2$[39]	Organic plastic crystal	04/19	325	383	30	0.25
$MnCoGeB_{0.03}$[81]	Intermetallic	08/19	305	20	10	0.37
$(NH_2)C(CH_2OH)_3$[53]	Organic plastic crystal	11/19	331	599	75	0.5
$(CH_3)C(CH_2OH)_3$[53]	Organic plastic crystal	11/19	350	479	5	0.04
$(CH_3)_3C(CH_2OH)$[53]	Organic plastic crystal	11/19	211	197	20	0.18

Hybrid organic-inorganic materials (HOIMs) with barocaloric properties

The presence of organic molecules in an ionic structure (as the NH_4^+ cation in the oxyfluorides) has led to deeper studies in the so-called family of *hybrid organic-inorganic materials (HOIMs)*.

Many different systems, including a wide range of different materials, can be described as hybrid materials, but for the present *Thesis Dissertation*, this term will be defined by taking into account several concepts of composition and structure. The definition which more area includes is that a hybrid material is a material with two moieties blended on the molecular scale. Generally, one of these components is organic and the other one is inorganic in nature.[82] In the context of this *doctoral thesis*, HOIMs will be classified in two big groups:

i) HOIMs that incorporate organic and inorganic components as **building blocks**.
ii) HOIMs with organic cations combined with inorganic anions in an **ionic network**.

i) HOIMs that incorporate organic and inorganic components as building blocks.

In a typical HOIM formed by organic and inorganic components forming **building blocks**, metal cations or metallic clusters are connected with covalent bonds by organic or inorganic ligands, generating frameworks which can have guest molecules (organic cations or solvent molecules) in the cavities, as seen in Figure 1-16.[83,84]
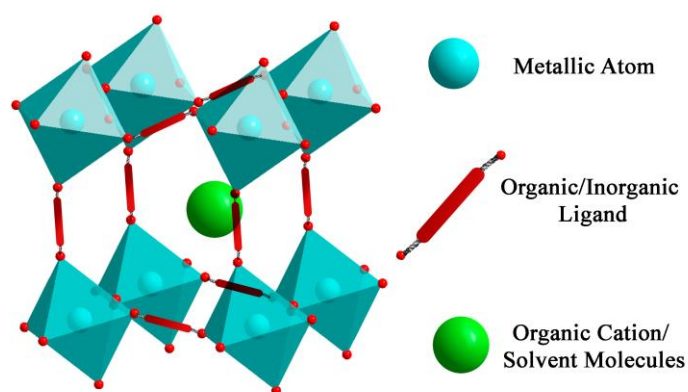
Figure 1-16. Scheme of the coordination of the building blocks into a hybrid organic-inorganic material.

Depending on the porosity, those HOIMs can be divided in *porous* and *dense*.[85] Porous hybrids (see Figure 1-17 left) present long and flexible organic ligands forming large cavities and channels that can facilitate diffusion, exchange and release of different guest molecules. They are also called metal-organic frameworks (MOFs).[85] There must be pointed that HOIMs are different from organometallic compounds, which are characterized by direct, more or less polar bonds between metal and carbon (but keeping the organic nature).[86]
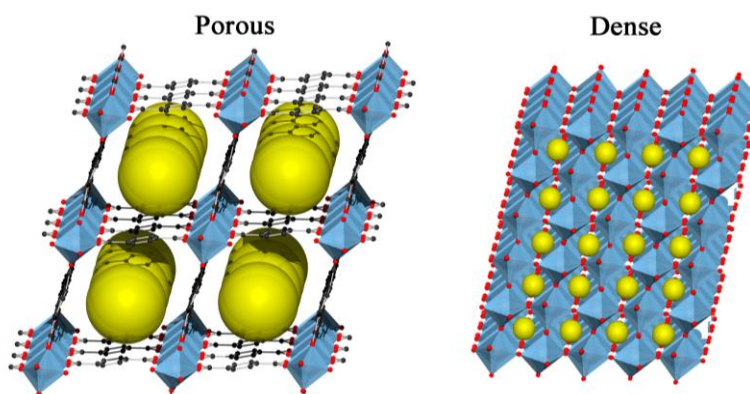
Figure 1-17. Scheme of two examples of HOIM-structures: porous (left) and dense (right).

Dense hybrids have shorter ligands and, therefore, present smaller cavities and limited mobility of the guest molecules and the framework (see Figure 1-17 right). This can lead to energetic solid-solid phase transitions when a stimulus is applied to change to the most stable configuration (a very interesting point for their potential caloric applications). Moreover, this group present structures similar to classic inorganic solids and, accordingly, they also can exhibit multifunctional properties (coupling for example caloric properties with magnetic, electrical, etc.). The most interesting thing is that these properties can be modified with small chemical variations in the organic part, in the inorganic part, or both, in all the hybrid materials.[87]

One interesting group belonging to the *hybrid organic-inorganic dense materials,* is the so-called *hybrid organic-inorganic perovskites*, a well known family to the research group where this *doctoral thesis* was carried out. *Hybrid organic-inorganic perovskites* exhibit a wide chemical diversity based on the general formula ABX_3. The ideal aristotype perovskite, with ABX_3 formula,

has a cubic stucture and the unit cell can be described as BX_6 octahedrons in the corners of the cube and the A-cations occupying the cuboctahedral cavities (see Figure 1-18).[88]
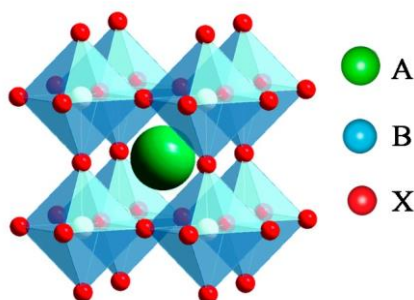
Figure 1-18. General perovskite drawing for the formula ABX_3.

Hybrid organic-inorganic perovskites are those where the A-site is occupied by an organic entity, B is a metal cation and X represents an organic or inorganic anion that links the metal atoms of the B-site. The A-site is generally occupied by short organic cations like butyl, propyl, ethyl and methylammonium (MA) derivatives, formamidinium (FA), imidazolium (IM), and so on. The metallic atoms are connected by organic or inorganic molecules such as halogens or polyatomic ligands like cyanide (CN^-), dicyanamide (dca), azide (N_3^-), formate ($HCOO^-$), etc.[89–91] There are many possible combinations exchanging A, B or X (see Figure 1-19), keeping one, two or substituting the three components, naturally taking into account the atoms must fit in the holes in the structure (which can be predicted using the so-called tolerance factors)[92–94]. This opens a wide range of combinations, allowing the modulation of physical properties and leading to new properties as (multi)functional and (multi)stimuli materials, including those studied in this *doctoral thesis*: BC materials.[91,95–97]
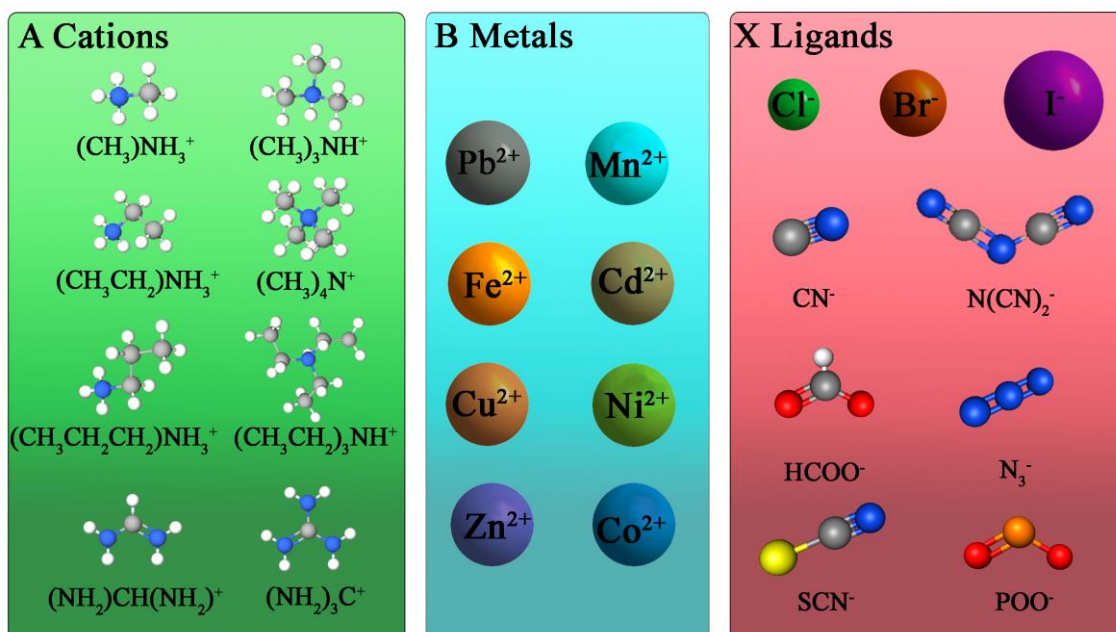
Figure 1-19. Examples of different components for the sites A, B and X in the general formula ABX_3 for hybrid perovskites.
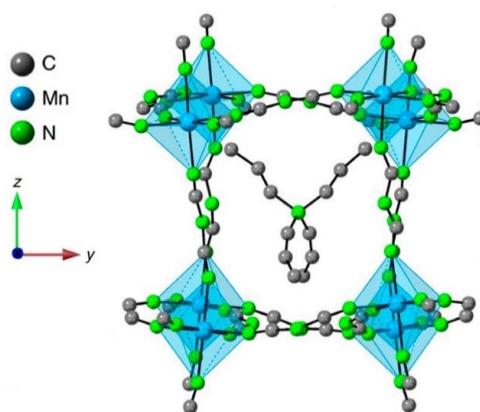
Figure 1-20. [TPrA][Mn(N(CN$_2$))$_3$] structure.[99] H-atoms are not represented.

High BC effect was found by the first time in a *hybrid organic-inorganic dense material* in the group[27] where this *thesis* was carried out, in 2017, in the hybrid [(CH$_3$CH$_2$CH$_2$)$_4$N]Mn(N(CN)$_2$)$_3$ (also called [TPrA][Mn(dca)$_3$] (Figure 1-20)[71,80] This compound shows an entropy change of 37 J kg^{-1} K^{-1} at a pressure of 0.07 kbar (see Table 1-1).[51] The sensitivity to pressure is related to the structural solid-solid phase transition driven by synergistic association of the off-centre displacements of the organic cation [(CH$_3$CH$_2$CH$_2$)$_4$N]$^+$ —tetrapropylammonium (TPrA) —and the order-disorder of their pending propyl groups and the [MnN$_6$] octahedral tilting and order-disorder associated with the ligands (N(CN)$_2$)$^-$ —dicyanamide (dca)—.[98] Therefore, the presence of organic components in the structure is providing a big disorder in the phase transition, which means, for this example, a big entropy change with considerably small pressure. The behavior of this compound opened a lot of possibilities to create new hybrids with an improvement of their BC properties.
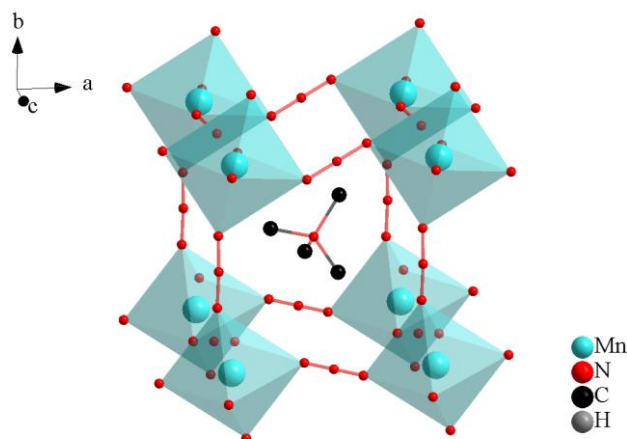
Figure 1-21. [(CH$_3$)$_4$]Mn(N$_3$)$_3$ structure.[100] H-atoms are not represented.

Following this discovery, this group identified the main requirements that materials should fullfil to display large BC effects useul for cooling applications and use them as an easy search tool to detect potential candidates within the family of hybrid perovskites.[52] For that, different parameters, as transition temperature, entropy change and the BC coefficient, were compared. It was concluded that the BC effect in these compounds is due to the flexibility of the materials, which also establishes the operational temperature. This was next checked and reported for the hybrid

perovskite [TPrA]Cd(dca)$_3$, reported with a similar BC behavior (see Table 1-1) to that shown by its Mn-analogue [TPrA]Mn(dca)$_3$.[80]

It was also found that **azide-perovskites** (those where the X-site is occupied by an azide ligand N$_3$) show high entropy changes and high theoretical BC coefficients, close to 15 K kbar^{-1}. Azide-perovskites, as [(CH$_3$)$_3$]Mn(N$_3$)$_3$ (see Figure 1-21), show order-disorder transitions and off-center shifts of the A cation and also the azide ligand, which can lead to change the coordination mode.[100]

With this background, **new azide-perovskites** were one of the selected families to continue with the search of BC materials in this *doctoral thesis*. The selection of the most suitable azides, their synthesis, characterization and, very important, the experimental determination of their barocaloric properties, constitute a part of the main objectives of this work. In addition, other possible functional properties that could coexist in those azide perovskites with the barocaloric behavior will be studied.

ii) HOIMs with organic cations combined with inorganic anions in an ionic network. Hybrid plastic crystals (PCs)

In addition to HOIMs with building blocks structure, we considered a second group of HOIMs in which organic cations and inorganic anions are combined in an **ionic lattice.** It is to be expected that the presence of weak chemical interactions between the ionic components allows a large pressure responsiveness and barocaloric coefficient. At the same time, this pressure responsiveness should be enhanced by the soft nature of organic components, meanwhile the inorganic components should increase the materials density that allows a larger volumetric barocaloric effect.

In the search of solids that exhibit solid-solid phase transitions, a type of ionic lattice HOIMs is of particular interest, which is a group included in the large family of the so-called **plastic crystals (PCs).**

PCs were firstly described in 1961 by Timmermans[101], and they have been deeply studied since then. He reported that a big group of organic molecular crystalline compounds (methane, tetrachlorometane, pentaerytriol, methylcyclohexane and so on) exhibits plastic phases before melting, showing a remarkable high "plasticity". Such plasticity is related to their mechanic behaviour: irreversible deformations can be produced without fracture of the material when stress is applied (see Figure 1-22).
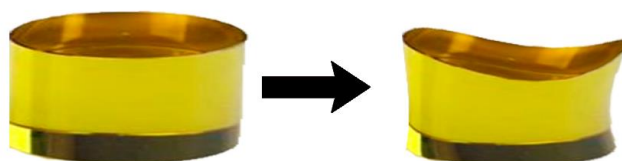
Figure 1-22. Scheme of an irreversible plastic deformation in a PC.

Looking at the internal structure, a **PC** can be defined as composed of weakly interacting units that possess some degree of freedom. As depicted in Figure 1-23, the plastic-crystal-state is a mesophase between the crystalline and the liquid state often found in ionic compounds with large molecular moieties, which acquire some degree of freedom above a certain temperature, while their center of gravity remains fixed in the crystal lattice.[102]
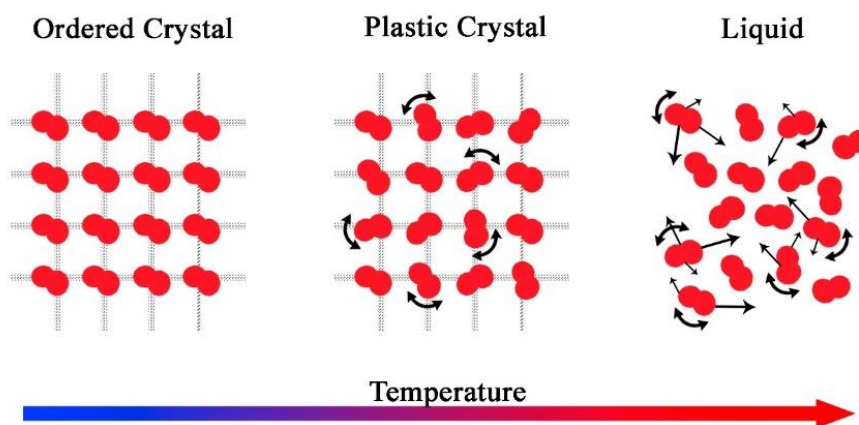
Figure 1-23. Scheme of phase transitions, activated with temperature, from an ordered molecular crystal (left) to a liquid (right), passing through a PC phase (middle).

Considering the type of applications on which the present work is focused, it is very interesting that these compounds could easily undergo those solid-solid phase transitions —from a crystal-state to a plastic-crystal-state—, causing an increase of entropy, but keeping a crystal lattice. Those phase transitions can be related to different mechanisms as *polar, lattice*, or *occupational* freedom, among others (see section 1.1.2.). However, the most interesting phase transitions for solid state cooling applications (and also thermal energy storage, that we well see in section 1.2.2.) are those where the molecules get disordered with an increase of the *orientational* and *rotational* freedom above a temperature or (below) a pressure point.[38]

It was very recently reported that some of that kind of compounds exhibit record colossal barocaloric effects. A very remarkable example is neopentylglycol (NPG) —$(CH_3)_2C(CH_2OH)_2$— with a value of 383 J kg^{-1} K^{-1} at 2.5 kbar.[39] (see Table 1-1). Similar entropy variations of the same magnitude order were reported for other similar PCs (and at similar values of pressure) such as pentaglycerin — $(CH_3)C(CH_2OH)_3$— (see Table 1-1).[103] However, those compounds require operating pressures above 2500 bar, which hinders their commercial applications.[39,53]

But in the last decades, this plastic crystal behavior was also found in an emerging family of HOIMs with molecular (instead of 3D-framework) structure,[104] which we refer to as **hybrid PCs**. HOIMs in which plastic crystal behavior was found have a molecular structure composed of discrete inorganic anions and organic cations with weak electrostatic interactions. There are many examples of hybrid PCs undergoing this characteristic phase transition to a plastic-crystal-state.[105–110] In order to illustrate the molecular changes produced in a phase transition to a plastic-crystal-state, we selected the halometallate $[(CH_3)_3(CH_2Cl)N]FeCl_4$[111] as a representative and interesting example. This hybrid contains polyatomic organic (trimethylchloromethylammonium) cations and polyatomic inorganic (tetrachloroferrate) anions, while maintaining the molecular nature of the organic PCs. The phase transition induced with temperature in this compound is shown in Figure 1-24. The reversible mechanisms for the phase change can be driven by rotational disorder and also by orientational disorder. Rotational disorder derives from the onset of rotator motions around one or more molecular axes. The presence of rotator phases can lead to one or several phase transitions from orientationally ordered phases to orientationally disordered phases, attaching an increase of entropy as temperature increases.[112] In addition to this, by disorder, ions can find themselves in different, energetically equivalent positions from which they can swap from one to another.[113]
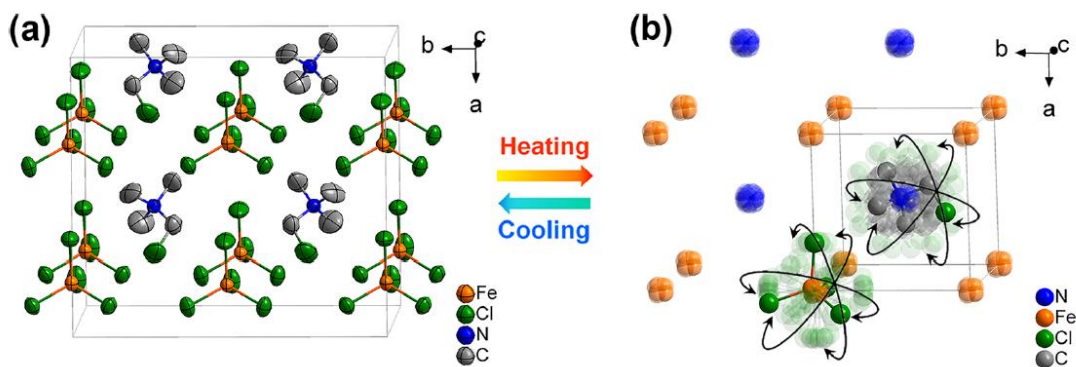
Figure 1-24. Crystal structures of the hybrid PC [(CH$_3$)$_3$(CH$_2$Cl)N]FeCl$_4$ below (a) and above (b) the transition temperature. (b) represents the plastic-crystal-state. All hydrogen atoms, part of chlorine and carbon atoms were omitted for clarity.[111]

Several switching properties of **hybrid PCs**, related to phase changes, have been published, such as dielectric, ferroelectric, optical, magnetic and also caloric properties.[108,110,111,114–117] Thanks to these properties (coexistent in some cases), hybrid PCs have big potential in several applications in the fields of memory devices, sensors, optoelectronics, and even in the ones we are most concerned in this thesis: energy storage and caloric cooling. Other interesting point from the practical point of view, is that many of these hybrid plastic crystals can be obtained by easy and low-cost methods as thin-films, which is desirable for a lot of practical and commercial applications.[118]

However, up to the date of initiation of this work, this family of hybrid PCs had not been studied before as BC materials. So, among the hybrid PCs reported so far, those that presented some of the ideal parameters of a good BC material were selected: energetic phase transitions close to room temperature with relatively low thermal hysteresis. The first selected candidate was [(CH$_3$)$_3$(CH$_2$Cl)N]FeCl$_4$,[111] which fits with the sought parameters. Very interestingly, this compound was reported as potential candidate for *thermal energy storage (TES)* applications (that we will see in section 1.2.2.).[111] Another interesting fact of [(CH$_3$)$_3$(CH$_2$Cl)N]FeCl$_4$ is that shows sharp *dielectric* and *magnetic* transitions along the structural transition, making it interesting for its potential *multi-functionality*. Other non-reported material selected for our studies, related to [(CH$_3$)$_3$(CH$_2$Cl)N]FeCl$_4$, was [(CH$_3$)$_3$S]FeCl$_4$, which will be studied in the **chapter 3**.

Thus, it was decided to synthesize new similar PCs by making small chemical variations, such as changes in the organic cation or in the halometallate, in order to find new potential hybrid PCs for both cooling and TES applications (which will be commented in the following section, 1.2.), and even multifunctional ones.

1.2. Phase change materials for thermal energy storage

1.2.1. Thermal energy storage: Introduction

If cooling applications represent around 20% of global energy consumption, as commented in the section 1.1., **heating technologies** have a higher utilization and represents the 40% of CO_2 emissions.[119] In fact, the main objective of energy systems is obtaining heat, which is necessary for almost everything in the current society: from the most basic activities (cooking, domestic heating) to more complex processes (metallurgy, refinery). However, the production of energy for heating not always has an immediate use, so it must be pointed the important necessity of storing the energy once it is produced.

Figure 1-25. Examples of different renewable energies whose storage is essential.

First systems in history to acquire useful heat employed wood combustion. Wood can be stored during periods of low demand, as in warm seasons, so it can be considered as the first system of energy storage. But, wood is limited and its use has associated problems such as deforestation.

For the last decades, one of the most common technology to produce energy is the combustion of fossil fuels, which are stored as gasses (natural gas), liquids (petroleum) or solids (carbon).[120] However, the use of fossil fuels has two main problems: they are polluting and limited; that is why renewable energy systems are experimenting a high increase in their use during the last decades.[121] Therefore, the tendency is to obtain energy from sustainable and renewable sources.

In this context, right now, the main sources of energy are renewable sources that only depend on natural phenomena, such as solar, wind, hydro, marine and geothermal, among others (see Figure 1-25).[122] Whether the energy source is eco-friendly or not, both systems share the technological challenge of storing their production in an efficient way, specially renewable systems, whose source is not a storable material, unlike fossil fuels.[123] The main inconvenience of renewable energies is related to match the production and consumption peaks. For example, solar energy maximum peak of production is during day, while most of domestic energy demand is at night (see Figure 1-26).Thus, there is an important necessity of employing efficient systems of energy storage to avoid the waste of the excess of energy.[124] As energy demand is irregular, there are on-peak and off-peak consumption periods. The efficiency of the provision can be improved by storing energy in the off-peak and releasing it in the on-peak period.
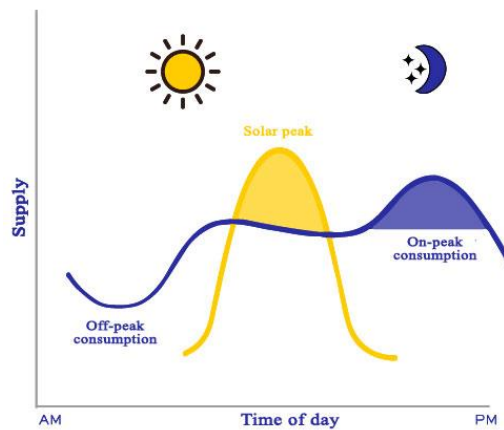
Figure 1-26. Scheme of solar energy production and demand peaks along a day.[125]

There are different systems for *energy storage*.[120,126] One of the most common is mechanical, which stores the energy during the off-peak by mechanical movement, converting it into kinetic energy to be released during the on-peak period.[127] Another typical system is the electrochemical energy storage with batteries that store chemical energy in two electrodes (a reductant and an oxidant).[128] Other systems, like the chemical, take advantage of chemical reactions such as the hydrogen produced from solar energy or the formation of ammonia with nitrogen and methane.[129]

In this context, **thermal energy storage** is a technology employed to stock thermal energy into a storage medium, so it is possible to use this energy later.[130] Typically, the TES systems use the residual energy from a heating or cooling source to be exploited mainly in buildings and industrial processes.[131] Obviously, TES systems that allow the *storage of solar energy* are of particular interest.

There are two types of mechanisms for TES[132]: those based upon the employment of the "***sensible heat***" (solid and/or liquid compounds), and those based on the "***latent heat***" of phase change materials (PCMs).[120]

In **sensible heat storage** systems, the energy can be stored by transferring the sensible heat —the energy involved in changing the temperature of a material when it is heated— from a warmed material to another cooler material or to the environment by radiation, convection or conduction. The **sensible heat energy storage capacity** of a material *(E)* can be calculated from the product of the specific heat of the material (C_p) and the temperature variation, according to the equation 1-8:[133]

$$E = m \left\{ \left[\int_{T_1}^{T_2} C_p dT \right] \right\} \qquad \text{1-8}$$

where *m* is the mass, C_p is the specific heat and T_1 and T_2 are the initial and final temperatures, respectively.

A domestic example of sensible heat storage is the use of a bag of hot sand or hot water to warm a bed. Although the materials used in this system are simple and cheap (clay, brick, wood, water), the amount needed is usually large, which finally increases the cost. Besides, there are always energy losses with this method, so the isolation costs are also high.[124]

Latent heat storage is the other main energy storage mechanism and it involves a **phase transition**. In these systems, latent heat is absorbed or released at a constant temperature during

the phase transition and it can also be exploited for energy storage.[124] Typically, liquid-gas, solid-liquid or solid-solid phase transitions are involved in latent heat storage. However, solid-solid transitions offer some advantages as small volume variation and the simpler requirements for the container of the material because the leakage problems of liquid and gases compounds are avoided.

The charge-discharge of a latent heat energy storage process is very simple.[134] As an example, the performance of a simplified **domestic solar latent heat storage system** is shown in Figure 1-27. During the day, the charge process takes place: the solar energy increases the temperature of the TES material and induces a solid-solid phase transition on heating the material above the phase transition temperature T_t. As consequence, the material undergoes to the high temperature polymorph and absorbs heat from the environment. Now, the material is charged and the thermal energy is stored into the material while it is maintained at $T>T_t$. When night comes and temperature decreases, the discharge process occurs: the material undergoes again the phase transition and returns to the initial phase, which provokes the release of the stored thermal energy to the environment.
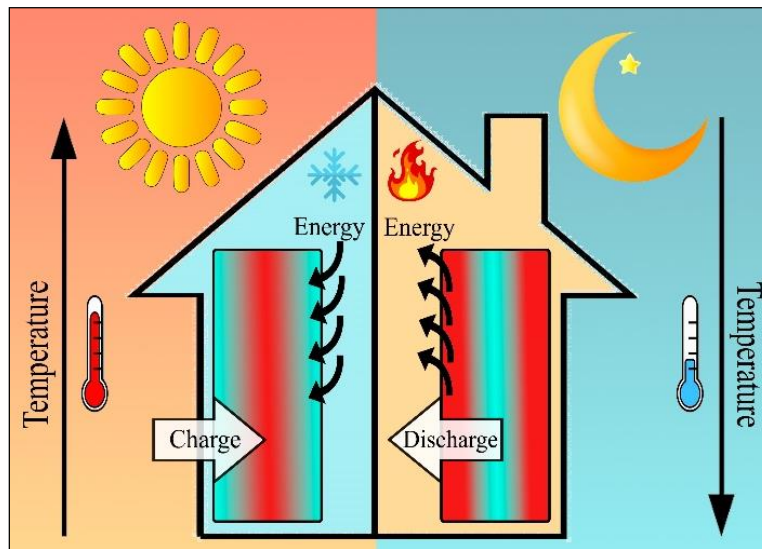
Figure 1-27. Representation of a domestic solar thermal energy storage system.

In this case, **latent heat TES capacity (E)** can be estimated by combining the sensible heat TES capacity in the low and high temperature polymorphs and the latent heat of the phase transition, according to the equation 1-9:[135]

$$E = m\left\{\left[\int_{T_1}^{T_t} C_p^{LT} dT\right] + \Delta H + \left[\int_{T_t}^{T_2} C_p^{HT} dT\right]\right\} \qquad \text{1-9}$$

where m is the mass of the material, ΔH is the latent heat due to the phase transition, C_p is the specific heat of the low-temperature (LT) and high-temperature (HT) polymorphs, T_t is the transition temperature and T_1 and T_2 are the initial and final temperature of the process of energy storage.[111] The presence of a phase transition in the operational range of a latent heat TES material means a significant increase of the storable energy with respect to only sensible heat TES systems (see Figure 1-28).
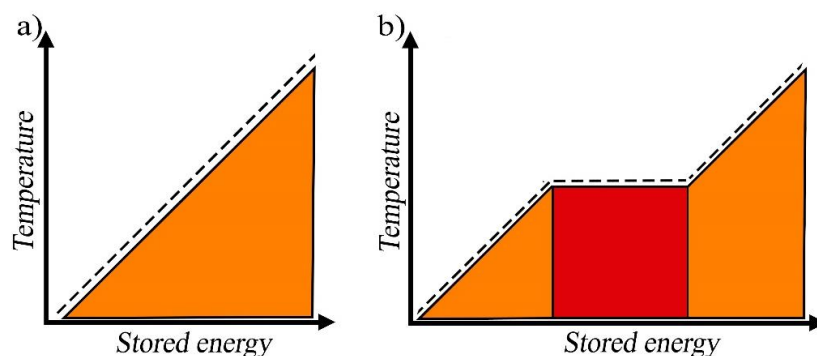
Figure 1-28. Representation of the storable heat on heating for (a) sensible heat TES and (b) latent heat TES.[132]

As in the case of the BC parameters (section 1.1.2.), *Differential Scanning Calorimetry (DSC)* measurements are very useful to study TES materials; more precisely, for the estimation of operational temperatures of a latent heat TES compound, or for enthalpy (ΔH) in the phase transition (calculated as the area under the curve of heat flow-versus-temperature). In addition, the specific heat (C_p) of both polymorphs can also be measured as a function of temperature, in order to calculate the latent heat TES capacity of the system (E) using the equation 1-9.

Along the last decades, it has been reported a large diversity of materials with the suitable thermo-physical properties for TES. Their characteristics to perform efficiently can be different, like the charging/discharging temperatures, the latent heat or its volume change, among others. Nevertheless, there are some thermo-physical properties which are mainly important when looking for an **efficient and suitable latent heat storage** compound:

- The transition temperatures (on heating and on cooling) must fit the desired temperature operating range. The working ranges can be classified in high temperatures (500 K to 1000 K), medium temperatures (373 K to 500 K) and low temperatures (273 K to 373 K).[136,137] In this latter, for solar TES it is required that the phase transition occurs in the temperature range from 283 K to 363 K.[138]
- A considerable difference between the charging and discharging temperature is required to store the thermal energy over a wide temperature range.[139] It is worth to note that while the thermal hysteresis should be small for solid-state cooling applications, for TES it should be as large as possible.
- A large latent heat is required.[135] Additionally, as all materials have sensible heat storage contributions, it is desirable a large specific heat.[140]
- Low thermal expansion is needed. As the materials undergo a volume change with temperature and phase transitions, it is required that this change is small to avoid problems with the sample container.[135]
- High thermal conductivity is necessary to favor the energy exchange with the environment.[135]

Besides thermo-physical requisites, and in a manner comparable to what is sought in BC materials, there are other requisites to consider for a good TES material. It must be chemically stable, because of the possible reaction with other compounds in the work environment would decrease the energy storage capacity. Furthermore, it must not be toxic, even that it is easier to isolate a toxic solid than a toxic fluid. Another important requisite is the prize, which (for commercial applications) is always desired to be as low as possible.

1.2.2. Thermal energy storage materials: state of art

Along the last decades, different solid-solid PCMs have been employed for TES applications, which we found in the literature classified in four main families: polymeric, organic, inorganic and MOFs (*metalorganic frameworks,* which consist on organic-inorganic hybrid structures, based in metallic centers united by long organic molecules, to which we refer as "porous HOIMs'' in section 1.1.3.). Table 1-2 summarizes the most relevant magnitudes found so far (reviewing recent literature) to be taken into account for the use of these materials in thermal storage.[141]

Table 1-2. Main properties for solid-solid TES of different materials: T_t, transition temperature; ΔH, enthalpy change; volume change; and thermal stability.[141]

Family	T_t (K)	ΔH (J g^{-1})	Volume change	Thermal stability
Polymeric	284 – 338	10 – 205	Large	Small
Organic	298 – 463	15 – 270	Large	Small
MOFs	305 – 433	62 – 154	Small	Regular
Inorganic	953 – 1261	34 – 56	Insignificant	Large

Polymeric and organic materials show the largest energy exchanges, which makes them very attractive for latent heat TES. However, they undergo large volume changes and it is a problem for their containment, in addition to their small thermal stability. Some examples of the most common organic PCMs employed for TES were previously commented in section 1.1.3. due to their potential applications also for solid-state cooling. This is the case of neopentylglycol, pentaerythritol and pentaglycerine, three organic compounds with high latent heat (ranging from 102 J g^{-1} to 185 J g^{-1}), but whose cyclability and thermal stability are very small, in addition to be flammable.[141]

On the contrary, inorganics are much more stable in general, but their enthalpy changes are considerably smaller. Another drawback of inorganic materials may be the transition temperature range, which is too high in relation to the ambient temperature, if they are to be used for solar energy utilization. For solar TES it is required that the phase transition occurs in the temperature range from ~280 K to ~360 K, which are the temperatures achievable with sun energy along the planet (they can be higher or lower depending on the latitude).[138]

By combining inorganic and organic fragments in the same structure, it is possible to combine also the stability and small volume change of inorganics with the temperature range or operation of organics. This is the case of the MOFs, as can be seen in Table 1-2.

It is expected to have a similar effect in the case of the hybrid PCs, with a big potential for applications in TES technologies, as we have mentioned in section 1.1.3. In this context, some months after the start of this *doctoral thesis*, in 2019, it was reported a phase transition with a latent heat of 49.5 J g^{-1} in the organic-inorganic plastic crystal of formula $[(CH_3)_3N(CH_2Cl)]FeCl_4$.[111] This value is very high compared to inorganic materials and, furthermore, this hybrid PC has less volume change and higher thermal stability than the reported organic TES materials. Also, in addition to a more reversible phase transition than organic compounds, $[(CH_3)_3N(CH_2Cl)]FeCl_4$

shows switching in other interesting properties (electric and magnetic)[111], which opens up new possibilities of energy storage, in addition to using only the thermal behaviour.

Since many of the characteristics sought in materials for cooling applications (high energy exchange at phase transitions and transition temperatures near room temperature when seeking to valorize solar energy) coincide with the ideal properties of a good solar TES material, the strategy proposed in this work for the search of materials for TES is to explore the same materials that will be studied for cooling applications, starting with $[(CH_3)_3N(CH_2Cl)]FeCl_4$ and related materials, such as the non-reported hybrid PC $[(CH_3)_3S]FeCl_4$.

1.3. Advantages of HOIMs as multi-energy storage systems

A series of advantages have been proposed for the use of HOIMs as BC, as materials for TES, and even as multi-energy storage materials. That is why we have focused on HOIMs to find new systems for such applications. Some of their most important advantages, discussed so far, are worthy of being summarized:

- The presence of organic components in the structure provides a big disorder in the phase transitions. This can be associated to high entropy changes, which is a main requisite for cooling applications; and high latent heat, which is necessary for a high storage of thermal energy.
- The inorganic units provide stability to the solid phases. This means a higher thermal stability and higher melting and boiling points than purely-organic compounds, avoiding leakage, storage and transport problems and risks.
- Furthermore, the presence of metallic atoms can provide additional functional properties (besides thermo- and BC). The coexistence of properties such as magnetic, dielectric or ferroelectric, among others, enhances the functional value of HOIMs.[135–138]
- The above-mentioned coexistence of different properties can lead to the coexistence, also, of more than one mechanism in the phase transitions, which gives more potential for energetic applications.[82]
- Another attractive characteristic of hybrid materials for numerous applications is their processing. These materials need lower temperature treatment than pure inorganic materials for their processing. Their treatment is often closer to polymers due to their high organic content and also because of the formed cross-linked inorganic networks. Therefore, hybrid materials can be shaped in different ways, as in bulk, nanoparticles, films, etc.[82]
- Nowadays, HOIMs are used in several applications and they are part of daily life.[142] They have been used and studied as potential candidates for energy storage, electrocatalysis, supercapacitors, rechargeable lithium batteries, sensors, photovoltaics and so on.[90,143–147] Therefore, by now, much is known about their behavior under different conditions.

1.4. Main objectives

This introduction leads us to the general objective of this doctoral thesis, which is the study and development of hybrid organic-inorganic materials that present solid-solid phase transitions that make them good candidates for their use in solid-state cooling and/or thermal energy storage systems, as well as in multi-energy storage systems when the materials present other suitable transitions (e.g. electrical, magnetic,). No less important is the goal of deepening the understanding of the relationship between their structure and properties, in order to improve their performance and to develop more efficient systems.

Therefore, we have focused on the following hybrid systems:

1. The hybrid perovskite $[(CH_3)_4N]Mn(N_3)_3$, as good candidate to present adequate barocaloric properties to be used for solid-state cooling.

2. The hybrid plastic crystals $[(CH_3)_3(CH_2Cl)N]FeCl_4$, $[(CH_3)_3S]FeCl_4$ and $[(CH_3)_3(CH_2Cl)N]GaCl_4$, as good candidates for solid-state cooling, thermal and electric energy storage, and also for their potential magnetic properties.

In order to complete the proposed objectives, the methodology used was the following:

- The bibliographic search for a clear understanding of the research topics, as a contextualization of the state of the art.
- The selection of hybrid perovskites and hybrid plastic crystals in the literature that could show structural phase transitions and functional properties which could be modulated by different external stimuli. Those whose previous studies allow us to foresee that they will have the properties required for a good barocaloric or thermal energy storage material were selected.
- The design of new hybrid plastic crystals that could also display structural phase transitions, based on the knowledge and understanding of previously studied systems, in order to improve their properties.
- The synthesis of all those materials, and their compositional, structural and morphological characterization by using elemental analysis, X-ray diffraction, thermal analysis, electron microscopy, etc. Logically, the structural characterization as a function of temperature is a very important part.
- The calorimetric analysis as a function of temperature and external pressure, by differential scanning calorimetry, without and with applied external pressure (DSC and P-DSC).
- The study of the dielectric and magnetic properties, when appropriate, by impedance spectroscopy, electrical polarization measurements, magnetic susceptibility measurements and electron spin resonance, among others.

1.5. References

1   EU, *Regul. No 517/2014*, 2014, 57, 216.

2   O. Evans and J. Stevens, *The Young Steam Engineer's Guide*, Carey & Lea, 1805.

3   Perkins, J., British Patent 6662, 1834.

4   J. M. Calm, *Int. J. Refrig.*, 2008, 31, 1123–1133.

5   *Montreal Protocol on substances that deplete the ozone layer*, Montreal, Canada, 1987.

6   U. S. C. S. C. on F. Relations, *Amendment to the Montreal Protocol on Substances that Deplete the Ozone Layer*, Washington, D.C., 1993.

7   C. Norman, S. DeCanio and L. Fan, *Glob. Environ. Chang.*, 2008, 18, 330–340.

8   Y. T. Ge and S. A. Tassou, *Energy Convers. Manag.*, 2014, 78, 245–252.

9   A. Cavallini, G. Censi, D. Del Col, L. Doretti, G. A. Longo and L. Rossetto, *Int. J. Refrig.*, 2001, 24, 73–87.

10 V. W. Bhatkar, V. M. Kriplani and G. K. Awari, *Int. J. Environ. Sci. Technol.*, 2013, 10, 871–880.

11 A. Greco, C. Aprea, A. Maiorino and C. Masselli, *Int. J. Refrig.*, 2019, 106, 66–88.

12 A. Kitanovski, A., Tušek, J., Tomc, U., Plaznik, U., Ožbolt, M., & Poredoš, *Magnetocaloric Energy Conversion*, Springer I., 2015.

13 A. Kitanovski, U. Tomc and A. Poredo, *Int. J. Refrig.*, 2015, 57, 288–298.

14 L. Caron, N. Ba Doan and L. Ranno, *J. Phys. Condens. Matter*, 2017, 29, 7.

15 X. Moya, S. Kar-Narayan and N. D. Mathur, *Nat. Mater.*, 2014, 13, 439.

16 A. Kitanovski, *Adv. Energy Mater.*, 2020, 10, 1–34.

17 V. Franco, J. S. Blázquez, J. J. Ipus, J. Y. Law, L. M. Moreno-Ramírez and A. Conde, *Prog. Mater. Sci.*, 2018, 93, 112–232.

18 A. M. Tishin and Y. I. Spichkin, *Magnetocaloric Eff. its Appl.*, 2016, 1–475.

19 M. Valant, *Prog. Mater. Sci.*, 2012, 57, 980–1009.

20 R. Ma, Z. Zhang, K. Tong, D. Huber, R. Kornbluh, Y. S. Ju and Q. Pei, *Science*, 2017, 357, 1130–1134.

21 C. Cazorla, *Appl. Phys. Rev.*, 2019, 6, 4.

22 L. Mañosa and A. Planes, *Adv. Mater.*, 2017, 29, 11.

23 A. Greco, C. Aprea, A. Maiorino and C. Masselli, *Int. J. Refrig.*, 2019, 106, 66–88.

24 J. Tušek, K. Engelbrecht, R. Millán-solsona, L. Mañosa, E. Vives, L. P. Mikkelsen and N. Pryds, *Adv. Energy Mater.*, 2015, 5, 1–5.

25 H. Hou, P. Finkel, M. Staruch, J. Cui and I. Takeuchi, *Nat. Commun.*, 2018, 9, 1–8.

26 E. Stern-Taulats, T. Castán, L. Mañosa, A. Planes, N. D. Mathur and X. Moya, *MRS Bull.*, 2018, 43, 295–299.

27 J. M. Bermúdez-García, Doctoral Thesis, University of A Coruña, 2016.

28 L. Mañosa and A. Planes, *J. Phys. D. Appl. Phys.*, 2018, 51, 070201.

29 T. Gottschall, D. Benke, M. Fries, A. Taubel, I. A. Radulov, K. P. Skokov and O. Gutfleisch, *Adv. Funct. Mater.*, 2017, 27, 1–6.

30 C. Aprea, A. Greco, A. Maiorino and C. Masselli, *Energy*, 2018, 165, 439–455.

31 P. Papon, J. Leblond and P. H. E. Meijer, *Physics of Phase Transitions*, Springer, 2002.

32 C. N. R. Rao and J. Gopalakrishnan, *New Directions in Solid State Chemistry*, Cambridge University Press, 1997.

33 D. De Fontaine, *Solid state Phys.*, 1994, 47, 33–176.

34 Q. Shen, D. Zhao, W. Sun, Z. Wei and J. liu, *Intermetallics*, 2018, 100, 27–31.

35 X. He, S. Wei, Y. Kang, Y. Zhang, Y. Cao, K. Xu, Z. Li and C. Jing, *Scr. Mater.*, 2018, 145, 58–61.

36 P. J. Shamberger and F. S. Ohuchi, *Phys. Rev. B*, 2009, 79, 144407.

37 S. Qian, Y. Geng, Y. Wang, J. Ling, Y. Hwang, R. Radermacher, I. Takeuchi and J. Cui, *Int. J. Refrig.*, 2016, 64, 1–19.

38 D. Boldrin, *Appl. Phys. Lett.*, 2021, 118, 170502.

39 P. Lloveras, A. Aznar, M. Barrio, P. Negrier, C. Popescu, A. Planes, L. Mañosa, A. Avramenko, N. D. Mathur, X. Moya and J. Tamarit, *Nat. Commun.*, 2019, 10, 1803.

40 C. Nicolini, R. Ravindra, B. Ludolph and R. Winter, *Biophys. J.*, 2004, 86, 1385–1392.

41 S. Y. Dan'Kov, A. M. Tishin, V. K. Pecharsky and K. A. Gschneidner, *Phys. Rev. B*, 1998, 57, 3478.

42 P. Gütlich, H. A. Goodwin and Y. Garcia, *Spin crossover in transition metal compounds I*, Springer Science & Business Media, 2004, vol. 1.

43 R. K. Mishra, D. K. Pradhan, R. N. P. Choudhary and A. Banerjee, *J. Phys. Condens. Matter*, 2008, 20, 045218.

44 W. Zhong, D. Vanderbilt and K. M. Rabe, *Phys. Rev. B*, 1995, 52, 6301.

45 E. Stern-Taulats, P. Lloveras, M. Barrio, E. Defay, M. Egilmez, A. Planes, J.-L. Tamarit, L. Mañosa, N. D. Mathur and X. Moya, *APL Mater.*, 2016, 4, 91102.

46 P. Lloveras, M. Barrio, J. Tamarit, S. Crossley, W. Li, V. Pomjakushin, N. D. Mathur, X. Moya, A. Planes and L. Man, *Nat. Commun.*, 2015, 6, 8801.

47 J. Lin, P. Tong, X. Zhang, Z. Wang, Z. Zhang, B. Li, G. Zhong, J. Chen, Y. Wu and H. Lu, *Mater. Horizons*, 2020, 7, 2690–2695.

48 D. Halliday, R. Resnick and J. Walker, *Fundamentals of physics*, John Wiley & Sons, 2013.

49 K. J. Rao and C. N. R. Rao, *Br. J. Appl. Phys.*, 1966, 17, 1653–1654.

50   M. Natarajan, A. R. Das and C. N. R. Rao, *Trans. Faraday Soc.*, 1969, 65, 3081–3087.

51   J. M. Bermúdez-García, M. Sánchez-Andújar, S. Castro-García, J. López-Beceiro, R. Artiaga and M. A. Señarís-Rodríguez, *Nat. Commun.*, 2017, 8, 15715.

52   J. M. Bermúdez-García, M. Sánchez-Andújar and M. A. Señarís-Rodríguez, *J. Phys. Chem. Lett.*, 2017, 8, 4419–4423.

53   A. Aznar, P. Lloveras, M. Barrio, P. Negrier, A. Planes, L. Mañosa, N. Mathur, X. Moya and J. L. Tamarit, *J. Mater. Chem. A*, 2019, 8, 639–647.

54   A. Lázaro, E. Günther, H. Mehling, S. Hiebler, J. M. Mar\'\in and B. Zalba, *Meas. Sci. Technol.*, 2006, 17, 2168–2174.

55   C. Barreneche, A. Solé, L. Miró, I. Martorell, A. I. Fernández and L. F. Cabeza, *Thermochim. Acta*, 2013, 553, 23–26.

56   M. Szafrański, W.-J. Wei, Z.-M. Wang, W. Li and A. Katrusiak, *APL Mater.*, 2018, 6, 100701.

57   O. Gutfleisch, T. Gottschall, M. Fries, D. Benke, I. Radulov, K. P. Skokov, H. Wende, M. Gruner, M. Acet, P. Entel and M. Farle, *Philos. Trans. R. Soc. A Math. Phys. Eng. Sci.*, 2016, 374, 2074.

58   A. S. Mischenko, Q. Zhang, J. F. Scott, R. W. Whatmore and N. D. Mathur, *Science (80-.).*, 2006, 311, 1270–1271.

59   I. N. Flerov, M. V. Gorev, A. Tressaud and N. M. Laptash, *Crystallogr. Reports*, 2011, 56, 9–17.

60   T. Gottschall, M. D. Kuz'min, K. P. Skokov, Y. Skourski, M. Fries, O. Gutfleisch, M. G. Zavareh, D. L. Schlagel, Y. Mudryk, V. Pecharsky and J. Wosnitza, *Phys. Rev. B*, 2019, 99, 134429.

61   F. S. Guo, J. D. Leng, J. L. Liu, Z. S. Meng and M. L. Tong, *Inorg. Chem.*, 2012, 51, 405–413.

62   S. De Han, X. H. Miao, S. J. Liu and X. H. Bu, *Inorg. Chem. Front.*, 2014, 1, 549–552.

63   J. B. Peng, X. J. Kong, Q. C. Zhang, M. Orendáč, J. Prokleška, Y. P. Ren, L. S. Long, Z. Zheng and L. S. Zheng, *J. Am. Chem. Soc.*, 2014, 136, 17938–17941.

64   A. M. Aliev, A. B. Batdalov, L. N. Khanov, A. P. Kamantsev, V. V Koledov, A. V Mashirov, V. G. Shavrov, R. M. Grechishkin, A. R. Kaul' and V. Sampath, *Appl. Phys. Lett.*, 2016, 109, 202407.

65   K. Deepak and R. V. Ramanujan, *J. Alloys Compd.*, 2018, 743, 494–505.

66   M. H. Park, H. J. Kim, Y. J. Kim, T. Moon, K. Do Kim, Y. H. Lee, S. D. Hyun and C. S. Hwang, *Adv. Mater.*, 2016, 28, 7956–7961.

67   M. V Gorev, E. V Bogdanov and I. N. Flerov, *J. Phys. D. Appl. Phys.*, 2017, 50, 384002.

68   C. Aprea, A. Greco, A. Maiorino and C. Masselli, *Climate*, 2019, 7, 9.

69   L. Mañosa, A. Planes and M. Acet, *J. Mater. Chem. A*, 2013, 1, 4925–4936.

70   V. K. Pecharsky and K. A. Gschneidner Jr., *Phys. Rev. Lett.*, 1997, 78, 4494–4497.

71 A. Fujita, S. Fujieda, K. Fukamichi, H. Mitamura and T. Goto, *Phys. Rev. B*, 2001, 65, 14410.

72 I. N. Flerov, M. V Gorev, A. Tressaud and N. M. Laptash, *Crystallogr. Reports*, 2011, 56, 9–17.

73 P. Lloveras, E. Stern-Taulats, M. Barrio, J. L. Tamarit, S. Crossley, W. Li, V. Pomjakushin, A. Planes, L. Mañosa, N. D. Mathur and X. Moya, *Nat. Commun.*, 2015, 6, 8801.

74 A. Aznar, P. Lloveras, M. Romanini, M. Barrio, J. L. Tamarit, C. Cazorla, D. Errandonea, N. D. Mathur, A. Planes, X. Moya and L. Mañosa, *Nat. Commun.*, 2017, 8, 1.

75 L. Mañosa, D. González-Alonso, A. Planes, E. Bonnot, M. Barrio, J. L. Tamarit, S. Aksoy and M. Acet, *Nat. Mater.*, 2010, 9, 478–481.

76 S. Yuce, M. Barrio, B. Emre, E. Stern-Taulats, A. Planes, J. L. Tamarit, Y. Mudryk, K. A. Gschneidner, V. K. Pecharsky and L. Mañosa, *Appl. Phys. Lett.*, 2012, 101, 7.

77 E. Stern-Taulats, A. Planes, P. Lloveras, M. Barrio, J.-L. Tamarit, S. Pramanick, S. Majumdar, C. Frontera and L. Mañosa, *Phys. Rev. B*, 2014, 89, 214105.

78 D. Matsunami, A. Fujita, K. Takenaka and M. Kano, *Nat. Mater.*, 2015, 14, 73–78.

79 E. O. Usuda, N. M. Bom and A. M. G. Carvalho, *Eur. Polym. J.*, 2017, 92, 287–293.

80 J. M. Bermúdez-García, S. Yáñez-Vilar, A. García-Fernández, M. Sánchez-Andújar, S. Castro-García, J. López-Beceiro, R. Artiaga, M. Dilshad, X. Moya and M. A. Señarís-Rodríguez, *J. Mater. Chem. C*, 2018, 6, 9867–9874.

81 A. Aznar, P. Lloveras, J. Y. Kim, E. Stern-Taulats, M. Barrio, J. L. Tamarit, C. F. Sánchez-Valdés, J. L. Sánchez Llamazares, N. D. Mathur and X. Moya, *Adv. Mater.*, 2019, 31, 1–6.

82 G. Kickelbick, *Hybrid Materials*, John Wiley & Sons, Ltd, 1st edn., 2007, pp. 1–48.

83 C. N. R. Rao, A. K. Cheetham and A. Thirumurugan, *J. Phys. Condens. Matter*, 2008, 20, 83202.

84 G. Férey, *Chem. Soc. Rev.*, 2008, 37, 191–214.

85 A. K. K. Cheetham and C. N. R. Rao, *Mater. Sci.*, 2007, 318, 58–60.

86 C. Elschenbroich, *Organometallics*, Wiley, 2016.

87 A. García-Fernández, Doctoral Thesis, University of A Coruña, 2018.

88 D. Cherrad, D. Maouche, M. Reffas and A. Benamrani, *Solid State Commun.*, 2010, 150, 350–355.

89 K. Frohna and S. D. Stranks, *Hybrid perovskites for device applications*, Elsevier Ltd., 2nd edn., 2019.

90 T. M. Brenner, D. A. Egger, L. Kronik, G. Hodes and D. Cahen, *Nat. Rev. Mater.*, 2016, 1, 15007.

91 W. Li, Z. Wang, F. Deschler, S. Gao, R. H. Friend and A. K. Cheetham, *Nat. Rev. Mater.*, 2017, 2, 16099.

92 V. M. Goldschmidt, *Naturwissenschaften*, 1926, 14, 477–485.

93   G. Kieslich, S. Sun and A. K. Cheetham, *Chem. Sci.*, 2015, 6, 3430–3433.

94   G. Kieslich, S. Sun and A. K. Cheetham, *Chem. Sci.*, 2014, 5, 4712–4715.

95   D. Di Sante, A. Stroppa, P. Jain and S. Picozzi, *J. Am. Chem. Soc.*, 2013, 135, 18126–18130.

96   R. Shang, S. Chen, B.-W. Wang, Z.-M. Wang and S. Gao, *Angew. Chemie Int. Ed.*, 2016, 55, 2097–2100.

97   L.-J. Ji, S.-J. Sun, Y. Qin, K. Li and W. Li, *Coord. Chem. Rev.*, 2019, 391, 15–29.

98   J. M. Bermúdez-García, M. Sánchez-Andújar, S. Yáñez-Vilar, S. Castro-García, R. Artiaga, J. López-Beceiro, L. Botana, Á. Alegría and M. A. Señarís-Rodríguez, *Inorg. Chem.*, 2015, 54, 11680–11687.

99   B. K. Shaw, A. R. Hughes, M. Ducamp, S. Moss, A. Debnath, A. F. Sapnik, M. F. Thorne, L. N. McHugh, A. Pugliese, D. S. Keeble, P. Chater, J. M. Bermudez-Garcia, X. Moya, S. K. Saha, D. A. Keen, F. X. Coudert, F. Blanc and T. D. Bennett, *Nat. Chem.*, 2021, 13, 778–785.

100 L. C. Gómez-Aguirre, B. Pato-Doldán, A. Stroppa, L. M. Yang, T. Frauenheim, J. Mira, S. Yáñez-Vilar, R. Artiaga, S. Castro-García, M. Sánchez-Andújar and M. A. Señarís-Rodríguez, *Chem. - A Eur. J.*, 2016, 22, 7863–7870.

101 J. Timmermans, *J. Phys. Chem. Solids*, 1961, 18, 1–8.

102 L. A. K. Staveley, *Annu. Rev. Phys. Chem.*, 1962, 13, 351–368.

103 B. Li, Y. Kawakita, S. Ohira-Kawamura, T. Sugahara, H. Wang, J. Wang, Y. Chen, S. I. Kawaguchi, S. Kawaguchi, K. Ohara, K. Li, D. Yu, R. Mole, T. Hattori, T. Kikuchi, S. ichiro Yano, Z. Zhang, Z. Zhang, W. Ren, S. Lin, O. Sakata, K. Nakajima and Z. Zhang, *Nature*, 2019, 567, 506–510.

104 J. Even, M. Carignano and C. Katan, *Nanoscale*, 2016, 8, 6222–6236.

105 X. G. Chen, Y. Z. Zhang, D. S. Sun, J. X. Gao, X. N. Hua and W. Q. Liao, *Dalt. Trans.*, 2019, 48, 11292–11297.

106 T. Mochida, M. Ishida, T. Tominaga, K. Takahashi, T. Sakurai and H. Ohta, *Phys. Chem. Chem. Phys.*, 2018, 20, 3019–3028.

107 A. García-Saiz, P. Migowski, O. Vallcorba, J. Junquera, J. A. Blanco, J. A. González, M. T. Fernández-Díaz, J. Rius, J. Dupont, J. Rodríguez Fernández and I. De Pedro, *Chem. - A Eur. J.*, 2014, 20, 72–76.

108 I. De Pedro, A. García-Saiz, J. González, I. Ruiz De Larramendi, T. Rojo, C. A. M. Afonso, S. P. Simeonov, J. C. Waerenborgh, J. A. Blanco, B. Ramajo and J. R. Fernández, *Phys. Chem. Chem. Phys.*, 2013, 15, 12724–12733.

109 J. Harada, N. Yoneyama, S. Yokokura, Y. Takahashi, A. Miura, N. Kitamura and T. Inabe, *J. Am. Chem. Soc.*, 2018, 140, 346–354.

110 J. Estager, J. D. Holbrey and M. Swadźba-Kwaśny, *Chem. Soc. Rev.*, 2014, 43, 847–886.

111 D. Li, X. M. Zhao, H. X. Zhao, L. S. Long and L. S. Zheng, *Inorg. Chem.*, 2019, 58, 655–662.

112   A. Basile, M. Hilder, F. Makhlooghiazad, C. Pozo-Gonzalo, D. R. MacFarlane, P. C. Howlett and M. Forsyth, *Adv. Energy Mater.*, 2018, 8, 1703491.

113   B. D. R. Macfarlane and M. Forsyth, *Adv. Mater.*, 2001, 12, 957–966.

114   X. Zheng, P.-P. Shi, Y. Lu, L. Zhou, J.-X. Gao, F.-J. Geng, D.-H. Wu, D.-W. Fu and Q. Ye, *Inorg. Chem. Front.*, 2017, 4, 1445–1450.

115   L. Ye, Z.-X. Gong, C. Shi, J.-J. Ma, H. Liang, F.-W. Qi, D.-Y. E, C.-F. Wang, Y. Zhang and H.-Y. Ye, *CrystEngComm*, 2019, 21, 7043–7047.

116   J. Walker, R. Miranti, S. L. Skjærvø, T. Rojac, T. Grande and M. A. Einarsrud, *J. Mater. Chem. C*, 2020, 8, 3206–3216.

117   J. Binns, G. J. McIntyre, J. A. Barreda-Argüeso, J. González, F. Aguado, F. Rodríguez, R. Valiente and S. Parsons, *Acta Crystallogr. Sect. B Struct. Sci. Cryst. Eng. Mater.*, 2017, 73, 844–855.

118   Z.-X. Zhang, T. Zhang, P.-P. Shi, W.-Y. Zhang, Q. Ye and D.-W. Fu, *Inorg. Chem. Front.*, 2020, 7, 1239–1249.

119   IEA, *https://www.iea.org/reports/renewables-2019*, 2019, Paris (accessed May 02, 2020).

120   B. C. Liu, F. Li, L. Ma and H. Cheng, *Adv. Energy Mater.*, 2010, 22, 28–62.

121   J. Mohtasham, *Energy Procedia*, 2015, 74, 1289–1297.

122   O. Ellabban, H. Abu-Rub and F. Blaabjerg, *Renew. Sustain. Energy Rev.*, 2014, 39, 748–764.

123   C. Bussar, P. Stöcker, Z. Cai, L. Moraes Jr, D. Magnor, P. Wiernes, N. van Bracht, A. Moser and D. U. Sauer, *J. Energy Storage*, 2016, 6, 1–10.

124   R. A. Huggins, *Energy storage*, New York: Springer, 2nd edn., 2010.

125   A. Sani Hassan, L. Cipcigan and N. Jenkins, *Appl. Energy*, 2017, 203, 422–441.

126   A. R. Dehghani-Sanij, E. Tharumalingam, M. B. Dusseault and R. Fraser, *Renew. Sustain. Energy Rev.*, 2019, 104, 192–208.

127   A. Rimpel, K. Krueger, Z. Wang, X. Li, A. Palazzolo, J. Kavosi, M. Naraghi, T. Creasy, B. Anvari and E. Severson, in *Thermal, Mechanical, and Hybrid Chemical Energy Storage Systems*, Elsevier, 2021, pp. 139–247.

128   J. B. Goodenough, *Energy Environ. Sci.*, 2014, 7, 14–18.

129   A. Aho, M. Antonietti, S. Arndt, M. Behrens, E. Bill, A. Brandner, G. Centi, P. Claus, N. Cox and S. DeBeer, *Chemical energy storage*, Walter de Gruyter, 2012.

130   L. F. Cabeza, *Compr. Renew. energy*, 2012, 3, 211–253.

131   L. Navarro, A. de Gracia, S. Colclough, M. Browne, S. J. McCormack, P. Griffiths and L. F. Cabeza, *Renew. Energy*, 2016, 88, 526–547.

132   I. Sarbu and C. Sebarchievichi, *Sustainability*, 2018, 10, 191.

133   M. Ebrahimi and A. Keshavarz, *Combined cooling, heating and power: Decision-making, design and optimization*, Elsevier, 2014.

134 V. Palomba, V. Brancato and A. Frazzica, *Appl. Energy*, 2017, 199, 347–358.

135 S. D. Sharma and K. Sagara, *Int. J. Green Energy*, 2005, 2, 1–56.

136 M. Medrano, A. Gil, I. Martorell, X. Potau and L. F. Cabeza, 2010, 14, 56–72.

137 J. Pereira da Cunha and P. Eames, *Appl. Energy*, 2016, 177, 227–238.

138 M. M. Farid, A. M. Khudhair, S. Ali and K. Razack, 2004, 45, 1597–1615.

139 E. Moreles, G. Huelsz and G. Barrios, *Build. Simul.*, 2018, 11, 519–531.

140 A. F. Regin, S. C. Solanki and J. S. Saini, *Renew. Sustain. Energy Rev.*, 2008, 12, 2438–2458.

141 A. Fallahi, G. Guldentops, M. Tao, S. Granados-Focil and S. Van Dessel, *Appl. Therm. Eng.*, 2017, 127, 1427–1441.

142 C. Sanchez, K. J. Shea and S. Kitagawa, *Chem. Soc. Rev.*, 2011, 40, 471–472.

143 E. Shouji and D. A. Buttry, *Langmuir*, 1999, 15, 669–673.

144 Y. Liang, Y. Li, H. Wang and H. Dai, *ChemInform*, 2013, 44, 21.

145 M. Skunik, P. J. Kulesza, N. Vlachopoulos, L. Häggman and A. Hagfeldt, *ECS Trans.*, 2011, 35, 25.

146 K. S. Yoneyama H., Kishimoto A., *Chem. Commun.*, 1991, 986, 6–7.

147 E. Bescher and J. D. Mackenzie, *Mater. Sci. Eng. C*, 1998, 6, 145–154.

Chapter 2

Chapter 2
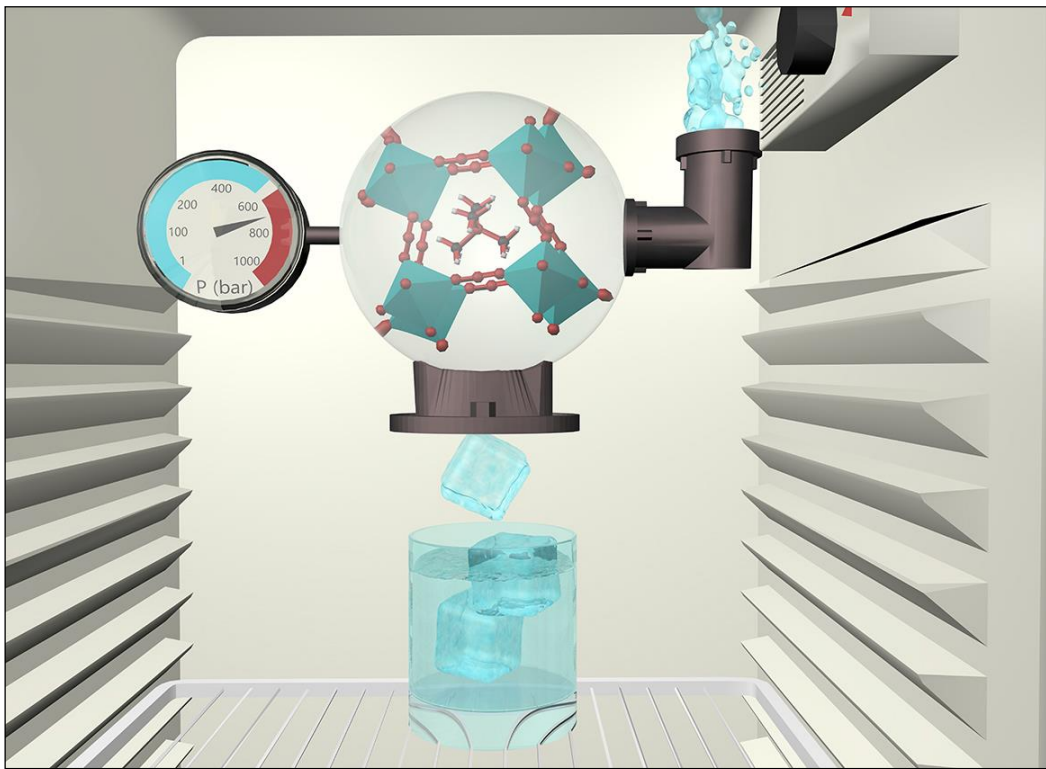
$[(CH_3)_4N]Mn(N_3)_3$

Giant barocaloric effect near room temperature in the multiferroic $[(CH_3)_4N]Mn(N_3)_3$ hybrid perovskite

Abstract: In this chapter, it is reported a giant reversible barocaloric effect in $[(CH_3)_4N]Mn[N_3]_3$ hybrid organic–inorganic perovskite, near its first-order cubic-monoclinic structural phase transition at T_0 ~305 K. When driving the transition thermally at atmospheric pressure, the transition displays a large change in entropy of ~80 J K^{-1} kg^{-1} and a small thermal hysteresis of ~7 K, as well as a large change in volume of ~1.5%. When driving the transition with pressure near room temperature, the transition displays large changes in entropy of ~70 J K^{-1} kg^{-1}, which represent a giant barocaloric response. Hybrid perovskites with similar barocaloric response and lower operating temperatures may find applications in environmentally friendly cooling.

2.1. Introduction

In recent years, barocaloric materials have arisen as promising solid-state replacements to commercial refrigerant fluids, which are strong volatile greenhouse contributors that are often flammable or toxic.[1–3] Similarly to refrigerant fluids, barocaloric materials display large thermal changes under application and removal of hydrostatic pressure, which are typically parameterised as pressure-driven isothermal changes in entropy ΔS, or pressure-driven adiabatic changes in temperature ΔT.[1] However, due to their solid nature, barocaloric materials ultimately represent an environmentally friendly cooling solution.

With this motivation, a number of materials families have been investigated for barocaloric applications, which include magnetic alloys,[4–9] polymers,[10] oxyflourides,[11–14] ferroelectric oxides,[15,16] ferrielectric salts,[17] superionic conductors,[18,19] plastic crystals,[20–23] and hybrid organic–inorganic perovskites.[24,25] The latter have the potential to operate at hydrostatic pressures that are similar to those available in commercial compressors ($\leq$150 bar), specifically in the case of dicyanamide hybrid perovskites.[24,25] Moreover, hybrid perovskites have the advantage that they can be synthesized using fast, economic, simple and escalable methods, and their chemical composition can be easily modified by using different building-blocks, which can lead to an optimization of their barocaloric parameters depending on the application of interest.[26]

Dicyanamide perovskites have been shown to display giant barocaloric effects only at temperatures well above room temperature ($\geq$330 K).[24,25] Here the operating temperature of hybrid perovskites is brought closer to room temperature, by demonstrating giant barocaloric effects in a $[(CH_3)_4N]Mn[N_3]_3$ azide perovskite at ~310 K and above. Near its non-isochoric cubic ($Pm\overline{3}m$) to monoclininc ($P2_1/m$) phase transition,[27,28] there were found pressure-driven entropy changes $|\Delta S|$ of ~70 J K^{-1} kg^{-1} that can be driven reversibly using changes in applied pressure p of $|\Delta p| = |p - p_{atm}| \sim |p| \sim 1$ kbar (p_{atm} is atmospheric pressure). These results improve upon the performance of state-of-the-art barocaloric hybrid perovskites, by increasing twofold or more the barocaloric entropy change, and decreasing operating temperatures by ~25 K or more, at the expense of larger driving pressures.

2.2. Experimental section

2.2.1. Materials

The following chemicals were used in the synthesis as-puchased and without further purification: $MnCl_2 \cdot 4H_2O$ ($\geq$98%, Aldrich), $[(CH_3)_4N]Cl$ (purum $\geq$98%, Fluka), NaN_3 ($\geq$99%, Aldrich) and CH_3OH (99.5%, Panreac).

Caution: Azide compounds can be potentially explosive and should be handled with caution.

2.2.2. Synthesis

Colourless polycrystalline powders of $[(CH_3)_4N]Mn[N_3]_3$ were synthesised via liquid diffusion.[27,28] 0.5 M of NaN_3 and 0.5 M of $[(CH_3)_4N]Cl$ were dissolved in a 1 : 1 mixture of methanol :water of volume 2.5 mL, in a glass tube. The solution was then covered by 1 ml of methanol, followed by 4 ml of 0.1 M of $MnCl_2 \cdot 4H_2O$ (0.1 M) in methanol, and the glass tube was sealed. Polycrystalline powders $[(CH_3)_4N]Mn[N_3]_3$ were obtained after leaving the sealed glass tube undisturbed for three days.

2.2.3. Powder X-ray diffraction

Powder X-ray diffraction at room temperature was performed using a Siemens D-5000 diffractometer,

with CuKa radiation (λ = 1.5418 Å). The recorded spectra was compared with an spectra that was simulated using existing single-crystal data and Mercury 3.5.1 software.

Variable-temperature powder X-ray diffraction using λ = 0.412483 Å at beamline BL04 – MSPD, Alba Synchrotron. For this experiment, ~5 mg of $[(CH_3)_4N]Mn(N_3)_3$ were inserted in a borosilicate capillary of diameter ϕ = 0.5 mm, and the capillary was rotated during data collection. The recorded patterns were fitted using the Le Bail method.

2.2.4. Differential scanning calorimetry

Variable-pressure differential scanning calorimetry was performed using a Setaram μDSC7 EVO microcalorimeter equipped with a 260D Isco pressure pump that utilised nitrogen gas a pressuretransmitting media. Samples of ~100 mg of $[(CH_3)_4N]Mn(N_3)_3$ were inserted in commercial pressure sample holders provided by Setaram and connected to the Isco pump. For quasi-direct barocaloric measurements, samples were swept in temperature at ±1.2 K min^{-1}. For direct barocaloric measurements, the same amount of sample was swept in pressure at -10 bar min^{-1}.

2.3. Results and discussion

2.3.1. Powder X-ray diffraction

X-ray diffraction data taken on the synthesized powder at atmospheric pressure and room temperature confirmed singlephase character (Fig. 2-1).
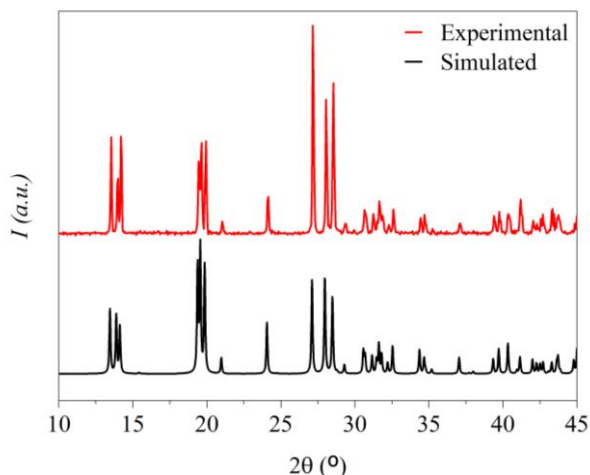

Figure 2-1. Powder x-ray diffraction patterns at room temperature for the $[(CH_3)_4N]Mn[N_3]_3$ compound as-prepared in this work (red pattern) and simulated from the single crystal structure at room temperature (black pattern).

Variable-temperature powder X-ray diffraction data (Fig. 2-2a) revealed a large increase in specific volume of $|\Delta V_0|$ ~ 9.40 ± 0.03 x 10^{-6} m^3 kg^{-1} on heating across the

transition, which represents a relative change of ~1.5%. The Clausius–Clapeyron equation $(dT_0/dp) = (\Delta V_0/\Delta S_0)$ returns a value of barocaloric tunability[25] dT_0/dp of ~11.7 K kbar^{-1} that is large but smaller than those obtained in dicyanamide perovskites.[24,25]

2.3.2. Differential scanning calorimetry

Differential scanning calorimetry at atmospheric pressure (Fig. 2-2b) confirmed the first-order cubic-monoclinic phase transition at T_h ~ 309 K on heating (identified using the peak in heat flow $dQ/|dT|$), and at T_c ~ 302 K on cooling (identified using the peak in heat flow $dQ/|dT|$), with a small thermal hysteresis of $\Delta T = T_h - T_c$ ~ 7 K. The thermally driven latent heat and entropy change for the transition (obtained via suitable integration[1,2] of the peaks in heat flow $dQ/|dT|$) where $|Q_0|$ ~ 25 kJ kg^{-1} and $|\Delta S_0|$ ~ 80 J K^{-1} kg^{-1}, respectively, in good agreement with literature values.[27,28]
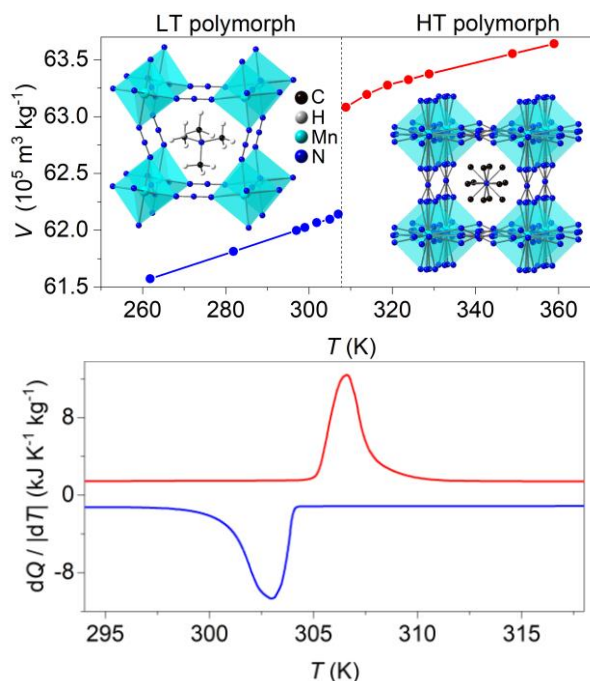
Figure 2-2. (a) Specific volume as a function of temperature, at atmospheric pressure, measured on heating via variable-temperature synchrotron powder X-ray diffraction. Left inset: pseudo-cubic representation of the low-temperature monoclinic phase; right inset: pseudo-cubic representation of the high-temperature cubic phase. H atoms in the high temperature phase are omitted for clarity of visualisation. (b) Heat flow $dQ/|dT|$ as a function of temperature, at atmospheric pressure.

The large values of $|Q_0|$ and $|\Delta S_0|$ arise primarily due to large changes in the degree of ordering[27] of the nitrogen atoms within the azide ligands (N_3), and of the monoclinic phase, $N = \exp(\Delta S_0/R)$, is ~12 (R is the universal gas constant). When undergoing the phase transition from the monoclinic to the cubic phase, the azide N atoms get disordered over 4 different positions and the tetramethylammonium C atoms get disorder over twelve

different positions.[27] This type of order–disorder phase transitions have been identified as mechanisms for potential barocaloric effects.[29]

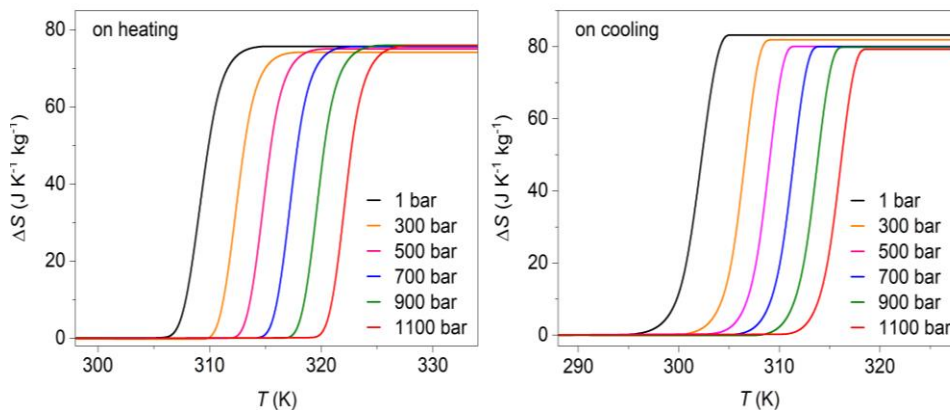Variable-pressure differential scanning calorimetry (Fig. 2-3a) confirmed the calculated barocaloric tunability, with $dT_h/dp \sim dT_c/dp \sim 12$ K kbar^{-1} (Fig. 2-3b). Using these quasi-direct measurements[1], the difference between thermally driven changes in entropy measured at two different pressures (Fig. 2-4) was taken to calculate pressure-driven isothermal changes in entropy (Fig. 2-5).

Giant isothermal changes in entropy $|\Delta S|$ of ~33 J K^{-1} kg^{-1} that can be driven reversibly using changes in applied pressure of ~0.7 kbar were found. On increasing applied pressure further, it is found a $|\Delta S|$ of ~70 J K^{-1} kg^{-1} for $|p|$ ~ 1.1 kbar, which is in agreement with a previous indirect prediction.[26]

The calculated pressure-driven changes in entropy were confirmed via direct measurements[1] of barocaloric heat (Fig. 2-6), which are rare, as few existing calorimeters permit the application of variable pressure. At 311 K, application and removal of ~900 bar drives reversibly the largest barocaloric entropy change of $|\Delta S|$ ~ 70 J K^{-1} kg^{-1} (obtained via suitable integration of the peaks in heat flow $dQ/|dp|$).

Figure 2-3. (a) Heat flow $dQ/|dT|$ as a function of temperature, at finite applied pressures. (b) Transition temperatures versus pressure, identified using the peak in heat flow $dQ/|dT|$.

Figure 2-5. Pressure-driven isothermal changes in entropy on applying (0 → p) and removing (p → 0) selected hydrostatic pressures. Data shaded using different colours represent the reversible[18] barocaloric response at different pressures.
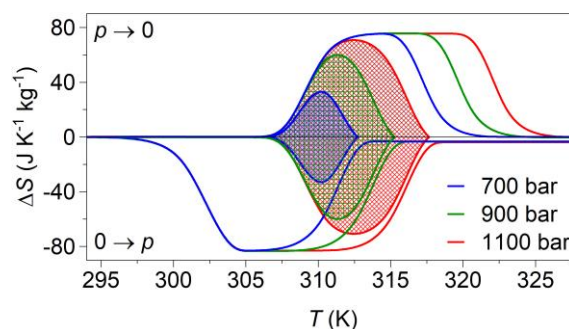
Additional changes in isothermal entropy[17] that arise due to volumetric thermal expansion either side of the transition (Fig. 2-2a) were not considered because the coefficient of thermal expansion may decrease significantly under pressure for this compound.[30] These additional changes —if taken into account— will increase the magnitude of the here presented barocaloric effect, so the values of ΔS that are presented are underestimated.

At higher temperatures, higher pressures are required to drive the transition reversibly but $|\Delta S|$ remains nominally constant. [(CH$_3$)$_4$N]Mn[N$_3$]$_3$ improves upon the performance of [TPrA]Mn[dca]$_3$ and [TPrA]Cd[dca]$_3$ dicyanamide perovskites (Table 1), by increasing twofold or more the barocaloric entropy change, and decreasing operating temperatures by ~25 K or more, at the expense of larger driving pressures.

Figure 2-4. Change in entropy calculated for the thermally-induced phase transition of [(CH$_3$)$_4$N]Mn[N$_3$]$_3$ hybrid perovskites at different isostatic pressures on heating (left) and cooling (right)

Table 2-1. Comparison of the barocaloric parameters for the best hybrid, organic and inorganic barocaloric materials up to the date of publication of this work, September 2020. T_0 = transition temperature averaged from the peaks maximum on heating and cooling, T_h - T_c = thermal hysteresis calculated from the peaks maximum on heating and cooling, $|\Delta S_0|$ = thermally driven entropy change averaged from peaks integration on heating and cooling, $|\Delta V_0|$ = volume change calculated on heating, $|dT_0/dp|$ = barocaloric tunability averaged from heating and cooling, $|\Delta S|$ = reversible pressure-driven isothermal entropy change obtained by quasi-direct methods, Δp = corresponding driving pressure for $|\Delta S|$.

	Barocaloric material	T_0 (K)	T_h-T_c (K)	$|\Delta S_0|$ (J K^{-1} kg^{-1})	$|\Delta V_0|$ (10^{-6} m^3 kg^{-1})	$|dT_0/dp|$ (K kbar^{-1})	$|\Delta S|$ (J K kg^{-1})	Δp (bar)	Ref.
Hybrid	[(CH$_3$)$_4$N]Mn[N$_3$]$_3$	305	7	80	90.4	12	70	900	This work
	[TPrA]Mn[dca]$_3$	330	0.9	42.5	10	23.1	30.5	70	24
	[TPrA]Cd[dca]$_3$	386	1.4	16.2	5.3	38.2	11.5	70	25
Organics	(CH$_3$)$_2$C(CH$_2$OH)$_2$	311	25	372	46	10.3	445	2500	20
	(CH$_3$)C(CH$_2$OH)$_3$	354	12	482	38	8.7	490	2400	21
	(CH$_3$)$_3$C(CH$_2$OH)	251	33	200.5	45.5	17	290	2600	21
	Fullerite C$_{60}$	257	3	26.5	4.6	17	42	4100	23
Inorganics	(NH$_4$)$_2$SO$_4$	222	3	65	2.9	5.1	60	1000	17
	AgI	420	24	64	7.4	13.4	60	2500	18
	Fe$_{49}$Rh$_{51}$	314	10	12.5	1	5.9	12.5	2500	7
	MnCoGeB$_{0.03}$	290	18	47	5	10	30	1700	9
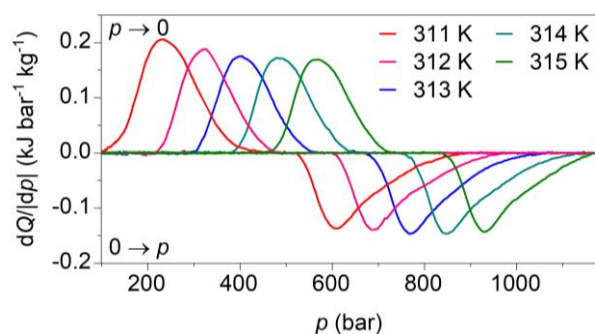
Figure 2-6. Heat flow dQ/dp| on applying (0 → p) and removing (p → 0) hydrostatic pressure, after baseline subtraction, at different temperters.

The larger barocaloric entropy change arises due to the larger change in configurational order when driving the transition with pressure, *cf.* N ~12 for [(CH$_3$)$_4$N]Mn[N$_3$]$_3$, whereas it is ~8 and ~2.6 for the Mn-dicyanamide perovskite and the Cd-dicyanamide perovskite, respectively. The lower transition temperatures may arise due to a lower Goldschmidt tolerance factor, which is close to the ideal value of 1[31,32] for [(CH$_3$)$_4$N]Mn[N$_3$]$_3$. The higher driving pressure is a consequence of the smaller barocaloric tunability, (dT_0/dp) = ($\Delta V_0/\Delta S_0$), as expected for systems with similar ΔV_0 but larger ΔS_0. Moreover, a larger thermal hysteresis also contributes to the need of a larger driving pressure for obtaining a reversible barocaloric effect upon cycling.

2.4. Conclusions

In conclusion, when comparing the azide perovskite with the best barocaloric organic and/or inorganic materials up to when these results were published (2020), this perovskite exhibited a larger reversible barocaloric effect than most of the listed materials (except polyalcohols), with the advantage of working under lower pressures (Table 2-1). In the future, it will be interesting to explore multicaloric effects[33] in this (and related) compounds, given that the monoclinc phase of [(CH$_3$)$_4$N]Mn[N$_3$]$_3$ is magnetic and antiferroelectric.[27]

2.5. Notes

The work showed and discussed in this chapter has been published in the following article:

2.6. References

1   X. Moya, S. Kar-Narayan and N. D. Mathur, *Nat. Mater.*, 2014, 13, 439–450.

2   L. Mañosa and A. Planes, *Adv. Mater.*, 2017, 29, 11.

3   S. Crossley, N. D. Mathur and X. Moya, *Aip Adv.*, 2015, 5, 67153.

4   S. Yuce, M. Barrio, B. Emre, E. Stern-Taulats, A. Planes, J. L. Tamarit, Y. Mudryk, K. A. Gschneidner, V. K. Pecharsky and L. Mañosa, *Appl. Phys. Lett.*, 2012, 101, 7.

5   L. Mañosa, D. González-Alonso, A. Planes, M. Barrio, J. L. Tamarit, I. S. Titov, M. Acet, A. Bhattacharyya and S. Majumdar, *Nat. Commun.*, 2011, 2, 1–5.

6   L. Mañosa, D. González-Alonso, A. Planes, E. Bonnot, M. Barrio, J. L. Tamarit, S. Aksoy and

M. Acet, *Nat. Mater.*, 2010, 9, 478–481.

7   E. Stern-Taulats, A. Planes, P. Lloveras, M. Barrio, J.-L. Tamarit, S. Pramanick, S. Majumdar, C. Frontera and L. Mañosa, *Phys. Rev. B*, 2014, 89, 214105.

8   D. Matsunami, A. Fujita, K. Takenaka and M. Kano, *Nat. Mater.*, 2015, 14, 73–78.

9   A. Aznar, P. Lloveras, J. Kim, E. Stern-Taulats, M. Barrio, J. L. Tamarit, C. F. Sánchez-Valdés, J. L. Sánchez Llamazares, N. D. Mathur and X. Moya, *Adv. Mater.*, 2019, 31, 1903577.

10 E. L. Rodriquez and F. E. Filisko, *J. Appl. Phys.*, 1982, 53, 6536–6540.

11 I. N. Flerov, A. V Kartashev, M. V Gorev, E. V Bogdanov, S. V Mel'Nikova, M. S. Molokeev, E. I. Pogoreltsev and N. M. Laptash, *J. Fluor. Chem.*, 2016, 183, 1–9.

12 M. V Gorev, E. V Bogdanov, I. N. Flerov, A. G. Kocharova and N. M. Laptash, *Phys. Solid State*, 2010, 52, 167–175.

13 M. V Gorev, I. N. Flerov, E. V Bogdanov, V. N. Voronov and N. M. Laptash, *Phys. Solid State*, 2010, 52, 377–383.

14 I. N. Flerov, M. V. Gorev, A. Tressaud and N. M. Laptash, *Crystallogr. Reports*, 2011, 56, 9–17.

15 E. Stern-Taulats, P. Lloveras, M. Barrio, E. Defay, M. Egilmez, A. Planes and J.-L. Tamarit, *APL Mater.*, 2016, 4, 91102.

16 Y. Liu, J. Wei, P.-E. Janolin, I. C. Infante, X. Lou and B. Dkhil, *Appl. Phys. Lett.*, 2014, 104, 162904.

17 P. Lloveras, E. Stern-Taulats, M. Barrio, J. L. Tamarit, S. Crossley, W. Li, V. Pomjakushin, A. Planes, L. Mañosa, N. D. Mathur and X. Moya, *Nat. Commun.*, 2015, 6, 8801.

18 A. Aznar, P. Lloveras, M. Romanini, M. Barrio, J. L. Tamarit, C. Cazorla, D. Errandonea, N. D. Mathur, A. Planes, X. Moya and L. Mañosa, *Nat. Commun.*, 2017, 8, 1.

19 J. Min, A. K. Sagotra and C. Cazorla, *Phys. Rev. Mater.*, 2020, 4, 15403.

20 P. Lloveras, A. Aznar, M. Barrio, P. Negrier, C. Popescu, A. Planes, L. Mañosa, A. Avramenko, N. D. Mathur, X. Moya and J. Tamarit, *Nat. Commun.*, 2019, 10, 1803.

21 A. Aznar, P. Lloveras, M. Barrio, P. Negrier, A. Planes, L. Mañosa, N. Mathur, X. Moya and J. L. Tamarit, *J. Mater. Chem. A*, 2020, 8, 639–647.

22 B. Li, Y. Kawakita, S. Ohira-Kawamura, T. Sugahara, H. Wang, J. Wang, Y. Chen, S. I. Kawaguchi, S. Kawaguchi, K. Ohara, K. Li, D. Yu, R. Mole, T. Hattori, T. Kikuchi, S. ichiro Yano, Z. Zhang, Z. Zhang, W. Ren, S. Lin, O. Sakata, K. Nakajima and Z. Zhang, *Nature*, 2019, 567, 506–510.

23 J. Li, D. Dunstan, X. Lou, A. Planes, L. Mañosa, M. Barrio, J.-L. Tamarit and P. Lloveras, *J. Mater. Chem. A*, 2020, 8, 20354–20362.

24 J. M. Bermúdez-García, M. Sánchez-Andújar, S. Castro-García, J. López-Beceiro, R. Artiaga and M. A. Señarís-Rodríguez, *Nat. Commun.*, 2017, 8, 15715.

25 J. M. Bermúdez-García, S. Yáñez-Vilar, A. García-Fernández, M. Sánchez-Andújar, S. Castro-García, J. López-Beceiro, R. Artiaga, M. Dilshad, X. Moya and M. A. Señarís-Rodríguez, *J. Mater. Chem. C*, 2018, 6, 9867–9874.

26 J. M. Bermúdez-García, M. Sánchez-Andújar and M. A. Señarís-Rodríguez, *J. Phys. Chem. Lett.*, 2017, 8, 4419–4423.

27 L. C. Gómez-Aguirre, B. Pato-Doldán, A. Stroppa, L. M. Yang, T. Frauenheim, J. Mira, S. Yáñez-Vilar, R. Artiaga, S. Castro-García, M. Sánchez-Andújar and M. A. Señarís-Rodríguez, *Chem. - A Eur. J.*, 2016, 22, 7863–7870.

28 F. A. Mautner, S. Hanna, R. Cortés, L. Lezama, M. G. Barandika and T. Rojo, *Inorg. Chem.*, 2002, 38, 4647–4652.

29 C. Cazorla, *Appl. Phys. Rev.*, 2019, 6, 4.

30 D. Walsh and P. Zoller, *Standard Pressure Volume Temperature Data for Polymers*, Taylor \& Francis, 1995.

31 G. Kieslich, S. Sun and A. K. Cheetham, *Chem. Sci.*, 2015, 6, 3430–3433.

32 J. M. Bermúdez-García, M. Sánchez-Andújar, S. Yáñez-Vilar, S. Castro-García, R. Artiaga, J. López-Beceiro, L. Botana, Á. Alegría and M. A. Señarís-Rodríguez, *Inorg. Chem.*, 2015, 54, 11680–11687.

33 E. Stern-Taulats, T. Castán, L. Mañosa, A. Planes, N. D. Mathur and X. Moya, *MRS Bull.*, 2018, 43, 295–299.

Chapter 3
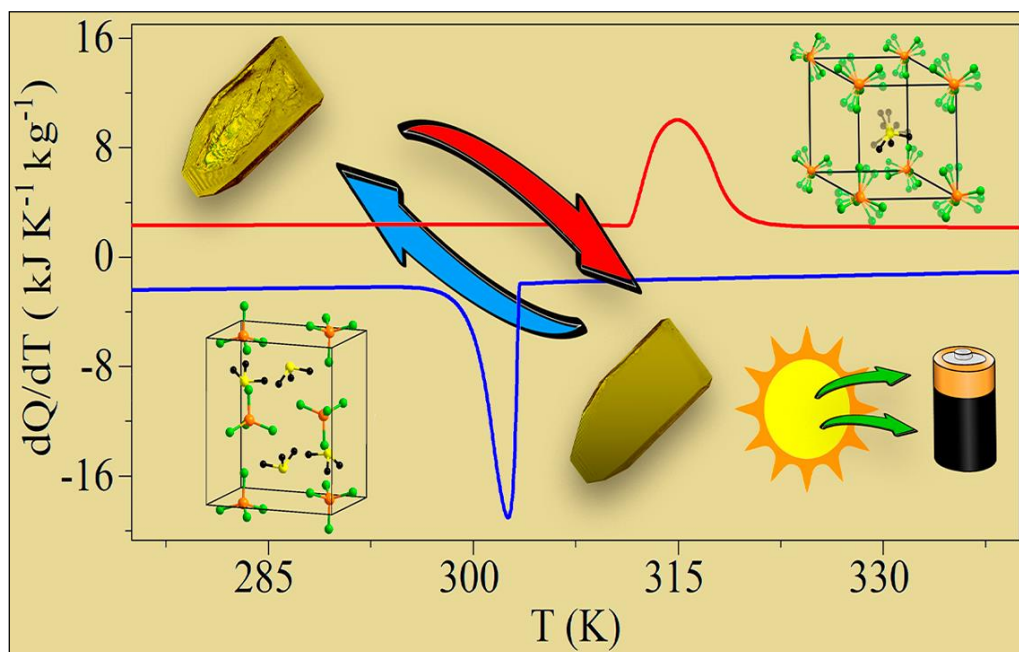
Chapter 3

[(CH₃)₃S]FeCl₄

Multifunctional properties and multi-energy storage in the [(CH₃)₃S]FeCl₄ plastic crystal

Abstract: In this work, a new halometallate [(CH₃)₃S]FeCl₄ with plastic crystal behavior is reported as a new material for multi-energy storage. This material undergoes a first-order solid–solid plastic crystal phase transition near room temperature with a relatively large latent heat (~40 kJ kg⁻¹) and an operational temperature for storing and releasing thermal energy between 42 °C (315 K) and 29 °C (302 K), very appropriate for solar thermal energy storage. In addition, the dielectric, magnetization and electron spin resonance studies reveal that this material exhibits multifunctional properties with temperature-induced reversible changes in its dielectric, conducting and magnetic behaviour associated with the phase transition. Also, the dielectric permittivity increases sharply up to 5 times when inducing the phase transition, which could be exploited to store electric energy in a capacitor. Therefore, [(CH₃)₃S]FeCl₄ is a very interesting compound with the coexistence of multifunctional properties that can be useful for both solar thermal and electric energy storage.

3.1. Introduction

Hybrid halometallate systems, which are composed of coordination metal halide anions and organic cations, have attracted great interest due to their potential applications in a wide variety of fields. For example, the low melting temperature of some hybrid halometallate salts has been exploited in the field of ionic liquids.[1–3]

Additionally, the existence of different functional properties (such as dielectric, magnetic, optical or caloric properties), associated to the reversible solid–solid phase transitions they often possess, renders them very interesting phase change materials (PCMs) for sensors and transducers, memory devices, photonics and optoelectronics, and thermal energy storage (TES), among other aplications.[4–10] In this regard, hybrid halometallates resemble the emerging family of hybrid organic– inorganic perovskites, whose functionality is also related to structural solid–solid phase transitions, in many cases of the order–disorder type.[11–13] However, differently from the framework structure presented by the perovskite compounds, the molecular nature of the hybrid halometallates, with weakly associated inorganic anions and organic cations, allows for a much larger orientational or conformational degree of freedom, which finally results in the possibility of the appearance of soft ''plastic'' crystals.[14]

This is a mesophase between the crystalline and the liquid state often found in ionic compounds with large molecular moieties, which acquire some rotational degree of freedom above a certain temperature, while their center of gravity remains fixed in the crystal lattice.[15]

Very interestingly, different hybrid halometallates with plastic crystal behaviour have been recently reported to display outstanding dielectric properties at room temperature, such as ferroelectricity and piezoelectricity.[16–19] Moreover, these compounds can be obtained by easy and low cost methods as thin-films, which is desirable for practical applications.[20]

Additionally, the relatively high latent heat associated with such solid–solid phase transitions in hybrid halometallates can be useful for TES applications.[21,22] To date, most materials used for TES applications are those with solid–liquid phase transitions, mainly because the latent heat is larger than in the case of solid–solid transitions. Nevertheless, there is an increasing interest in developing TES materials with solid–solid phase transitions because they offer a number of advantages: they avoid leaks and/or volatilization of the liquid phase, minimise volume changes providing denser and more compact systems, avoid incongruent melting, and increase thermal stability.[23–25] Specially interesting solid–solid PCMs for this type of application are the well-known polyalcohols with plastic crystal transitions, such as neopentylglycol, pentaglycerine, and pentaerythritol.[26] These polyalcohols exhibit large latent heat values; however, they have very poor thermal stability (they degrade above 353 K)[27] and they are flammable compounds, which can be unsafe for practical applications.

Therefore, it remains a challenge to find new, safe and thermally stable solid–solid PCMs with sufficient latent heat[28–30] and an adequate operational temperature.[31,32]

In this context, hybrid halometallates are arising as promising hybrid materials that can combine TES and multifunctional properties, and which are of great interest for technological applications,[33] even if these materials are very scarce.[5] This family of hybrid materials offers a

new alternative to other thermal energy storage systems based on hybrid porous materials, such as the evaporative thermal energy storage described in metal–organic frameworks (MOFs).[34]

In this work, it is reported the synthesis and characterization of a new halometallate [(CH_3)_3S]FeCl_4 with plastic crystal behaviour and interesting functional properties. As demonstrated in this chapter, this material shows a solid–solid plastic crystal phase transition with a relatively large latent heat (~40 kJ kg^{-1}) and an operational temperature that ranges between 42 and 29 °C (315 and 302 K). As discussed below, such a temperature window matches very well with the requirements for commercial solar TES applications. In addition, the multifunctional properties exhibited by this compound (with a temperature-induced reversible change in its dielectric, conducting and magnetic behaviour), render this material very interesting for both thermal energy storage and its multifunctional properties.

3.2. Experimental section

3.2.1. Materials

Commercially available analytical grade [(CH_3)_3S]Br (98% Sigma-Aldrich), FeCl_3·6H_2O (98% Sigma-Aldrich) and HCl solution (ca. 37% in H_2O ACS reagent, ACROS Organics) were used as starting materials.

3.2.2. Synthesis and basic characterization
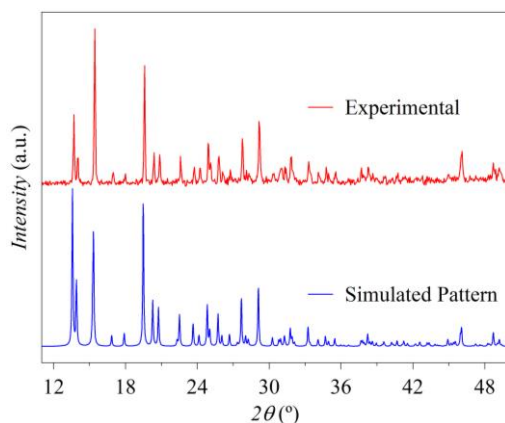
Figure 3-1. Room temperature experimental PXRD patterns for the obt **SI-**ned [(CH_3)_3S]FeCl_4 compound together with the simulated patterns based on its single crystal structure at room temperature.

Single crystals and polycrystalline powder of [(CH_3)_3S]FeCl_4 have been obtained by crystallization from a water solution with a yield of ~80%. For this purpose, stoichiometric amounts of [(CH_3)_3S]Br and FeCl_3·6H_2O were dissolved by adding 3 ml of water and 3 ml of hydrochloric acid (to provide an excess of Cl$^-$

anions). Rhombohedral yellow single crystals of [(CH_3)_3S]FeCl_4 were obtained after 3 days upon slow evaporation of the solvent at room temperature after several days and they were collected by filtration and washed several times with diethyl ether. The experimental PXRD pattern was compared with a single crystal XRD pattern simulated, confirming the purity of the formed phase (see Fig. 3-1).

3.2.3. Thermal analysis

Thermogravimetric analysis (TGA) was carried out using TGA-DTA thermal analysis SDT2960 equipment. For each experiment, approximately 27 mg of grounded single crystals were heated at a rate of 5 K min^{-1} from 300 K to 1200 K, using a corundum crucible, under a flow of dry nitrogen.

Differential scanning calorimetric (DSC) analysis was carried out using a TA-Instruments Q200, heated and cooled with a rate of 1.5 K min^{-1}, from 270 up to 350 K, under a nitrogen atmosphere.

3.2.4. Compositional analysis

Elemental analysis for C, H and S content in [(CH_3)_3S]FeCl_4 samples was carried out using a FLASHEA1112 (Thermo- Finnigan) analyzer. Calculated: C = 13.11%, H = 3.30%, S = 11.67%; found: C = 12.95%, H = 3.35%, S = 11.53%.

3.2.5. Powder X-ray diffraction

Powder X-ray diffraction (PXRD) patterns of the obtained polycrystalline samples were collected using a Siemens D-5000 diffractometer with CuKα radiation at room temperature. The experimental PXRD pattern was compared with a single crystal XRD pattern simulated using Mercury software[35] to confirm the purity of the studied single phase samples.

3.2.6. Single crystal X-ray diffraction

Single-crystal X-ray diffraction (SCXRD) experiments were carried out at temperatures well below and above the observed DSC transitions. For that purpose, single-crystal diffraction data sets of one crystal were collected at 100 K, 150 K, 200 K, 250 K, 300 K, 310 K and 320 K using a Bruker D8 VENTURE Kappa X-ray diffractometer equipped with a PHOTON III detector and using monochromatic MoKα radiation (λ = 0.71073 Å).

A suitable crystal was chosen and mounted on a MiTeGen MicroMountt using Paratones N (Hampton Research). The temperature of the crystal was changed at a rate of 200 K h^{-1} blowing the sample with a stream of nitrogen gas from an Oxford Cryosystem 800 Plus cooler. The data integration and reduction were performed using the

APEX3 v2019.1-0 (Bruker AXS, 2019) software suite. The integrations of the reflections were performed with SAINT 8.40A and the intensities collected were corrected for Lorentz and polarization effects and for absorption by semi-empirical methods on the basis of symmetry equivalent data using SADABS 2016/2 of the suite software. The structures were solved by the dual-space algorithm implemented in the SHELXT2014/5[36] program and were refined using the least squares method on SHELXL2018/3.[37]

To refine the structures, anisotropic thermal factors were used for the non-H atoms. The hydrogen atoms of the $(CH_3)_3S^+$ cations were found in the Fourier difference maps except those belonging to the lowest occupancy positions in disordered cations. The coordinates of all H atoms were freely refined in the structure at 100 K and some of them were restrained at higher temperatures during the refinement using the riding model implemented in SHELXL2018/3. Their isotropic displacement parameters were kept constrained to 1.5 times the U_{eq} values of the carbon atoms they are bonded to.

Detailed experimental crystallographic data for $[(CH_3)_3S]FeCl_4$ at T = 100, 150, 200, 250, 300, 310 and 320 K is included in Table SI-1 of the 3-SI. The crystallographic data was deposited in the Cambridge Crystallographic Data Center (CCDC) with the identifiers 2000618–2000623.

3.2.7. Electron spin resonance

Electron Spin Resonance (ESR) experiments were performed between 130 K and 400 K using a Bruker EMX spectrometer operating at 9.4 GHz (X-band), equipped with an ER 4102ST resonant cavity (TE_{102} mode). The linewidth, ΔH, was measured as the peak-to-peak distance in the first derivative of the absorption line, ΔH_{pp}.

3.2.8. Magnetic measurements

Variable-temperature magnetic susceptibility measurements were performed using a QuantumDesign MPMS SQUID magneto-meter. Different zero field-cooling/field-cooling as well as field-cooling/warming runs were performed between 4.2 K and 400 K, under different magnetic fields of H = 0.1 to 1 T.

3.2.9. Dielectric properties

The complex dielectric permittivity ($\varepsilon_r = \varepsilon_r' - i\varepsilon_r''$) of cold-press pelletized samples was measured as a function of frequency and temperature with a parallel-plate capacitor coupled to a Solartron1260A Impedance/Gain-Phase Analyzer, capable of measuring in the frequency range from 1 Hz up to 1 MHz using an amplitude of 1 V. The capacitor was mounted in a Janis SVT200T cryostat refrigerated with liquid nitrogen and with a Lakeshore 332 incorporated to control the temperature from 100 K up to

400 K. The data were collected on heating and before carrying out the measurement, the pellets were maintained at each temperature for two minutes, so as to allow them to reach thermal equilibrium. Pelletized samples, with an area of approximately 133 mm^2 and a thickness of approximately 1 mm, were prepared by cold-press to fit into the capacitor. Gold was sputtered previously on the surfaces of the pelletized samples to ensure good electrical contact. All the dielectric measurements were carried out under a nitrogen atmosphere, performing several cycles of vacuum and nitrogen gas to ensure a sample environment free of water. The conductance of the sample was determined from the real axis intercept in the Nyquist plot of the impedance data.

3.3. Results and discussion

3.3.1. Thermal characterization

DSC experiments reveal that $[(CH_3)_3S]FeCl_4$ undergoes a reversible first-order phase transition near room temperature, as shown by an endothermic peak on heating ($T_h \sim 315$ K) and an exothermic peak on cooling ($T_c \sim 302$ K) with a thermal hysteresis of 13 K (see Fig. 3-2).
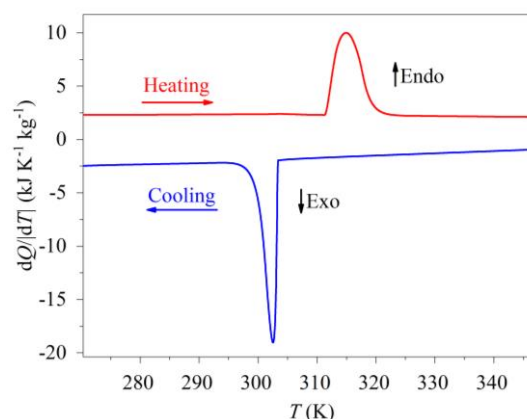
Figure 3-2. DSC results as a function of temperature (heat flow dQ/|dT| as a function of temperature, at atmospheric pressure), obtained by heating and cooling the sample at a rate of 1.5 K min^{-1}.

The values of the associated latent heat (ΔH) and entropy change (ΔS), obtained from the peak integration of the heat flow curves, are $\Delta H_h \sim 39.7$ kJ kg^{-1} and $\Delta H_c \sim 40.7$ kJ kg^{-1}, ΔS_h 126.0 J kg^{-1} K^{-1} and $\Delta S_c \sim 134.3$ kJ kg^{-1}.

Considering the configurational entropy as the main contributor to ΔS across the transition, the ratio of configurations or free energy minima thermally accessible to the system above/below the transition temperature, N, can be estimated from the equation:

$$\Delta S = R \ln(N) \tag{1}$$

It was obtained a value of $N \sim 64$, which indicates a very large variation in the number of available states in the high temperature phase, characteristic of plastic crystals.[5]

According to the TGA results (Fig. 3-3), the new [(CH$_3$)$_3$S]FeCl$_4$ compound shows a large thermal stability with a decomposition temperature of T_{dec} ~ 550 K, offering a thermal stability of between 50 and 20 K larger than most of the reported hybrid halometallates (see Table 3-1).
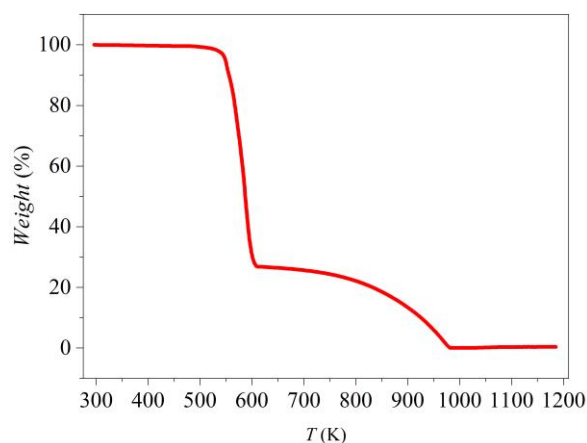
Figure 3-3. TGA decomposition curve for the [(CH$_3$)$_3$S][FeCl$_4$] compound.

Above this temperature, it decomposes in two steps: there is a first weight loss (~70% at T ~ 550 K), which corresponds to the loss of the [(CH$_3$)$_3$S]$^+$ cations and one Cl$^-$ anion; and a second weight loss (~30% at T ~ 773 K)

related to the complete volatilization of the remaining inorganic FeCl$_3$ residue.

In view of such phase transition and in order to evaluate the potential of this compound for TES applications, the requirements and the commercial needs for solar TES materials were firstly analysed. In this context, the ideal thermal storage material should fulfill several criteria related to its thermal and physico-chemical properties, namely: phase transition temperature in the desired operating range and thermal hysteresis (T_h - T_c) matching the desired charging and discharging temperatures, large specific heat and phase transition latent heat, large density to increase the thermal storage per unit of volume, large thermal conductivity, small volume change at the phase transition, low vapour pressure and chemical and thermal stability, among others.[23,44,45]

As for the commercial needs for TES, PCMs for household applications (such as indoor comfort temperature or hot water supply) are required to store thermal energy at operational temperatures (charging temperatures) of around 30–60 °C (303–333 K).[32] These temperatures are easily achievable under sunlight illumination without needing the use of solar collectors. Besides, the temperature for releasing the stored thermal energy (discharging temperature) should be around two degrees above the desired comfort temperature (normally around 20 °C or 293 K).[32]

Table 3-1. Selected thermal and physico-chemical parameters of interest for TES applications of different hybrid halometallate compounds and polyalcohols: transition temperature (T_h) and thermal hysteresis (T_h - T_c), phase transition latent heat per unit of mass and per unit of volume (ΔH_h), density of the low temperature polymorphs (ρ) and decomposition temperature (T_{dec}). a Flash points of pentaerythriol and pentaglycerine. Date: September 2020.

Hybrid halometallate compounds	T_h (K)	T_h-T_c (K)	ΔH_h (kJ kg^{-1})	ΔH_h (J cm^{-3})	ρ (g cm^{-3})	T_{dec} (K)	Ref.
1. [(CH$_3$)$_3$S]FeCl$_4$	315	13	39.7	61.9	1.56	550	This work
2. [(CH$_3$)$_4$N]FeCl$_4$	385	5	21.9	32.4	1.48	-	38
3. [(CH$_3$)$_3$(CH$_2$Cl)N]FeCl$_4$	329	5	44.0	80.2	1.62	530	5
4. [(CH$_3$)$_3$S]$_2$MnBr$_4$	312	32	23.6	48.8	2.07	519	39
5. [(CH$_3$)$_3$S]$_2$CdBr$_4$	304	32	20.0	45.0	2.25	506	39
6. [(CH$_3$)$_3$S]$_2$ZnBr$_4$	310	37	20.1	42.8	2.13	500	39
7. [Fe(C$_5$(CH$_3$)$_4$H)$_2$]FeCl$_4$	298	8	16.1	24.0	1.49	-	4
8. [Fe(C$_5$(CH$_3$)$_4$H)$_2$]GaCl$_4$	301	43	24.4	37.3	1.53	-	4
9. [Fe(C$_5$(CH$_3$)$_4$H)$_2$]B(CN)$_4$	312	10	34.1	42.3	1.24	-	4
10. [Fe(C$_5$(CH$_3$)$_4$H)$_2$]C(CN)$_3$	343	18	68	87.7	1.29	525	4
11. [Fe(C$_5$(CH$_3$)$_4$H)$_2$](SO$_2$F)$_2$N	355	21	25.5	41.8	1.64	523	4
12. [C$_5$H$_9$N$_2$]FeCl$_4$	357	22	97.7	159.2	1.63	624	40
13. [C$_5$H$_{14}$NO]FeCl$_4$	282	26	38.8	38.4	0.99	520	41
14. Neopenthylglycol (NPG)	317	15	130	143.0	1.1	353	42
15. Pentaerythritol (PE)	463	27	301	421.4	1.4	473^a	43
16. Pentaglycerine (PG)	361	25	153	186.7	1.22	423^a	43
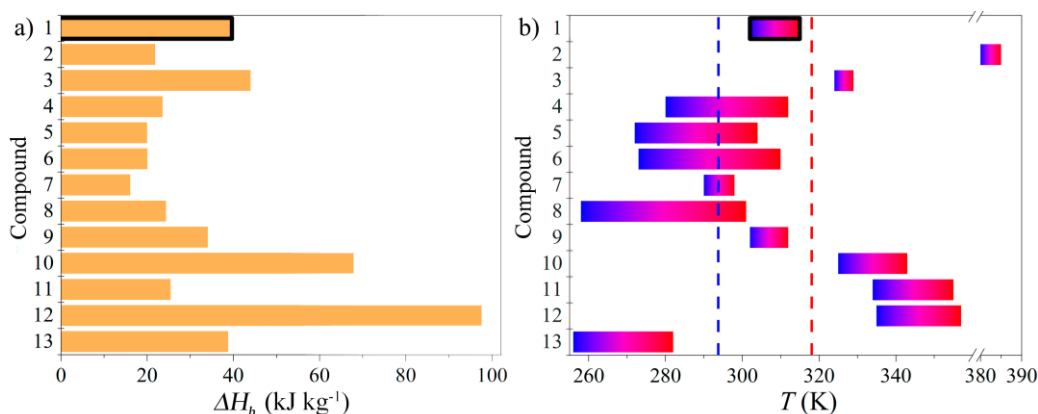
Figure 3-4. (a) Comparison of latent heat (ΔH) measured on heating for hybrid halometallate compounds. Note: numbers indicate the corresponding hybrid halometallate compounds from Table 1. (b) Comparison of operational temperature for the same compounds. Note: the blue end of the bars indicates the discharging temperature and the red end of the bars indicate the charging temperature. The compound $[(CH_3)_3S]FeCl_4$ reported in this work is #1 and it is enclosed within a black frame. Dashed lines are guidelines indicating the average discharging (blue) and charging (red) temperatures for solar TES domestic applications.[32]

The thermal and physico-chemical parameters of $[(CH_3)_3S]FeCl_4$ that are of interest for TES applications are summarized in Table 3-1, where our material is compared with other outstanding hybrid halometallate compounds and poly- alcohols (one of the first generations of TES materials with solid–solid phase transitions) for reference purposes. In general, hybrid hallometalates display a smaller latent heat than most polyalcohols. On the other hand, the hybrid materials are more thermally stable and are not flammable compounds, which is very important for practical applications.

As it can be observed in Table 3-1 and Fig. 3-3a, the latent heat per unit of mass of $[(CH_3)_3S]FeCl_4$ (39.7 kJ kg^{-1}) is larger than most of these hybrids, even if the specific heat capacity is expected to be similar, 1.0–1.5 kJ kg^{-1} °C^{-1}.[5]

Most interestingly, the operational temperature of this com- pound for storing thermal energy (charging temperature) is ~315 K, and for releasing this energy (discharging temperature) is ~302 K, which is very close to the operational temperature requirements for solar TES applications, especially for domestic use,[32] as indicated above (see Fig. 3-3b). Therefore, the relatively large latent heat and the enhanced thermal stability and operational temperature in comparison with most reported hybrid halometallates bring this material closer to the commercial requirements for solar thermal energy storage applications.

### 3.3.2. Crystal structures by single-crystal X-ray diffraction

In order to understand the origin of the observed phase transition, single-crystal X-ray diffraction experiments were performed at different temperatures well below and above the transition temperature T_t. The SCXRD results reveal a structural phase transition at T_t from a rather ordered low temperature LT-polymorph present at $T<T_t$ into a highly disordered high temperature HT-polymorph present at $T>T_t$. Furthermore, this solid-to-solid phase

transition is completely reversible, even if the crystals get twinned on the phase transition on both heating and cooling.
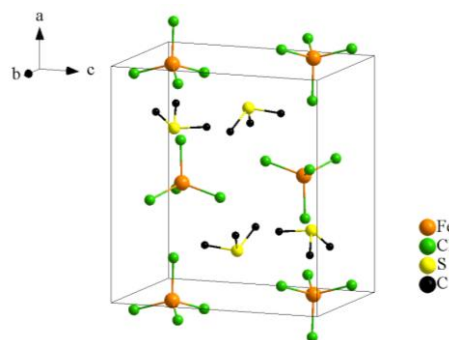
Figure 3-5. Crystal structure of the LT-polymorph of $[(CH_3)_3S]FeCl_4$.

The LT-polymorph is orthorhombic, space group *Pnma* (see more details in Table SI-1 of the supplementary info of this chapter, 3SI and Fig. 3-5).
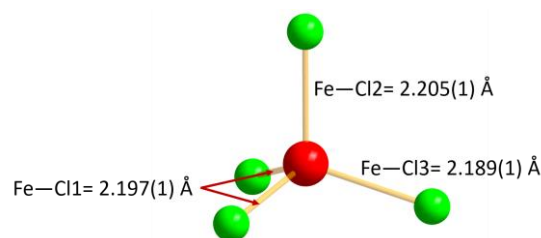
Figure 3-6. Detail of the crystal structure of the $[(CH_3)_3S]FeCl_4$ compound showing the three different Fe-Cl distances present in the [FeCl4]$^-$ anions at 100K.

Concerning the molecular arrangement within the crystal structure, the compound displays a NiAs-type structure where the [FeCl4]$^-$ anions are surrounded by six

[(CH₃)₃S]⁺ cations, forming an octahedral environment, while the $[(CH_3)_3S]^+$ cations themselves are surrounded by six $[FeCl_4]^-$ in a trigonal prismatic environment.
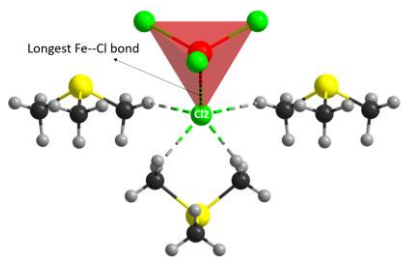
Figure 3-7. Detail of the crystal structure of the $[(CH_3)_3S]FeCl_4$ compound at 100K showing the interactions between one Cl-atom of $[FeCl_4]^-$ with four H-atoms of methyl groups of three $[(CH_3)_3S]^+$ cations.

The asymmetric unit of the LT-polymorph consists of one half of $[(CH_3)_3S]^+$ and one half of $[FeCl4]^-$, as both moieties are placed over a mirror symmetry plane. In the case of this anion, the Fe^{3+} is in a slightly distorted tetrahedral environment as three different Fe–Cl distances are observed (see Fig. 3-6). It is also worth highlighting that at 100 K, both the cationic and anionic species are ordered.
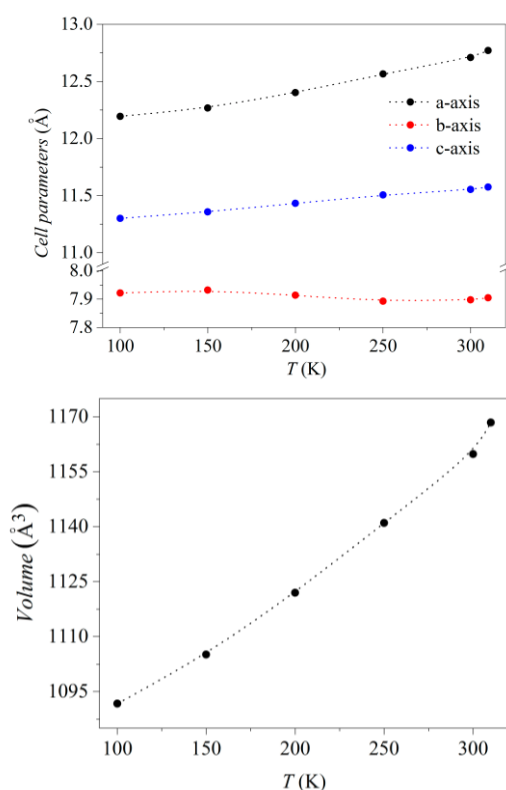

Figure 3-8. Top: Thermal evolution of the cell parameters of the LT-polymorph of $[(CH_3)_3S]FeCl_4$. **Bottom:** Thermal evolution of the volume of the LT-polymorph of $[(CH_3)_3S]FeCl_4$.

On the other hand, the interactions between the anionic–cationic components are electrostatic and weak (see Fig. 3-5).

In addition, there are interactions between Cl-atoms of the $[FeCl_4]^-$ entities and H-atoms of the methyl groups of $[(CH_3)_3S]^+$ (see Fig. 3-6 and Table SI-2 of the 3-SI). At 100 K these interactions occur in the *bc*-plane and involve in particular one of the Cl-atoms (the one with largest Fe–Cl distance) and four methyl groups of three $(CH_3)_3S^+$ (see Fig. 3-7).

As for the thermal evolution of the crystal structure of the LT-polymorph from T = 100 K to 310 K, our studies confirm that the compound preserves the *Pnma* symmetry up to T_t.
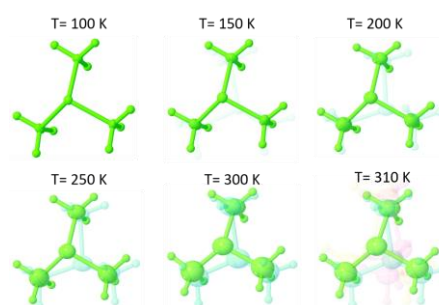
Figure 3-9. Detail of the crystal structure of $[(CH_3)_3S]FeCl_4$ showing the disorder of the $[(CH_3)_3S]^+$ cations at different temperatures between 100, 150, 200, 250, 300 and 310K (from left top to right bottom). The ellipsoid shows a probability of 30%. Hydrogen atoms shown as spheres of fixed radius. Refined atomic population parameters are used for transparency level (%), see Table SI-3 for numerical values.

The unit cell shows some anisotropy in the expansion: the b axis remains almost constant while the a and c axes elongate with temperature, even if the unit cell volume exhibits the expected thermal expansion upon heating (see Fig. 3-8).
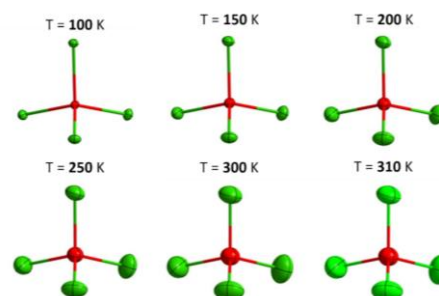
Figure 3-10. Detail of the crystal structure of $[FeCl4]^-$ tetrahedral at different temperatures between 100, 150, 200, 250, 300 and 310 K (from left top to right bottom). The ellipsoid shows a probability of 30%.

Another interesting feature is that the $[(CH_3)_3S]^+$ cations start exhibiting some rotational disorder as soon as the temperature increases above 100 K, so that their

coordinates can be modelled and refined in 2, or even 4 disordered orientations at 310 K (see Fig. 3-9, 3-10 and Table SI-3 of the 3-SI).

The increasing number of $[(CH_3)_3S]^+$ orientations extends and complicates the hydrogen bonding interaction between the cationic and anion species (Table SI-2 of 3-SI) making them more spherically (isotropically) distributed in space, instead of being only restricted to the bc-plane.

Above T_t, the X-ray diffraction data show a twinning, exhibit strong diffuse scattering (see Fig. 3-11) and a drastic reduction in Bragg reflection intensity (~1.35 Å maximum resolution observed), as it is characteristic for plastic crystals composed of severely disorder molecular entities.[46] This precluded the refinement of the HT-structure, although the data could be indexed to a cubic symmetry with a primitive cell, with cell parameter a = 6.662(1) Å (Table SI-1 in the 3-SI). The formation of a high-temperature highly disordered phase of cubic symmetry is also typical for plastic crystals.[47]
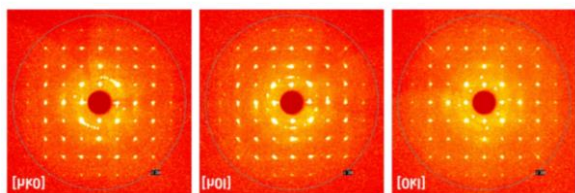
Figure 3-11. Precession images generated from single-crystal X-ray diffraction data of the HT-polymorph obtained along the main axis.

The orientational degree of freedom of the $[(CH_3)_3S]^+$ and the $[FeCl_4]^-$ in the HT-polymorph is also supported by the weakly associated anion–cation components and the high latent heat associated to the phase transition, as discussed before.

3.3.3. Magnetic properties: magnetization results and ESR

The temperature dependence of the magnetic susceptibility of $[(CH_3)_3S]FeCl_4$ was measured in a wide temperature range across the structural phase transition (Fig. 3-12a). The inverse susceptibility versus temperature fits nicely to a Curie law in the temperature range $4.2 < T$ (K) < 300 (Fig. 3-12b), which discards any type of magnetic ordering. The magnetic moment in the LT-polymorph is $\mu \sim 5.8$ μ_B/Fe, in good agreement with a spin-only value expected for Fe^{3+}.

In addition, the magnetic susceptibility shows hysteretic behaviour in the temperature range 300–320 K, $i.e.$ across the first order structural phase transition (see the inset to Fig. 3-12a). On the other hand, the magnetic susceptibility of the HT-polymorph deviates continuously from the Curie law indicating a continuous decrease of the magnetic moment in the plastic crystal phase. The

reversible behaviour of the magnetic susceptibility and the TGA analysis discard the evaporation of any of the components of $[(CH_3)_3S]FeCl_4$ in this temperature range. Thus, the continuous change in the magnetic moment must reflect a variation in the static Fe–Cl (crystal-field) distances.

To access the dynamic magnetic structure of the system in the LT- and HT-polymorphs, the Electron Spin Resonance (ESR) spectra was collected from 130 K to 400 K.
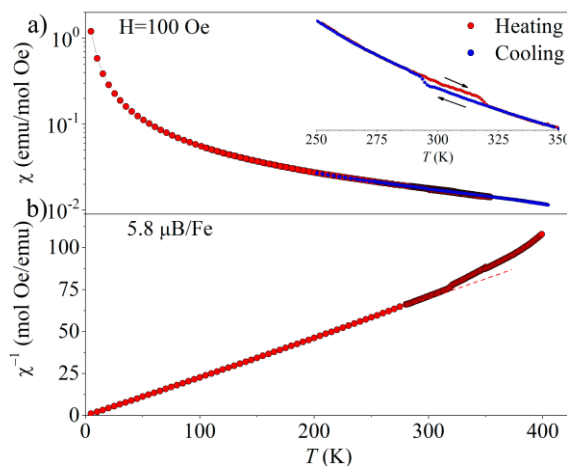
Figure 3-12. (a) Temperature dependence of the magnetic susceptibility measured at $H \sim 100$ Oe. The inset shows an enlargement around the structural phase transition. (b) Inverse susceptibility versus temperature curve and its fitting to a Curie law (dash line).

The low temperature spectrum consists of a single Lorentzian line coming from the resonance of Fe^{3+} (d^5), centered around $H_r \sim 3280$ G ($g \sim 2.07$), and with a linewidth which decreases continuously, from $\Delta H_{pp} \sim 2100$ G at 150 K, to $\Delta H_{pp} \sim 1550$ G at 300 K, right before T_t (see Fig. 3-13).
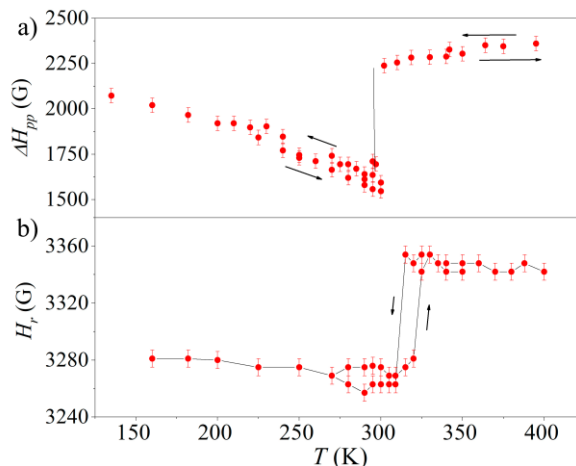
Figure 3-13. (a) Temperature dependence of the ESR linewidth. (b) Resonance field across the structural phase transition.

Given the large Fe–Fe distances (~6.5–7.3 Å) in the crystal, dipolar interactions must be the source of line-broadening in this compound with negligible narrowing from direct exchange interaction ($J \sim 0$ from the magnetic susceptibility data).

In this case $\Delta H_{pp} \sim (0.5\pi\mu_{eff}\rho)$, where the effective μ_{eff} is the effective magnetic moment (5.8 μ_B) and ρ is the spin density (3.39 x 10^{21} Fe per cm^3). This calculation predicts a value of $\Delta H_{pp} \sim 2860$ G, about 35% larger than the value of ΔH_{pp} at the lowest temperature measured in this work. Moreover, there is a marked and continuous decrease of ΔH_{pp} with temperature.

There are many intrinsic (dipolar interaction, etc.) and extrinsic (vacancies or imperfections, etc.) factors which add random perturbations to the local magnetic field sensed by each Fe^{3+} ion, broadening the experimental ESR signal. However, if the resonating spins can move at a faster rate (ω_r) than the amplitude of the perturbations (ω_p), this averages out the effect of the inhomogeneities over the local field, narrowing the ESR absorption line, according to:

$$\Delta\omega = \omega_{dip}^2 \big/ \omega_r \qquad (2)$$

This is the mechanism responsible for line-narrowing in liquids (due to rapid spin-probe diffusion),[48] in doped organic/inorganic semiconductors due to fast polaron diffusion,[49] and also in plastic crystals, through averaging out of the anisotropic spin environment through fast rotational movement.[38]

Moreover, fast rotational movement produces a characteristic Lorentzian lineshape, consistent with the experimental observation (pure dipolar interaction between like spins in dense solids results in absorption lines with a characteristic Gaussian shape).[50]

Therefore, the continuously decreasing linewidth observed in the LT-phase is consistent with the motional narrowing from the thermally activated rotation of $[(CH_3)_3S]^+$ observed by X-ray diffraction.[38]

On the other hand, both ΔH_{pp} and H_r show a discontinuous increase at T_t, and remain constant above this temperature in the HT-polymorph, see Fig. 13. In this case, the almost constant ΔH_{pp}, ~20% smaller than the calculation, suggests that the mechanism responsible for line-narrowing observed in the LT-polymorph is not operative in the HT-polymorph. Although this result is far from being completely understood, the strong disorder observed in XRD above T_t, as well as the continuous departure observed from the Curie law suggest a diffusive movement of the ionic environment.

3.3.4. Dielectric properties

To probe the hypothesis of the ionic dynamics, the dielectric properties were measured across the structural transition. Fig. 14 shows the temperature dependence of the real part of the complex dielectric permittivity (the so-

called dielectric constant or real part of the relative permittivity, ε_r') in the temperature range 300–350 K. As it can be seen, a sharp dielectric transition occurs at $T \sim$ 318 K, transforming the ε_r' (LT-polymorph) ~ 10 into ε_r' (HT-polymorph) ~ 45–50. Therefore, the dielectric constant of the material increases up to 5 times when heating above the phase transition. It should be noted that the relative permittivity is directly related to that of the capacity of a material to store electrical energy into a parallel plate capacitor. Accordingly, this sharp phase transition involves the increase of up to five times of the amount of electric energy that can be stored into a capacitor built with this material at temperatures above T_t.

On the other hand, and in view of the shape of the ε_r' versus T curve, which reminds of that shown by antiferroelectric materials, and the crystal structures of both polymorphs, the observed dielectric response can be rationalized as following: it is related to the change from an antiferrodistortive arrangement in the LT-polymorph to a paraelectric state in the HT-polymorph. In this context, a careful inspection of the low temperature crystal structure reveals the existence of two cooperative anti- ferrodistortive distortions that could be responsible for the subsequent structural and dielectric transition. An off-center shift of the Fe^{3+} cations in the $[FeCl_4]^-$ anions in the LT-polymorph, which renders these tetrahedral ions polar.
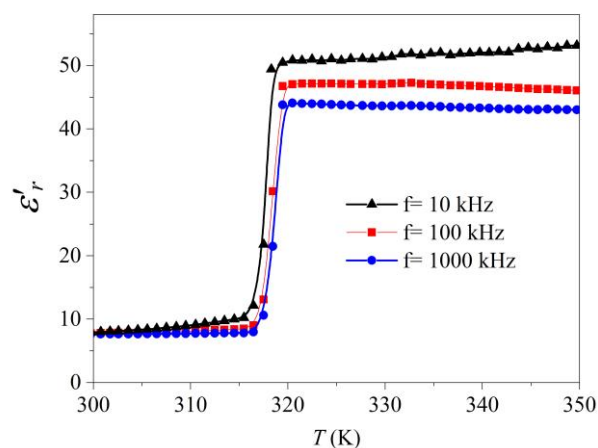
Figure 3-14. Temperature dependence of the dielectric constant (ε_r'), measured at different frequencies (10, 100 and 1000 kHz) for $[(CH_3)_3S]FeCl_4$.

Considering that those polar $[FeCl_4]^-$ anions and polar $[(CH_3)_3S]^+$ cations are antiparallelly arranged with respect to each other in the crystal, the resulting net polarization nulled and the LT-polymorph displays an antiparallel arrangement. Meanwhile, in the disordered HT-polymorph, the moments associated to the moving/rotating ionic species average out, giving rise to a paraelectric state.
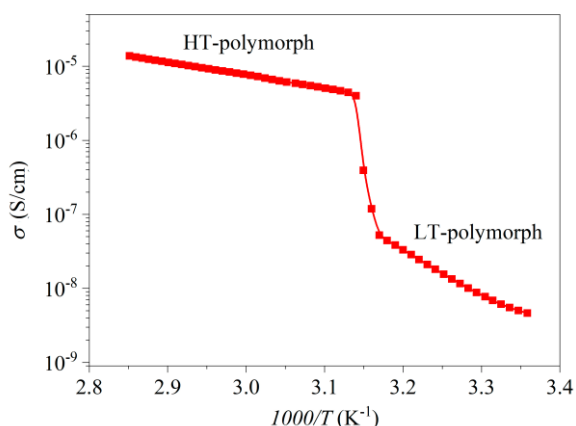
Figure 3-15. Temperature dependence of conductivity of [(CH$_3$)$_3$S]FeCl$_4$.

Additionally, the solid-state ionic conductivity was studied, which is closely related to the microscopic rotational and translational motions of the ionic species (see Fig. 3-15). Interestingly, the conductivity of the LT-phase experiences a large variation at T_t, increasing approximately by two orders of magnitude. It is also worth noting that the conductivity of both the LT- and HT-phases follow an Arrhenius law (see Fig. 3-15). From the linear relationship of logσ versus 1000/T data, the activation energies could be calculated as E_a (LT-polymorph) ~ 0.51 eV and E_a (HT-polymorph) ~ 0.15eV.

Within the context discussed before, the lower conductivity of the LT-polymorph is attributed to the restricted ionic movement in an ordered crystalline phase. In contrast, the relatively high conductivity of the HT-polymorph seems to indicate a substantial degree of self-diffusion of the ionic species within this plastic phase, as often observed in ionic plastic crystals.[51]

Given the persistence of (low intensity) X-ray diffraction signal, the HT-phase could be a mesophase with the coexis- tence of crystalline and glassy regions and [(CH$_3$)$_3$S]$^+$ cations and [FeCl$_4$]$^-$ anions could possess an orientational degree of freedom in both of them. In addition, the glassy region seems to show certain translational motions of the ionic species, where the dipolar interaction between the ionic species is temperature independent.

3.4. Conclusions

In this work, it is reported a novel plastic crystal [(CH$_3$)$_3$S]FeCl$_4$, which exhibits several interesting functional properties and can also be interesting for multi-energy storage (both thermal energy storage and electric energy storage). In fact, solar energy can be converted and stored as thermal energy in this material but also induces a notable increase in the amount of electric energy that can be stored on a capacitor made with this material.

As explained in detail, this compound undergoes a reversible, first-order phase transition near room temperature (T_t ~ 315 K), with a rather large thermal hysteresis of 13 K and a notable latent heat (ΔH ~ 39.7 kJ kg^{-1}) around the phase transition temperature, which render this material very interesting for solar thermal energy storage with an operational temperature for storing and releasing thermal energy between 42 ºC (315 K) and 29 ºC (302 K), respectively.

The characterization of the solid–solid reversible phase transitions reveals a reversible transformation of a LT-ordered orthorhombic (S.G.: *Pnma*) polymorph into a dynamically highly disordered cubic plastic phase, whose detailed characteristics and evolution with temperature were investigated by SCXRD, ESR, magnetic and dielectric measurements.

Very remarkably, this PCM compound exhibits temperature-induced reversible changes in its magnetic, dielectric, and conducting behaviour associated to such phase transition, namely: (i) a hysteretic magnetic behaviour across the transi- tion with decrease of the magnetic moment in the dynamically disordered plastic phase; (ii) a sharp dielectric transition from an antiferrodistortive arrangement in the LT-polymorph to a paraelectric state at the HT-polymorph, and (iii) a sharp increase of the ionic conductivity in the plastic phase probably related to a substantial degree of self-diffusion of the ionic species within that phase.

In the specific case of its dielectric constant, it was found that it increases up to five times when heating the material above the phase transition, giving rise to a fivefold increase in the capacity of the material to store electric energy when in the form of a capacitor. Therefore, the provided solar energy can not only be stored as latent heat, but can also induce a fivefold increase in electrical energy that can be stored in a capacitor device made with this material.

3.5. Notes

The work showed and discussed in this chapter has been published in the following article:

J. Salgado-Beceiro, J. M. Bermúdez-García, A. L. Llamas-Saiz, S. Castro-García, M. A. Señarís-Rodríguez, F. Rivadulla and M. Sánchez-Andújar, *J. Mater. Chem. C*, 2020, 8, 13686–13694.

3.6. References

1   J. Estager, J. D. Holbrey and M. Swadźba-Kwaśny, *Chem. Soc. Rev.*, 2014, 43, 847–886.

2   R. Kore, P. Berton, S. P. Kelley, P. Aduri, S. S. Katti and R. D. Rogers, *ACS Catal.*, 2017, 7, 7014–7028.

3   A. W. Taylor, S. Men, C. J. Clarke and P. Licence, *RSC Adv.*, 2013, 3, 9436–9445.

4   T. Mochida, M. Ishida, T. Tominaga, K. Takahashi, T. Sakurai and H. Ohta, *Phys. Chem. Chem. Phys.*, 2018, 20, 3019–3028.

5   D. Li, X.-M. Zhao, H.-X. Zhao, L.-S. Long and L.-S. Zheng, *Inorg. Chem.*, 2019, 58, 655–662.

6   K. Y. Chan, B. Jia, H. Lin, N. Hameed, J. H. Lee and K. T. Lau, *Compos. Struct.*, 2018, 188, 126–142.

7   X. Zhang, X. Wang and D. Wu, *Energy*, 2016, 111, 498–512.

8   S. Jang, E. Hwang, Y. Lee, S. Lee and J. H. Cho, *Nano Lett.*, 2015, 15, 2542–2547.

9   X. Huang, G. Alva, Y. Jia and G. Fang, *Renew. Sustain. Energy Rev.*, 2017, 72, 128–145.

10 X. Geng, W. Li, Y. Wang, J. Lu, J. Wang, N. Wang, J. Li and X. Zhang, *Appl. Energy*, 2018, 217, 281–294.

11 K. T. Butler, A. Walsh, A. K. Cheetham and G. Kieslich, *Chem. Sci.*, 2016, 7, 6316–6324.

12 H. Y. Ye, J. Z. Ge, Y. Y. Tang, P. F. Li, Y. Zhang, Y. M. You and R. G. Xiong, *J. Am. Chem. Soc.*, 2016, 138, 13175–13178.

13 J. Even, M. Carignano and C. Katan, *Nanoscale*, 2016, 8, 6222–6236.

14 J. Timmermans, *J. Phys. Chem. Solids*, 1961, 18, 1–8.

15 L. A. K. Staveley, *Annu. Rev. Phys. Chem.*, 1962, 13, 351–368.

16 M. Ben Bechir, K. Karoui, M. Tabellout, K. Guidara and A. Ben Rhaiem, *J. Alloys Compd.*, 2014, 588, 551–557.

17 J. Harada, T. Shimojo, H. Oyamaguchi, H. Hasegawa, Y. Takahashi, K. Satomi, Y. Suzuki, J. Kawamata and T. Inabe, *Nat. Chem.*, 2016, 8, 946–952.

18 J. Harada, N. Yoneyama, S. Yokokura, Y. Takahashi, A. Miura, N. Kitamura and T. Inabe, *J. Am. Chem. Soc.*, 2018, 140, 346–354.

19 J. Harada, Y. Kawamura, Y. Takahashi, Y. Uemura, T. Hasegawa, H. Taniguchi and K. Maruyama, *J. Am. Chem. Soc.*, 2019, 141, 9349–9357.

20 Z.-X. Zhang, T. Zhang, P.-P. Shi, W.-Y. Zhang, Q. Ye and D.-W. Fu, *Inorg. Chem. Front.*, 2020, 7, 1239–1249.

21 A. Sharma, V. V. Tyagi, C. R. Chen and D. Buddhi, *Renew. Sustain. Energy Rev.*, 2009, 13, 318–345.

22 K. Pielichowska and K. Pielichowski, *Prog. Mater. Sci.*, 2014, 65, 67–123.

23 A. Fallahi, G. Guldentops, M. Tao, S. Granados-Focil and S. Van Dessel, *Appl. Therm. Eng.*, 2017, 127, 1427–1441.

24 S. Sundararajan, A. B. Samui and P. S. Kulkarni, *J. Mater. Chem. A*, 2017, 5, 18379–18396.

25 G. Alva, L. Liu, X. Huang and G. Fang, *Renew. Sustain. Energy Rev.*, 2017, 68, 693–706.

26 D. K. Benson, R. W. Burrows and J. D. Webb, *Sol. Energy Mater.*, 1986, 13, 133–152.

27 M. M. Umair, Y. Zhang, K. Iqbal, S. Zhang and B. Tang, *Appl. Energy*, 2019, 235, 846–873.

28 C. Alkan, E. Günther, S. Hiebler, Ö. F. Ensari and D. Kahraman, *Sol. Energy*, 2012, 86, 1761–1769.

29 Y. Zhang, L. Wang, B. Tang, R. Lu and S. Zhang, *Appl. Energy*, 2016, 184, 241–246.

30 X. Du, H. Wang, Y. Wu, Z. Du and X. Cheng, *J. Appl. Polym. Sci.*, 2017, 134, 1–8.

31 L. Navarro, A. de Gracia, S. Colclough, M. Browne, S. J. McCormack, P. Griffiths and L. F. Cabeza, *Renew. Energy*, 2016, 88, 526–547.

32 F. Souayfane, F. Fardoun and P.-H. Biwole, *Energy Build.*, 2016, 129, 396–431.

33 Y. Huang, M. Zhu, Y. Huang, Z. Pei, H. Li, Z. Wang, Q. Xue and C. Zhi, *Adv. Mater.*, 2016, 28, 8344–8364.

34 A. Elsayed, E. Elsayed, A.-D. Raya, S. Mahmoud, A. Elshaer and W. Kaialy, *Appl. Energy*, 2017, 186, 509–519.

35 C. F. Macrae, I. Sovago, S. J. Cottrell, P. T. A. Galek, P. McCabe, E. Pidcock, M. Platings, G. P. Shields, J. S. Stevens, M. Towler and P. A. Wood, *J. Appl. Crystallogr.*, 2020, 53, 226–235.

36 G. M. Sheldrick and IUCr, *Acta Crystallogr. Sect. A Found. Adv.*, 2015, 71, 3–8.

37 G. M. Sheldrick, *Acta Crystallogr. Sect. C Struct. Chem.*, 2015, 71, 3–8.

38 J. Salgado-Beceiro, S. Castro-García, M. Sánchez-Andújar and F. Rivadulla, *J. Phys. Chem. C*, , DOI:10.1021/acs.jpcc.8b09367.

39 X. G. Chen, Y. Z. Zhang, D. S. Sun, J. X. Gao, X. N. Hua and W. Q. Liao, *Dalt. Trans.*, 2019, 48, 11292–11297.

40 A. García-Saiz, P. Migowski, O. Vallcorba, J. Junquera, J. A. Blanco, J. A. González, M. T. Fernández-Díaz, J. Rius, J. Dupont, J. Rodríguez Fernández and I. De Pedro, *Chem. - A Eur. J.*, 2014, 20, 72–76.

41 I. De Pedro, A. García-Saiz, J. González, I. Ruiz De Larramendi, T. Rojo, C. A. M. Afonso, S. P. Simeonov, J. C. Waerenborgh, J. A. Blanco, B. Ramajo and J. R. Fernández, *Phys. Chem. Chem. Phys.*, 2013, 15, 12724–12733.

42 J. Font, J. Muntasell, J. Navarro and J. L. L.

Tamarit, *Sol. energy Mater.*, 1987, 15, 403–412.

43 M. Barrio, J. Font, J. Muntasell, J. Navarro and J. L. Tamarit, *Sol. energy Mater.*, 1988, 18, 109–115.

44 L. Klimeš, P. Charvát, M. Mastani Joybari, M. Zálešák, F. Haghighat, K. Panchabikesan, M. El Mankibi and Y. Yuan, *Appl. Energy*, 2020, 263, 114572.

45 E. Moreles, G. Huelsz and G. Barrios, *Build. Simul.*, 2018, 11, 519–531.

46 P. Gerlach and W. Prandl, *Acta Crystallogr. Sect. A Found. Crystallogr.*, 1988, 44, 128–136.

47 R. M. Lynden-Bell and K. H. Michel, *Rev. Mod. Phys.*, 1994, 66, 721–762.

48 J. E. (John E. Wertz and J. R. Bolton, *Electron spin resonance : elementary theory and practical applications*, McGraw-Hill, New York, 1972.

49 H. Matsui, T. Hasegawa, Y. Tokura, M. Hiraoka and T. Yamada, *Phys. Rev. Lett.*, 2008, 100, 126601.

50 C. P. Poole, *Electron spin resonance : a comprehensive treatise on experimental techniques*, Dover Publications, New York, 1983.

51 J. M. Pringle, P. C. Howlett, D. R. MacFarlane and M. Forsyth, *J. Mater. Chem.*, 2010, 20, 2056.

Chapter 3

Supplementary info

Table SI-1. Crystal data and structure refinement for $[(CH_3)_3S]FeCl_4$.

Empirical formula	$C_3H_9S\ FeCl_4$						
Wavelength (Å)	0.71073						
Crystal size (mm³)	0.170 x 0.100 x 0.056						
Formula weight	274.81						
F(000)	548						
							Proposed SG
Temperature (K)	100	150	200	250	300	310	320
Crystal system	Orthorhombic	Orthorhombic	Orthorhombic	Orthorhombic	Orthorhombic	Orthorhombic	Cubic?
Space group	*Pnma*	*Pnma*	*Pnma*	*Pnma*	*Pnma*	*Pnma*	*Pm-3m*?
Unit cell dimensions (Å)	a = 12.1950(7)	a = 12.2667(8)	a = 12.4012(4)	a = 12.5644(5)	a = 12.707(4)	a = 12.7698(9)	a = 6.6626(13)
	b = 7.9217(4)	b = 7.9320(5)	b = 7.9136(2)	b = 7.8927(3)	b = 7.900(2)	b = 7.9044(5)	
	c = 11.3013(6)	c = 11.3580(7)	c = 11.4326(4)	c = 11.5059(4)	c = 11.551(4)	c = 11.5756(8)	
Volume (Å³)	1091.71(10)	1105.13(12)	1121.97(6)	1141.01(7)	1159.6(6)	1168.41(14)	295.75(17)
Z	4	4	4	4	4	4	1
Density calculated (Mg/m³)	1.672	1.652	1.627	1.600	1.574	1.562	-
Absorption coefficient (mm⁻¹)	2.482	2.452	2.415	2.375	2.337	2.319	2.290
Tmin, Tmax	0.72, 0.87	0.65, 0.88	0.74, 0.88	0.74, 0.88	0.74, 0.88	0.72, 0.88	0.61, 0.82
Theta range for data collection (°)	2.46 - 36.37	2.44 - 33.16	2.42 - 33.13	2.40 - 29.57	2.38 - 27.13	2.38 - 26.72	3.06 – 15.15
Index ranges	-20<=h<=20 -13<=k<=13 -18<=l<=18	-17<=h<=18 -12<=k<=12 -17<=l<=17	-17<=h<=19 -12<=k<=12 -17<=l<=17	-16<=h<=17 -10<=k<=10 -15<=l<=15	-15<=h<=16 -10<=k<=10 -14<=l<=14	-15<=h<=16 -10<=k<=9 -14<=l<=14	-4<=h<=4 -4<=k<=4 -4<=l<=4
Measured reflections	65618	16182	17487	13914	11340	11256	2763
Independent reflections	2802 [R(int)=0.0488]	2241 [R(int)=0.0417]	2260 [R(int)=0.0369]	1702 [R(int)=0.0390]	1372 [R(int)=0.0365]	1324 [R(int)=0.0332]	24 [R(int)=0.0588]
Indep. Reflections [I>(I)]	2420	1726	1715	1194	889	844	24
Completeness (%)	99.8	99.9	99.8	99.8	99.9	99.9	100
Refinement method	Full-matrix least-squares on F²						-
Data / restraints / parameters	2802 / 0 / 63	2241 / 94 / 83	2260 / 94 / 83	1702 / 94 / 83	1372 / 94 / 83	1324 / 219 / 121	-
Goodness-of-fit on F²	1.102	1.057	1.031	1.022	1.030	1.050	-
Final R indices [I>2sigma(I)]	R1 = 0.0288 wR2 = 0.0603	R1 = 0.0345 wR2 = 0.0601	R1 = 0.0343 wR2 = 0.0719	R1 = 0.0401 wR2 = 0.0938	R1 = 0.0484 wR2 = 0.1254	R1 = 0.0378 wR2 = 0.0933	-
R indices (all data)	R1 = 0.0377 wR2 = 0.0652	R1 = 0.0542 wR2 = 0.0680	R1 = 0.0514 wR2 = 0.0827	R1 = 0.0602 wR2 = 0.1090	R1 = 0.0764 wR2 = 0.1493	R1 = 0.0621 wR2 = 0.1113	-
Largest diff. peak and hole (e·Å⁻³)	0.628 and -0.657	0.652 and -0.469	0.439 and -0.410	0.560 and -0.374	0.522 and -0.262	0.230 and -0.215	-

Table SI-2. Interactions between Cl-atoms of [FeCl$_4$]$^-$ with the H-atoms of methyl group of [(CH$_3$)$_3$S]$^+$ cations at different temperatures (distances in Å, °). Atoms labelled as ^a, ^b or ^c according to different disordered positions for the cation.

	D-H	H...A	D...A	<(DHA)	
T=100K					
	0.97(2)	2.79(2)	3.6488(15)	147.0(17)	C1-H1B...Cl2_i
	0.92(2)	2.79(2)	3.6251(15)	150.9(17)	C1-H1C...Cl2_ii
T=150K					
	0.98	2.84	3.676(6)	144.0	C1^a-H1B^a...Cl2_i
	0.98	2.75	3.632(6)	150.0	C1^a-H1C^a...Cl2_iii
	0.98	3.00	3.73(6)	132.4	C1B^b-H1D^b...Cl2_iii
	0.98	2.72	3.46(5)	132.2	C1B^b-H1D^b...Cl3
	0.98	2.67	3.55(6)	149.1	C1B^b-H1E^b...Cl2_i
	0.98	2.92	3.63(5)	129.5	C1B^b-H1F^b...Cl1_iv
	0.965(19)	2.97(3)	3.64(6)	128(3)	C2B^b-H2E^b...Cl1_iii
T=200K					
	0.98	2.87	3.675(7)	140.5	C1^a-H1B^a...Cl2_i
	0.98	2.78	3.674(7)	152.5	C1^a-H1C^a...Cl2_iii
	0.98	2.83	3.59(2)	135.0	C1B^b-H1D^b...Cl2_iii
	0.98	2.88	3.547(16)	126.2	C1B^b-H1D^b...Cl3
	0.98	2.87	3.73(2)	147.9	C1B^b-H1E^b...Cl2_i
T=250K					
	0.97	2.88	3.630(15)	134.4	C1^a-H1B^a...Cl1_iv
	0.97	2.95	3.697(14)	134.8	C1^a-H1B^a...Cl2_i
	0.97	2.81	3.704(14)	154.0	C1^a-H1C^a...Cl2_iii
	0.97	2.84	3.63(3)	139.5	C1B^b-H1D^b...Cl2_iii
	0.97	2.93	3.50(3)	118.3	C1B^b-H1D^b...Cl3
	0.97	2.95	3.75(3)	141.1	C1B^b-H1E^b…Cl2_i
T=300K					
	0.96	2.75	3.576(15)	144.6	C1^a-H1B^a...Cl1_iv
	0.96	2.80	3.702(18)	157.4	C1^a-H1C^a...Cl2_iii
	0.96	2.77	3.44(2)	127.8	C1B^b-H1D^b...Cl3
	0.96	2.84	3.70(3)	149.5	C1B^b-H1E^b...Cl2_i
	0.94(2)	2.98(3)	3.65(3)	129.6(17)	C2B^b-H2E^b...Cl1_iii
T=310K					
	0.96	2.81	3.585(11)	138.0	C1^a-H1B^a...Cl1_iv
	0.96	2.84	3.707(14)	150.0	C1^a-H1C^a...Cl2_iii
	0.96	2.69	3.43(2)	134.9	C1B^b-H1D^b...Cl3
	0.96	2.79	3.69(3)	155.7	C1B^b-H1E^b...Cl2_i
	0.96	2.53	3.35(5)	143.4	C1C^c-H1I^c...Cl1_iii
	0.96	2.81	3.72(6)	158.3	C2C^c-H1J^c...Cl1_v
	0.96	2.71	3.48(7)	137.3	C2C^c-H1L^c...Cl1_iii
	0.96	2.92	3.70(6)	138.6	C3C^c-H1M^c...Cl1
	0.96	2.81	3.44(4)	124.6	C3C^c-H1O^c…Cl3_i

Symmetry operations:
(i) -x+1, -y+1, -z+1
(ii) x-1/2, -y+3/2, -z+1/2
(iii) x-1/2, y, -z+1/2
(iv) -x+1/2, -y+1, z+1/2
(v) x-1/2, -y+1/2, -z+1/2

**Table SI-3**. [(CH$_3$)$_3$S]$^+$ cation disorder vs temperature.

Temperature (K)	No disordered positions	Refined population parameters (%)
100	1*	100
150	2	92.3(2) / 7.7(2)
200	2	81.1(2) / 18.9(2)
250	2	71.4(3) / 28.6(3)
300	2	65.2(5) / 34.8(5)
310	4	60.0(3) / 25.7(3) / 7.11(14) / 7.11(14)**

(*) There are some low electron density residual peaks in the Fourier difference map that allow to construct and refine (with many constrains) a disordered model for [(CH$_3$)$_3$S]$^+$ in 2 orientations like that found at higher temperatures. The final refined population parameters are 99.07(13) / 0.93(13) %. It is a much more complicated model with no significant improvement in data fitting, therefore, the no disordered model is considered in the final refinement reported at 100K.

(**) Last two population values are identical because they correspond to disordered positions related by a mirror symmetry plane.

Chapter 4
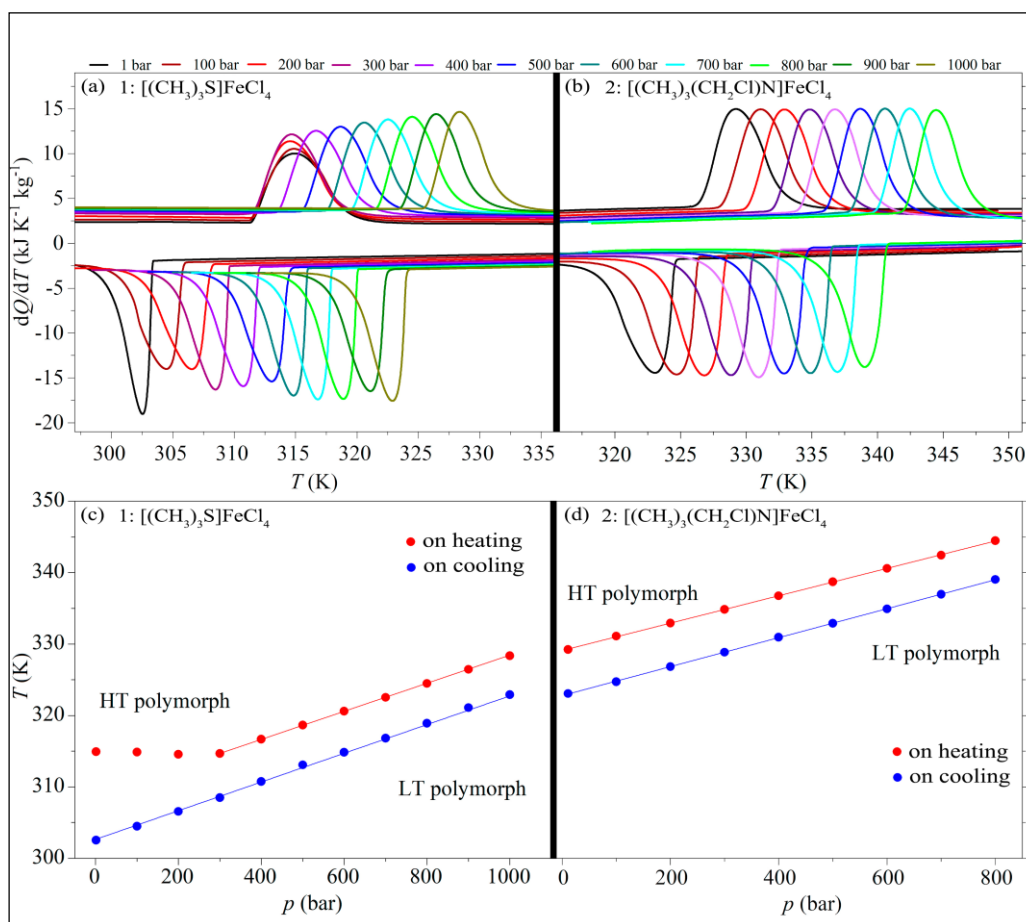
Chapter 4

[(CH₃)₃(CH₂Cl)N]FeCl₄ & [(CH₃)₃S]FeCl₄

$[(CH_3)_3(CH_2Cl)N]FeCl_4$ & $[(CH_3)_3S]FeCl_4$

Hybrid ionic plastic crystals in the race for enhanced low-pressure barocaloric materials.

Abstract: In this chapter, it is introduced a new family of barocaloric hybrid organic-inorganic compounds with colossal barocaloric effects. The here reported hybrid materials, $[(CH_3)_3(CH_2Cl)N]FeCl_4$ and $[(CH_3)_3S]FeCl_4$, exhibit a molecular structure composed by discrete inorganic anions and organic cations with weak elestrostatic interactions. The calorimetric studies reveal colossal barocaloric effects of similar magnitude than organic plastic crystals ($\Delta S > 100$ J K⁻¹ kg⁻¹) near room temperature and under smaller pressures ($p \leq 1000$ bar), which lead to higher barocaloric strengths. Therefore, the colossal large barocaloric strentgh, in addition to the low working pressure and near-room-temperature operation, offer a new family of compounds (that of ionic hybrid plastic crystals) to further explore in the search for improved barocaloric materials. This is of great interest since barocalorics have been proposed as strong candidates to reach zero-emission target by 2050, providing they can reduce their operating pressures, which traditionally are over 1000 bar.

4.1. Introduction

In the last years, the field of solid-state refrigeration has experienced a race for the discovery of the best barocaloric materials that could be viable for commercial implementation. As a matter of fact, the 2020 Henry Royce Institute's *road map* "materials for the energy transition" postulates the emerging barocaloric materials as a promising tool that would help to reach the target of net zero-emissions by 2050.[1]

Accordingly, solid-state barocaloric refrigeration arises as a promising alternative to the ubiquotous vapour-compresion systems, which use hazardous gases with environmental, efficiency and safety concerns (including greenhouse effect, fluid-originated thermal losses, toxicity, and/or flammability).[2–5] Barocaloric materials are solid-state compounds that can also provide refrigeration under a compression cycle, and avoid the latter concerns.[6–8] For a solid-state compound to be considered a good barocaloric, it should fulfill certain characteristics, specially: near-room-temperature phase transition, associated extremely large entropy changes, and easy-achievable operating pressures to avoid irreversible thermal losses.[9–12] In a first approximation, the ideal barocaloric material for commercial refrigeration would display colossal thermal changes (barocaloric effects of $\Delta S > 100$ J K⁻¹ kg⁻¹) near ambient temperature (from ~315 K down to ~273 K, or even lower in the case of freezing devices), and under the application of pressures well-below 1000 bar.[1] Thus, it is primordial to find materials with colossal and reversible isothermal entropy changes, ΔS_{rev}, (and adiabatic temperature changes, ΔT_{rev}), large barocaloric coefficient (dT_t/dp) and strength ($\Delta S_{rev}/\Delta p$)[13] (sensitivity to pressure) and appropiate operating temperature (T_{op})[14], which is the

thermal region where the barocaloric effect can be reversibly induced.

In the search for new materials that could fulfil those requirements, we found the first barocaloric materials operating under pressures easily-achievable by commercial compressors. As a matter of fact, we reported the barocaloric hybrid organic-inorganic perovskites $[TPrA]M[dca]_3$ (M = Mn²⁺ and Cd²⁺) that can operate under pressures as small as 70 bar near ambient temperature.[13,15,16] However, their barocaloric effects, although with values considered as giant ($|\Delta S_{rev}| = [10 - 40]$ J K⁻¹ kg⁻¹), were still far from the mentioned colossal magnitude. Soon after that, it was reported another hybrid perovskite, $[(CH_3)_4N]Mn[N_3]_3$, with improved near-colossal barocaloric effects ($|\Delta S_{rev}| \sim 70$ J kg⁻¹ K⁻¹) at the expense of increasing the operating pressure at 900 bar.[12] The giant barocaloric effects in these hybrid perovskites are related to the large structural disordering when undergoing the pressure-induced order-disorder phase transition. However, their crystal structures are formed by 3D-frameworks linked by strong chemical bonds, which limits the aforementioned disordering and, consequently, the magnitude of the barocaloric effects.

Even more recently, this limitation has been overcome in a long-known family of molecular organic plastic crystals,[17–19] which exhibit weaker chemical bonds. Therefore, these molecular compounds exhibit plastic crystal behaviour with extremely large disordering across the order-disorder phase transition. Up-to-date, these compounds exhibit record colossal barocaloric effects. A very remarkable example is neopentylglycol (NPG) with a value of $|\Delta S_{rev}| \sim 383$ J kg⁻¹ K⁻¹. However, this material requires operating pressures above 2500 bar, which hinders its commercial applications.[18] This large pressure requirement has been recently reduced in another family

of also long-known molecular organic plastic crystals, 1-haloadamantanes,[20] which exhibit reversible barocaloric effects of $|\Delta S_{rev}| \sim 153$ J K^{-1} kg^{-1} under pressures of 1000 bar.

In this work, the aim is to combine the advantages of all the above-mentioned materials, and explore the barocaloric effects in an emerging family of hybrid organic-inorganic materials with molecular (instead of 3D-framework) structure and plastic crystal behaviour. In particular, we focus on the [(CH$_3$)$_3$(CH$_2$Cl)N]FeCl$_4$ (**1**) and [(CH$_3$)$_3$S]FeCl$_4$ (**2**) compounds, which have been recently reported as multifunctional compounds with interesting magnetic and electric properties, as well as for thermal energy storage.[21,22]

These hybrids contain polyatomic organic (alkylammonium) cations and polyatomic inorganic (tetrachloroferrate) anions, while maintaining the molecular nature of the organic plastic crystals. The presence of weak chemical interactions between the ionic building-blocks allows for a large pressure responsiveness and barocaloric coefficient. At the same time, this pressure responsiveness is enhanced by the soft nature of organic components, meanwhile the inorganic components increase the materials density that allows for a larger volumetric barocaloric effect.

4.2. Experimental section

4.2.1 Materials

The following chemicals were used in the synthesis as-puchased and without further purification: (CH$_3$)$_3$N solution (45 wt. % in H$_2$O Sharlab), CH$_2$Cl$_2$ (99% anhydrous Sigma Aldrich), HCl (ca. 37 % in H$_2$O ACS reagent, ACROS Organics), [(CH$_3$)$_3$S]Br (98% Sigma-Aldrich), and FeCl$_3$·6H$_2$O (98% Sigma-Aldrich).

4.2.2. Synthesis

In this work, the hybrid ionic plastic crystals of [(CH$_3$)$_3$N(CH$_2$Cl)]FeCl$_4$ (**1**) and [(CH$_3$)$_3$S]FeCl$_4$ (**2**) were synthesized following the procedure reported in the literature.[21,22] The precursor [(CH$_3$)$_3$(CH$_2$Cl)N]Cl for the compound **1** was prepared by mixing (CH$_3$)$_3$N solution in an excess of CH$_2$Cl$_2$ stirring at room temperature. Crystals of (**1**) were synthesized by mixing stoichiometric amounts of the precursor [(CH$_3$)$_3$(CH$_2$Cl)N]Cl and FeCl$_3$·6H$_2$O and slow evaporation.

Crystals of (**2**) were obtained by slow evaporation of an aqueous solution containing [(CH$_3$)$_3$S]Br and FeCl$_3$·6H$_2$O in stoichiometric proportion, and an excess of HCl.

4.2.3. Powder X-ray diffraction

X-ray powder diffraction (XRPD) studies at room temperature were performed in a Siemens D-5000 diffractometer using CuKα radiation (λ = 1.5418 Å). The experimental XRPD pattern was compared with the profile obtained from the single crystal structure, which was generated by the Mercury 3.5.1 software.

4.2.4. Differential scanning calorimetry

Atmospheric and variable-pressure differential scanning calorimetry (DSC) analyses were performed in a Setaram μDSC7 EVO microcalorimeter equipped with a pressure pump with nitrogen gas as a pressure-transmitting media. Quasi-direct barocaloric measurements were made for ~100 mg of each compound at ± 1.2 K min^{-1} and at different isobaric pressures. Direct measurements were carried out with the same amount of sample with a ± 10 bar min^{-1} swept in pressure.

4.3. Results and discussion

4.3.1. Powder X-ray diffraction

The purity and crystallinity of the obtained samples were confirmed by comparison of the acquired powder X-ray diffraction patterns (Fig. 4-1) with the patterns simulated from single-crystal X-ray diffraction data.[21,22].
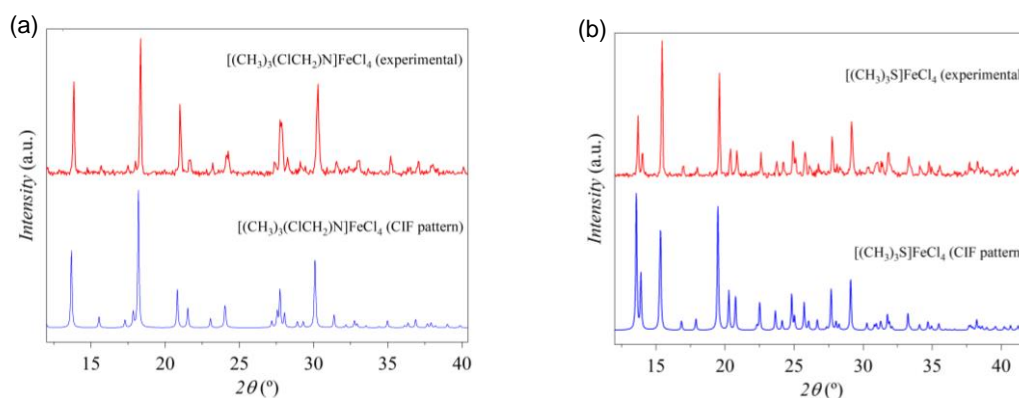
Figure 4-1. Powder x-ray diffraction patterns at room temperature for the as-prepared a) [(CH$_3$)$_3$N(CH$_2$Cl)]FeCl$_4$ and b) [(CH$_3$)$_3$S]FeCl$_4$ compounds. The experimental diffractogram is red-coloured and the simulated one is blue, based on their single crystal structure at room temperature.
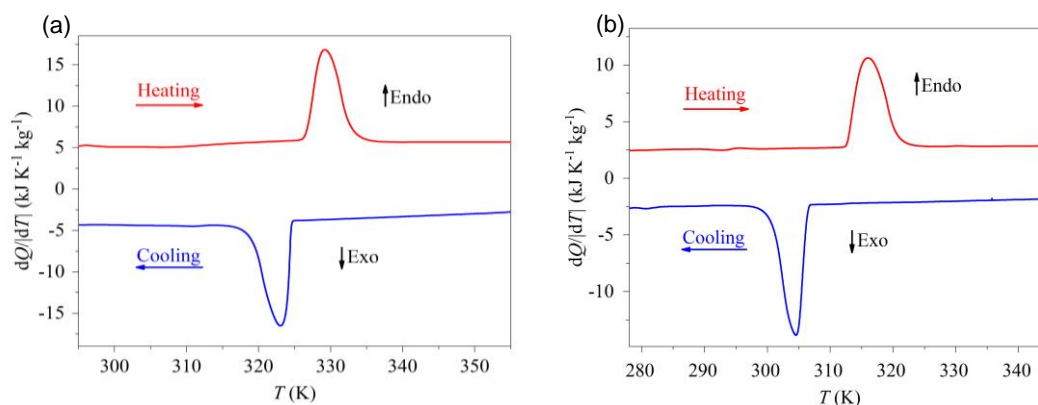
Figure 4-2. Heat flow dQ/|dT| as a function of temperature at atmospheric pressure for (a) [(CH$_3$)$_3$N(CH$_2$Cl)]FeCl$_4$ **(1)** and (b) [(CH$_3$)$_3$S]FeCl$_4$ **(2)**.
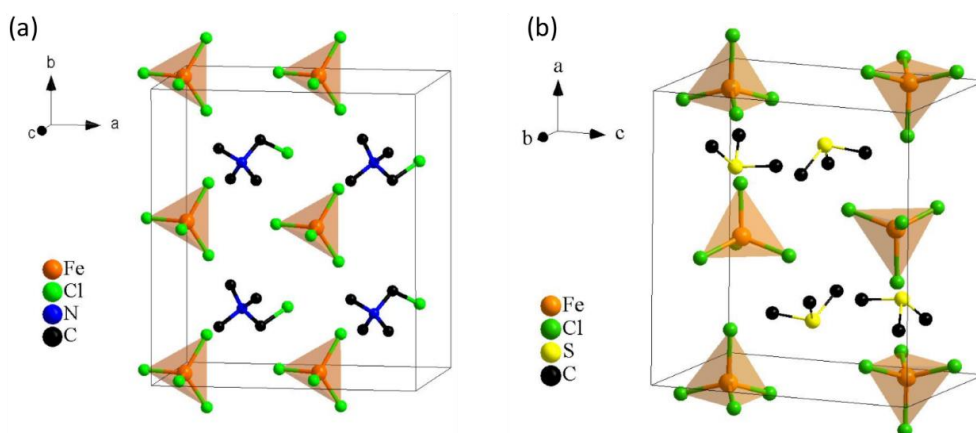
Figure 4-3. Crystal structure of the low-temperature polymorphs of (a) [(CH$_3$)$_3$N(CH$_2$Cl)]FeCl$_4$ **(1)** and (b) [(CH$_3$)$_3$S]FeCl$_4$ **(2)**.

4.3.2. Differential scanning calorimetry

These samples were studied by differential scanning calorimetry (DSC) at ambient pressure, which showed a first-order phase transition for each of these compounds (Fig. 2). Compounds **(1)** and **(2)** display a phase transition at $T_t \sim$ 326 K and $T_t \sim$ 315 K on heating, with a thermal hysteresis of ~ 4 K and ~13 K, respectively.

Latent heat and entropy change were obtained by the integration of the peaks in heat flow. The resulting values were $|Q_0| \sim$ 46 kJ kg^{-1} and $|\Delta S| \sim$ 140 J kg^{-1} K^{-1} for compound **(1)**, and $|Q_0| \sim$ 40 kJ kg^{-1} and $|\Delta S| \sim$ 130 J kg^{-1} K^{-1} for compound **(2)**. These large thermal changes are in fully agreement with the literature, and they are related to an increase in the structural disorder from a crystalline phase (Fig. 4-3) towards a plastic crystal state.[21,22]

Additionally, in order to study the barocaloric properties of these ionic plastic crystals, DSC analysis were carried out at different pressures (Fig. 4-4). In compound **(1)**, the pressure increase shifts the transition temperature towards higher values according to a barocaloric coefficient[13] of dT/d$p \sim$ 19.7 K kbar^{-1} (Fig. 4-4a,b) This is consistent with an enhanced stability of the more ordered and lower

volume LT-phase at the expense of the more disordered HT-phase due to pressure.

On the other hand, in compound **(2)** the transition temperature on cooling shifts towards higher values with a value of dT/d$p \sim$ 19.9 K kbar^{-1}. Interestingly, T_t on heating shows inertia towards pressure and remains pressure-independent up to 300 bar. Meanwhile for pressures above 300 bar, T_t moves to higher values with a barocaloric coefficient similar to that of the cooling ramp (dT/d$p \sim$ 19.9 K kbar^{-1}), see Fig 4-4c,d. This is an anomalous phenomenon (whose origin will be further explored in future publications) that decreases the thermal hysteresis from 13 K at ambient pressure down to 6 K from 300 bar upward. Therefore, in compound **(2)**, the thermal losses due to the hysteresis would be reduced at higher pressures. These findings will encourage to further study the origin of this pressure inertia using specific characterization techniques (which are not the scope of the present studies), in order to stablish new mechanism to reduce the thermal hysteresis.

Using these calorimetric data, the barocaloric effect was estimated in terms of isothermal entropy change by quasi-direct methods, $\Delta S_{it(q-d)}$.[23] For this purpose, isobaric entropy changes (ΔS_{ib}) were calculated for each pressure

by integrating the heat flow $dQ/|dT|$ over temperature curves (Fig. 4-5). The obtained data shows that, across the phase transition, the value of the isobaric entropy changes (ΔS_{ib}) increases up to a plateau of $|\Delta S_{ib}| \sim 131$ J kg^{-1} K^{-1} and $|\Delta S_{ib}| \sim 126$ J kg^{-1} K^{-1} for compounds **1** and **2**, respectively. It is worth noting that this maximum value is independent of the applied pressure for compound **2**, while for compound **1** it slightly decreases with pressure (from ~ 131 J kg^{-1} K^{-1} at 1 bar down to ~ 110 J kg^{-1} K^{-1} at 800 bar).
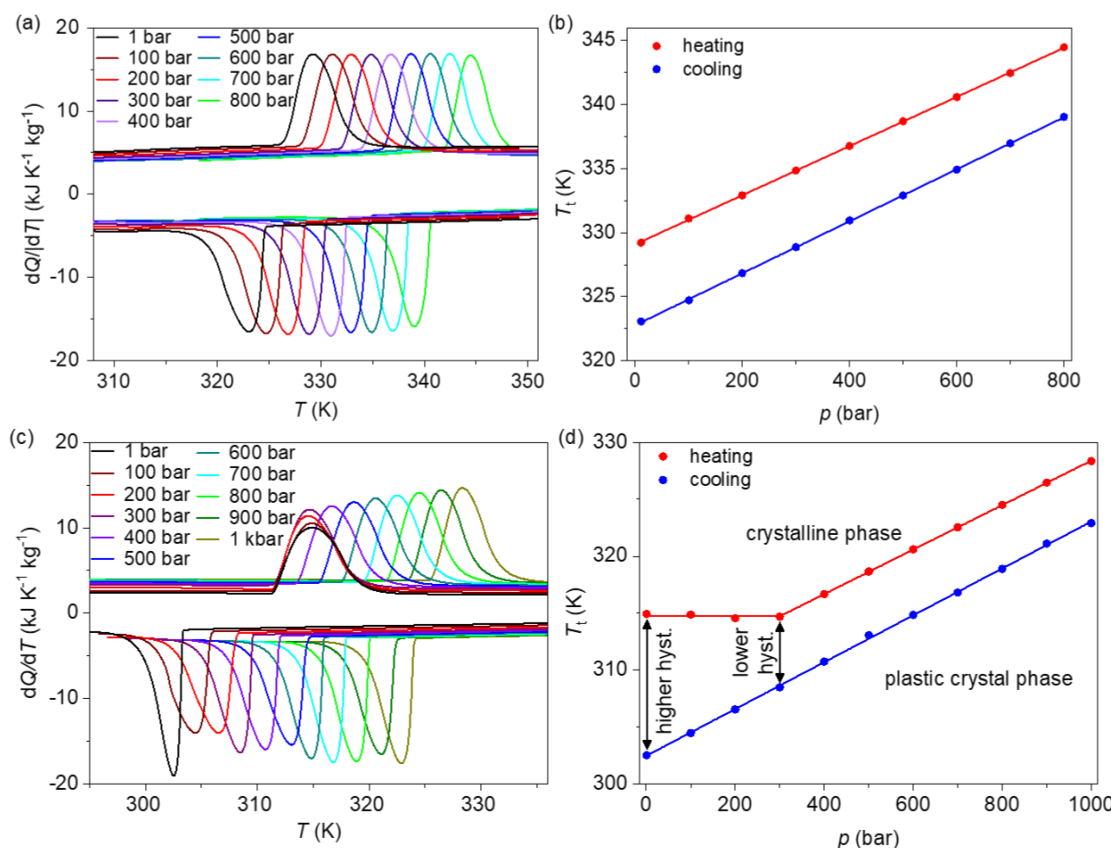
Figure 4-4. Calorimetric curves of $dQ/|dT|$ versus T at different pressures for compounds (a) $[(CH_3)_3(ClCH_2)N]FeCl_4$ (**1**) and (b) $[(CH_3)_3S]FeCl_4$ (**2**). Transition temperature versus pressure for (b) $[(CH_3)_3(ClCH_2)N]FeCl_4$ (**1**) and (d) $[(CH_3)_3S]FeCl_4$ (**2**), identified using the peak in the $dQ/|dT|$ curves. Note: the thermal hysteresis of compound (**2**) gets reduced for $p > 300$ bar.
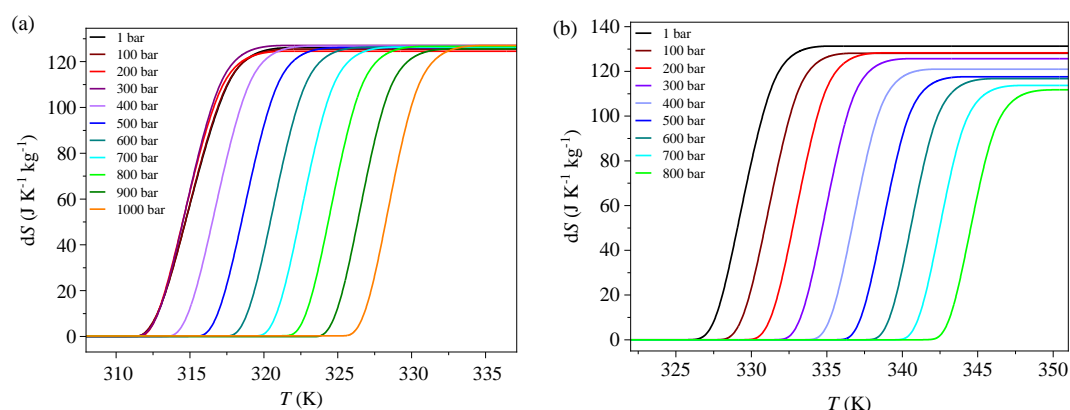
Figure 4-5. Thermally driven isobaric changes in entropy on heating with respect to the low-temperature phase for each pressure for (a) $[(CH_3)_3(ClCH_2)N]FeCl_4$ (**1**) and (b) $[(CH_3)_3S]FeCl_4$ (**2**)
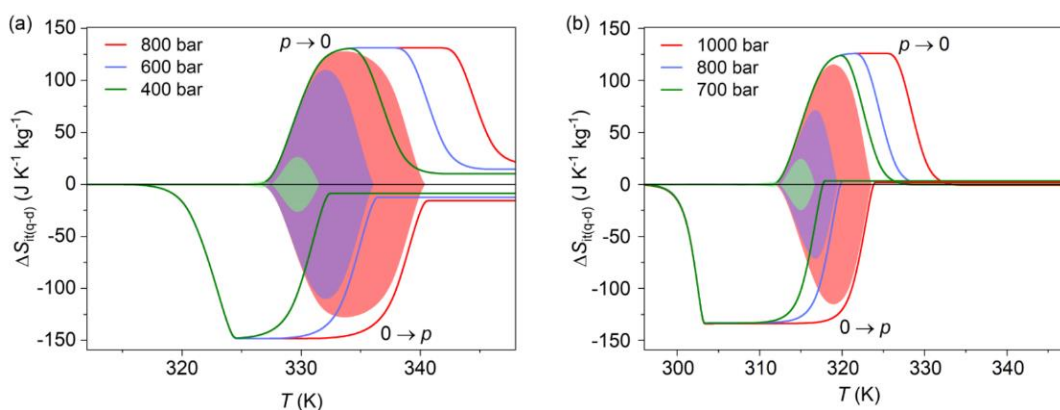
The pressure-driven isothermal changes in entropy, $\Delta S_{it(q-d)}$ (see Fig. 4-6), were obtained as the difference between thermally-driven changes in entropy at two different pressures, ΔS_{ib}, with the following equation (1):

$$\Delta S_{it(q-d)} = \Delta S_{ib}(p \neq 1, T) - \Delta S_{ib}(p = 1, T) \quad (1)$$

Interestingly, these results reveal colossal barocaloric effects in the case of compound (1), which can be reversibly reached under pressures as small as 800 bar ($|\Delta S_{it(q-d)rev}| \sim 123$ J K^{-1} kg^{-1}). Furthermore, the operating temperature range at this pressure is as large as 13 K. In the case of compound (2), the barocaloric effects are similar ($|\Delta S_{it(q-d)rev}| \sim 125$ J K^{-1} kg^{-1}) although require the application of slightly larger pressures ($p = 1$ kbar) to

induced them reversibly. In this latter material, the operating temperature change is also similar to compound (1), with a value of 7 K at 1 kbar. It should be noted that additional changes in isothermal entropy[9] that arise due to volumetric thermal expansion were not considered. This is because the coefficient of thermal expansion decreases significantly under pressure in soft materials.[12,24]

It is worth noting that the barocaloric coefficients of compounds (1) and (2), although smaller than those reported for 1-haloadamantanes and hybrid perovskites, are still larger than for most of barocaloric organic plastic crystals.[17,18,20]

Figure 4-6. Pressure-driven isothermal changes in entropy on applying ($0 \rightarrow p$) and removing ($p \rightarrow 0$) selected hydrostatic pressures. The data shaded using different colours represent the reversible barocaloric response at different pressures for the compound (a) [(CH$_3$)$_3$(ClCH$_2$)N]FeCl$_4$ (1) and (b) [(CH$_3$)$_3$S]FeCl$_4$ (2).
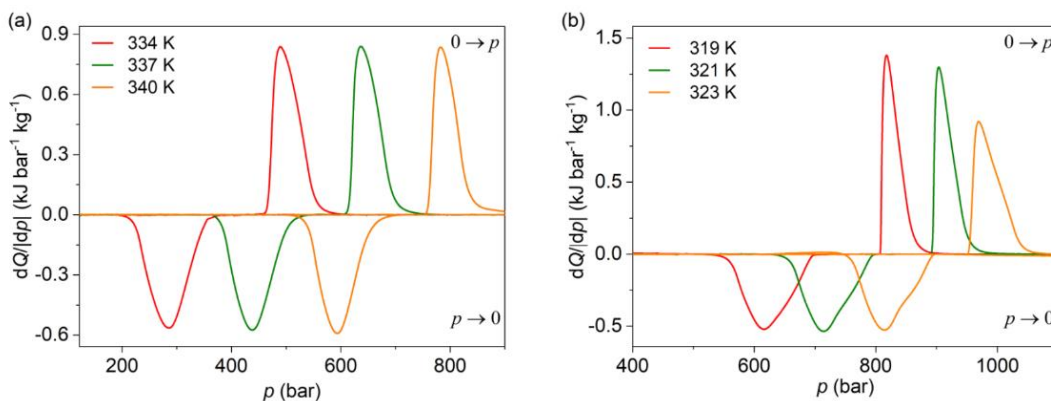
Figure 4-7. Heat flow dQ/|dp| on cycles of applying ($0 \rightarrow p$) and removing ($p \rightarrow 0$) hydrostatic pressure at different temperatures for compound (a) [(CH$_3$)$_3$(ClCH$_2$)N]FeCl$_4$ (1) and (b) [(CH$_3$)$_3$S]FeCl$_4$ (2). Note: baseline was subtracted for a better visualization.

In order to confirm the colossal values of the barocaloric effects, the entropy changes provoked by pressure were also studied under experimental isothermal conditions, $\Delta S_{it(direct)}$, which is known as direct measurements.[23] These conditions are more representative of real practical applications, where the materials are under continuous pressure cycles.[23] In that regard, Figure 4-7 shows the heat flow dQ/|dp| on compression-decompression cycles at different temperatures.

The integration of those curves shows that compound (1) displays a value of $|\Delta S_{it(direct)}| \sim 147$ J K^{-1} kg^{-1} at 334 K and 600 bar. As for compound (2), the observed barocaloric effect is as large as $|\Delta S_{it(direct)}| \sim 131$ J K^{-1} kg^{-1} at 319 K and 900 bar. It worth noting that these values show a slightly better performance (larger barocaloric effects under smaller pressures) than estimated by quasi-direct methods.

4.4. Conclusions

In summary, it is reported the outstanding barocaloric properties of two hybrid ionic plastic crystals with discrete ionic building-blocks. The weak chemical interactions and the soft nature of the organic cations allow these materials to exhibit a very large pressure responsiveness with remarkable barocaloric coefficients ($dT_t/dp \sim 20$ J kbar^{-1}) and barocaloric strengths ($|\Delta S_{rev}|/\Delta p > 120$ J K^{-1} kg^{-1} or > 200 J K^{-1} l^{-1}). Moreover, the hybrid ionic plastic crystals can operate under relatively low pressures and in a large operating temperature range near room temperature. Therefore, this work experimentally demonstrates that, as recently predicted,[25] hybrid ionic plastic crystals are a new family of promising compounds in the race towards the design of enhanced barocaloric materials for solid-state refrigeration. Also, these compounds were reported before with other interesting properties as dielectrics or ferroelectricity.[21,22] Taking this multi-functionality into account, in addition to the large availability of the forming elements of the compounds, organic-inorganic plastic crystals are a promising family that could open the door to the next generation of multicaloric materials, encouraging future studies on the combination of these different properties.

4.5. Notes

The work showed and discussed in this chapter has been published in the following pre-print:

J. Salgado-Beceiro, J. M. Bermudez-García, E. Stern-Taulats, J. García-Ben, S. Castro-García, M. Sanchez-Andujar, X. Moya and M. A. Señarís-Rodríguez, *ChemRxiv*, 2020.

4.6. References

1   X. Moya and I. M. Ilevbare, *Henry Royce Inst.*, 2020.

2   J. M. Calm, *Int. J. Refrig.*, 2008, **31**, 1123–1133.

3   Y. T. Ge and S. A. Tassou, *Energy Convers. Manag.*, 2014, **78**, 245–252.

4   A. Cavallini, G. Censi, D. Del Col, L. Doretti, G. A. Longo and L. Rossetto, *Int. J. Refrig.*, 2001, **24**, 73–87.

5   J. M. Gonçalves, C. Melo, C. J. L. Hermes and J. R. Barbosa Jr, *J. Brazilian Soc. Mech. Sci. Eng.*, 2011, **33**, 159–165.

6   V. W. Bhatkar, V. M. Kriplani and G. K. Awari, *Int. J. Environ. Sci. Technol.*, 2013, **10**, 871–880.

7   A. Greco, C. Aprea, A. Maiorino and C. Masselli, *Int. J. Refrig.*, 2019, **106**, 66–88.

8   A. Kitanovski, U. Tomc and A. Poredo, *Int. J. Refrig.*, 2015, **57**, 288–298.

9   P. Lloveras, E. Stern-Taulats, M. Barrio, J. L. Tamarit, S. Crossley, W. Li, V. Pomjakushin, A. Planes, L. Mañosa, N. D. Mathur and X. Moya, *Nat. Commun.*, 2015, **6**, 8801.

10   M. V Gorev, E. V Bogdanov and I. N. Flerov, *J. Phys. D. Appl. Phys.*, 2017, **50**, 384002.

11   C. Aprea, A. Greco, A. Maiorino and C. Masselli, *Climate*, 2019, **7**, 9.

12   J. Salgado-Beceiro, A. Nonato, R. X. Silva, A. García-Fernández, M. Sánchez-Andújar, S. Castro-Garcia, E. Stern-Taulats, M. A. Señarís-Rodríguez, X. Moya and J. M. Bermúdez-García, *Mater. Adv.*, 2020, **1**, 3167–3170.

13   J. M. Bermúdez-García, M. Sánchez-Andújar, S. Castro-García, J. López-Beceiro, R. Artiaga and M. A. Señarís-Rodríguez, *Nat. Commun.*, 2017, **8**, 15715.

14   A. Aznar, P. Lloveras, M. Romanini, M. Barrio, J. L. Tamarit, C. Cazorla, D. Errandonea, N. D. Mathur, A. Planes, X. Moya and L. Mañosa, *Nat. Commun.*, 2017, **8**, 1.

15   J. M. Bermúdez-García, S. Yáñez-Vilar, A. García-Fernández, M. Sánchez-Andújar, S. Castro-García, J. López-Beceiro, R. Artiaga, M. Dilshad, X. Moya and M. A. Señarís-Rodríguez, *J. Mater. Chem. C*, 2018, **6**, 9867–9874.

16   J. M. Bermúdez-García, M. Sánchez-Andújar and M. A. Señarís-Rodríguez, *J. Phys. Chem. Lett.*, 2017, **8**, 4419–4423.

17   A. Aznar, P. Lloveras, M. Barrio, P. Negrier, A. Planes, L. Mañosa, N. Mathur, X. Moya and J. L. Tamarit, *J. Mater. Chem. A*, 2020, **8**, 639–647.

18   P. Lloveras, A. Aznar, M. Barrio, P. Negrier, C. Popescu, A. Planes, L. Mañosa, A. Avramenko, N. D. Mathur, X. Moya and J. Tamarit, *Nat. Commun.*, 2019, **10**, 1803.

19   B. Li, Y. Kawakita, S. Ohira-Kawamura, T. Sugahara, H. Wang, J. Wang, Y. Chen, S. I. Kawaguchi, S. Kawaguchi, K. Ohara, K. Li, D. Yu, R. Mole, T. Hattori, T. Kikuchi, S. ichiro Yano, Z. Zhang, Z. Zhang, W. Ren, S. Lin, O. Sakata, K. Nakajima and Z. Zhang, *Nature*, 2019, **567**, 506–510.

20   A. Aznar, P. Negrier, A. Planes, L. Mañosa, E. Stern-Taulats, X. Moya, M. Barrio, J.-L. Tamarit and P. Lloveras, *Appl. Mater. Today*, 2021, **23**, 101023.

21   J. Salgado-Beceiro, J. M. Bermúdez-García, A. L. Llamas-Saiz, S. Castro-García, M. A. Señarís-Rodríguez, F. Rivadulla and M. Sánchez-Andújar, *J. Mater. Chem. C*, 2020, **8**, 13686–13694.

22   D. Li, X.-M. Zhao, H.-X. Zhao, L.-S. Long and L.-S. Zheng, *Inorg. Chem.*, 2019, **58**, 655–662.

23   X. Moya, S. Kar-Narayan and N. D. Mathur, *Nat. Mater.*, 2014, **13**, 439–450.
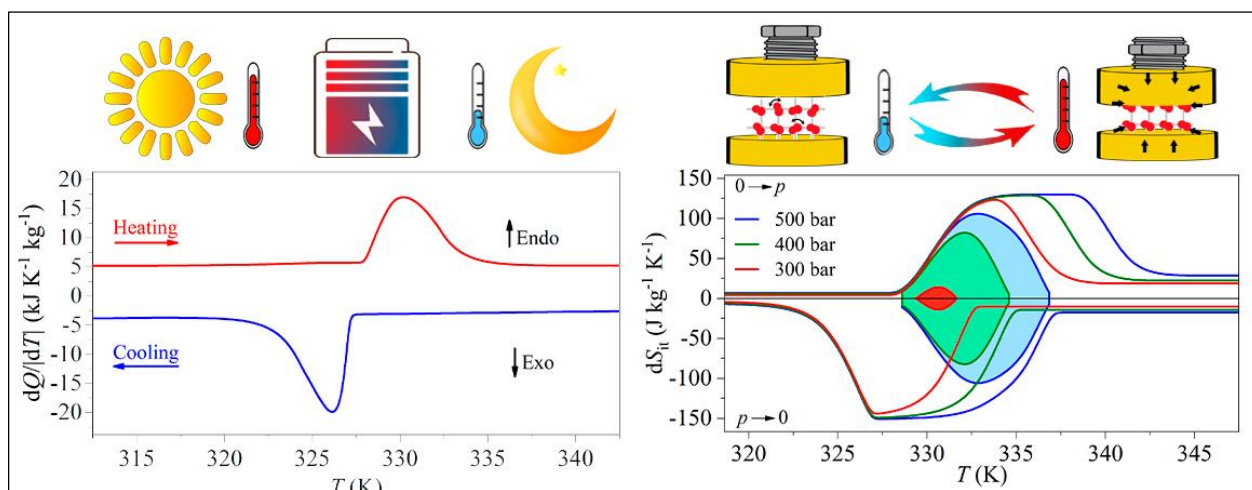
24   D. Walsh and P. Zoller, *Standard Pressure*

Volume Temperature Data for Polymers, Taylor & Francis, 1995.

25   D. Boldrin, *Appl. Phys. Lett.*, 2021, **118**, 170502.

Chapter 5

Chapter 5

$[(CH_3)_3(CH_2Cl)N]GaCl_4$

Multi-sensitive polar ionic plastic crystal $[(CH_3)_3(CH_2Cl)N]GaCl_4$ with barocaloric effect for solid-state cooling and multi-energy storage applications.

Abstract: This chapter focuses in the study of the novel plastic crystal $[(CH_3)_3(CH_2Cl)N]GaCl_4$ for energy storage and solid-state cooling applications. The novelty of this study is remarkable given the few publications of hybrid organic-inorganic plastic crystals for such applications. This new compound undergoes a crystal-to-plastic crystal phase transition at 330 K (on heating) and 326 K (on cooling) involving an intense latent heat (~44 kJ kg^{-1}). These parameters, among others, make this material very interesting for solar thermal energy storage applications. In addition, this phase transition was studied as a function of pressure. The results show a barocaloric transition with a reversible barocaloric effect of ~105 J kg^{-1} K^{-1} at 500 bar. This high value, combined with a relatively high sensitivity to pressure (22 K kbar^{-1}) makes this plastic crystal a promising candidate for solid-state cooling. Furthermore, the compound exhibit other interesting switching properties, as dielectric. The material undergoes a sharp dielectric transition as a function of temperature, increasing its dielectric constant up to 3 times. Also, given the non-centrosymmetric nature of the compound, polarization(P)-electric(E) field hysteresis loops were carried out in search of possible ferroelectricity. The combination of properties offered by this hybrid plastic crystal implies that $[(CH_3)_3(CH_2Cl)N]GaCl_4$ is a multi-sensitive compound with multi-functional properties for energetic applications.

5.1. Introduction

Phase change materials (PCM) have been focus of attention for the last decades due to their multiple applications.[1] They can be found in different important technologies, such as thermal energy storage (TES)[2], photonics[3], cooling[4], memories[5], sensors[6] and so on. Typically, the PCM employed in many of the mentioned applications (especially those involving TES and cooling) involve liquid-gas and liquid-solid transitions with large heat exchange generated in these transformations.[7–9] However, fluids has some intrinsic problems associated to their use, like risk of leakages and/or volatilization of the liquid phase, low thermal stability, difficult manipulation and a more challenging design of the containers. Furthermore, many of the employed fluids, in particular for cooling technologies, are polluting and represent an important contribution to the global warming because of their greenhouse nature.[10] In view of the problems of some fluids, solid-solid PCM offer significant advantages, especially in energy technologies like TES and solid state cooling (SSC).[11,12] TES and SSC are emergent technologies that take advantage of the latent heat (for TES) and entropic change (for SSC) involved phase transitions.

In this context, an ideal TES material should have large latent heat, high specific heat (for sensible heat storage), high thermal stability, low thermal expansion and high density, among others.[13,14] Organic compounds like polyalcohols (neopentylglycol and derivatives)[15,16] or paraffins[17] have been intensively studied for TES

applications due to their high latent heat associated to their peculiar solid-solid phase transitions. These organic materials undergo a phase change from a crystalline and ordered state at low temperature to a crystalline and dynamically disorder state at high temperature, where the molecules exhibit rotational degree of freedom while the molecular center keeps fixed in the crystalline lattice. This latter state is called plastic crystal state and the materials with this peculiar state are named as plastic crystals (PCs).[18,19]

Recently, organic PCs have also emerged as promising compounds for SSC, in particular as barocaloric materials. Barocaloric materials are solid-state compounds that exhibit large thermal changes and isothermal entropy changes (ΔS) or adiabatic temperature changes (ΔT). These thermal changes are generally related to volume variation (ΔV) in the materials induced by the application of external pressure. A good barocaloric material should have high sensitivity to pressure, large and reversible entropy changes under the lowest possible external pressure.[20] The organic PCs stand out for their high entropy change, whose values are even similar to the reported for fluids that are currently used on cooling technology.[21,22]

Nevertheless, organic PCs have low decomposition temperatures, some are flammable, have low density (which supposes a low TES per unit of mass) and most of them show a low reversibility as barocaloric materials (which means high operational pressures).[17,23,24] Therefore, it is necessary to keep looking for new TES

and BC materials, which avoid the aforementioned limitations.

In this context, hybrid ionic plastic crystals (HIPCs) have emerged as promising TES and BC materials.[25,26] These ionic PCs are formed by an organic cation combined with an inorganic anion (commonly, an halometallate).[26] Interestingly, HIPCs have been studied due to other interesting functional properties, related with the presence of transition metals, such as magnetism, optical properties, ferroelectricity, etc.[25,27–30]

This work focuses on a novel HIPC with formula $[(CH_3)_3(CH_2Cl)N]GaCl_4$, which exhibits a PC phase transition around $T_h \sim 330$ K. Remarkably, the obtained material displays interesting caloric and barocaloric properties related with the observed phase transitions and make this compound a promising candidate for both TES and SSC applications. Furthermore, the dielectric behaviour could open the possibility of using this material into a capacitor to store electrical energy, so it would be considered as a multi-energy storage[30] compound.

5.2 Experimental section

5.2.1. Materials

The following chemicals were used in the synthesis as-purchased and without further purification: $(CH_3)_3N$ solution (45 wt. % in H_2O Sharlab), CH_2Cl_2 (99% anhydrous Sigma Aldrich), and $GaCl_3$ (99% Scharlab).

5.2.2. Synthesis

The precursor $[(CH_3)_3(CH_2Cl)N]Cl$ was prepared by mixing $(CH_3)_3N$ in an excess of CH_2Cl_2 stirring at room temperature for 24 hours. The resulting white solid was obtained by removing the solvent under reduced pressure at 343 K.[25]

Colorless polycrystalline powder of $[(CH_3)_3(CH_2Cl)N]GaCl_4$ was synthesized by mixing stoichiometric amounts of $[(CH_3)_3(CH_2Cl)N]Cl$ and $GaCl_3$ in H_2O and removal of the solvent under reduced pressure.

5.2.3. Powder X-ray diffraction

Variable-temperature powder X-ray diffraction (PXRD) using $\lambda = 0.92636$ Å at beamline BM01, Swiss Norwegian Beam line (SNBL) at the European Synchrotron Radiation Facility (ESRF). For this experiment, 0.5 mm diameter quartz capillaries were filled with $[(CH_3)_3(CH_2Cl)N]GaCl_4$ powder and measured *in situ* during thermal cycling between from 200 to 400 K. The temperature was controlled with an Oxford Cryostream 700+ and diffraction data was collected with a Pilatus 2M detector. The recorded 2D patterns were integrated into a 1D powder profile and fitted using the Le Bail method. The whole diffraction patterns were refined using the GSAS-II software.[31]

5.2.4. Thermogravimetric analysis

Thermogravimetric analyses (TGA) were performed in a TGA-DTA Thermal Analysis SDT2960 equipment. About 25 mg of grounded powder were heated at 5 K/min from 293 to 1200 K using a corundum crucible under dry nitrogen flow.

5.2.5. Variable-pressure differential scanning calorimetry

Atmospheric and variable-pressure differential scanning calorimetry (DSC and P-DSC, respectively) was performed with a Setaram mDSC7 EVO microcalorimeter equipped with a 65D Isco pressure pump that utilized nitrogen gas as pressure transmitting media. For the measurements, ~20 mg of sample were swept in temperature from 300 to 360 K at ± 1.2 K min^{-1} at different isobaric pressures from atmospheric pressure to 500 bar.

5.2.6. Dielectric properties

For the sample preparation, $[(CH_3)_3(CH_2Cl)N]GaCl_4$ was hot pressed into a polycrystalline free-standing thick film by applying uniaxial pressure of approximately 10 MPa at a temperature of 390 K. The powder was placed between two aluminium foil buffer layers and sandwiched between two 3 mm thick steel plates. The sample/foil/plate stack was then placed directly in the uniaxial hot press which was preheated to the desired temperature. When the pressure was released, the sample was air quenched by being removed to a room temperature steel bench top to cool under ambient conditions. The pressed sample was then broken into approximately 5 mm^2 samples, although the exact geometry varied. 3 mm diameter gold electrodes were sputter coated through a shadow mask onto samples. Dielectric capacitance and loss were measured with a Hewlett Packard LCR meter 4142 as function of frequency from 0.001 Hz to 0.1 MHz and as function of temperature from 298 K to 353 K.

5.2.7. Electric field hysteresis measurements

Electric field switching measurements were performed with an Aixacct TF analyser with a Trek 10 kV signal amplifier and a laser interferometer for strain measurement. All samples had seen no prior electric field other that used for dielectric measurements before the measurements. A triangular waveform was used for all measurements with frequencies between 0.1 and 100 Hz. The electric field was applied in single cycles in positive,

then negative field directions and the field amplitude was increased incrementally for each cycle in intervals of 10 kV/cm. At various amplitudes the cycles were repeated at different frequencies.

5.3. Results and discussion

5.3.1. Basic characterization

As the obtained compound is synthesized here by the first time, we carried out a basic characterization to confirm the purity, thermal stability and presence of any phase transition.

Also, it is worth to note that the structural characterization of this compound was carried out using polycrystalline powders, because it has not been possible to obtain suitable single crystals to carry out the structural determination by single crystal X-ray diffraction.

To confirm the purity of the $[(CH_3)_3(CH_2Cl)N]GaCl_4$ compound, the obtained powder X-ray diffraction pattern was compared with the crystal structure of $[(CH_3)_3(CH_2Cl)N]FeCl_4$ reported at literature[25] (see Fig. 5-1). There is a good agreement between both patterns, which confirms that both compounds are isostructural.
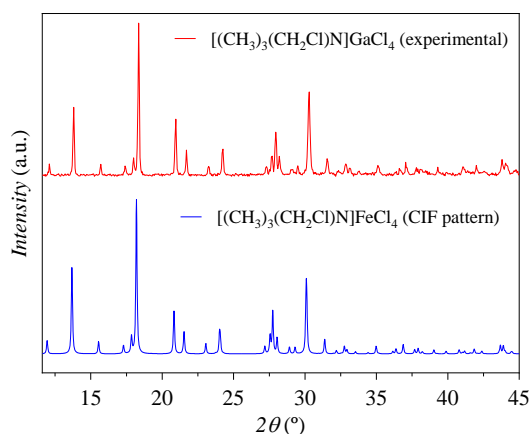
Figure 5-1. XRPD patterns at room temperature for the prepared $[(CH_3)_3(CH_2Cl)N]GaCl_4$ compound and the simulated one based on the single crystal structure at room temperature from literature[25] of $[(CH_3)_3(CH_2Cl)N]FeCl_4$.

TGA measurements (showed in Fig. 5-2a) revealed that $[(CH_3)_3(CH_2Cl)N]GaCl_4$ has a decomposition temperature of 420 K. Above this temperature, there is a two-steps decomposition: the first weight loss (~25 %) corresponds to part of the $[(CH_3)_3(CH_2Cl)N]^+$ cations at 420 K; above 500 K, there is another weight loss (~55 %), corresponding to the remaining atoms of N and Cl, remaining metallic Ga as residue (~20 %).

The DSC measurements (see Fig. 5-2b) show that $[(CH_3)_3(CH_2Cl)N]GaCl_4$ undergoes a reversible first-order phase transition with an endothermic peak at T_h ~

330 K on heating and an exothermic peak at T_c ~ 326 K at atmospheric pressure. The thermal hysteresis between heating and cooling ($\Delta T = T_h - T_c$) has a value of 4 K.

The associated latent heat (ΔH) and entropy change (ΔS) were calculated by integrating the peaks of the heat flow plots, obtaining the values of ΔH_h ~ 41 kJ kg^{-1} and ΔH_c ~ 47 kJ kg^{-1}; and ΔS_h ~ 123 J kg^{-1} K^{-1} and ΔS_c ~ 144 J kg^{-1} K^{-1}.

If the configurational entropy is considered as the main contribution to the total ΔS, the number of possible configurations N was calculated using the equation 1:

$$\Delta S = R\ln(N) \tag{1}$$

where R the gas constant, obtaining a value of $N = 114$. This high number of configurations is typical of plastic crystals, which commonly have an elevated orientational degree of freedom.[25]
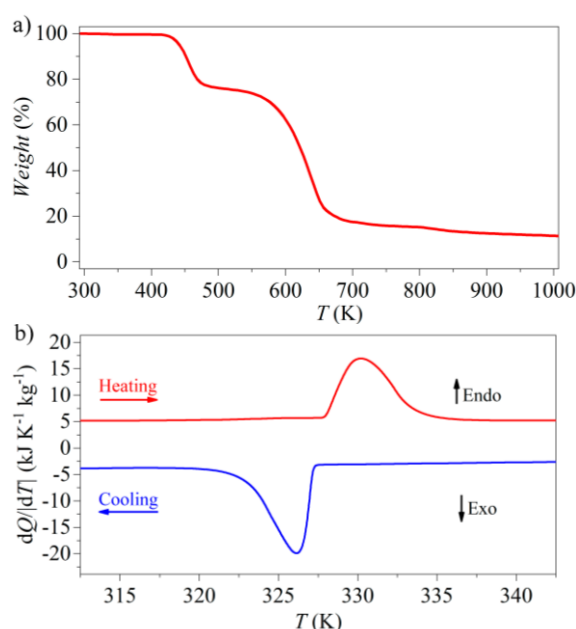
Figure 5-2. (a) Weight in percentage as function of temperature of the thermogravimetric analysis. (b) Heat flow $dQ/|dT|$ as a function of temperature T, at atmospheric pressure on heating and cooling. Endothermic and exothermic peaks are indicated.

5.3.2 Variable-temperature synchrotron radiation X-ray powder diffraction

In order to obtain detailed information of the temperature evolution of the crystal structure, the synchrotron radiation X-ray powder diffraction (SR-XRPD) patterns were measured from ~200 to ~370 K (see Fig. 5-3). There is a clear and drastic change in the SR-XRPD patterns between 325.8 and 332.1 K, taking approximately 60 seconds to complete with a heating rate of 6 K min^{-1}. This change represents the phase transition in agreement with the DSC results.
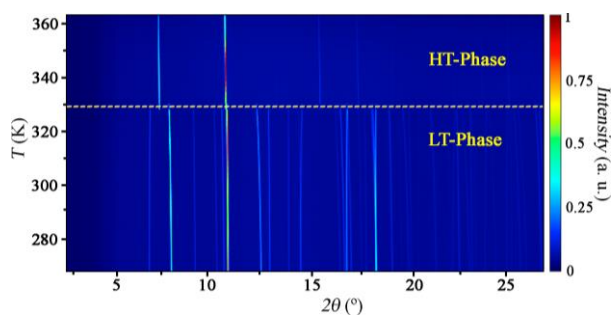
Figure 5-3. Evolution of the synchrotron radiation X-ray powder diffraction patterns (color) of $[(CH_3)_3(CH_2Cl)N]GaCl_4$ with the temperature on heating.

The Le Bail refinement of the obtained SR-XRPD patterns allows to confirm the lattice parameters and space groups of both low-temperature (LT) phase and high-temperature (HT) phase. The refinements reveal that $[(CH_3)_3(CH_2Cl)N]GaCl_4$ crystallizes in a monoclinic phase (space group Cm) below T < 330 K (see Fig. 5-4a) and the cell parameters are $a = 13.1711(2)$ Å, $b = 14.64770(7)$ Å, $c = 6.57568(6)$ Å and $\beta = 98.3683(5)$ ° at 328 K. The compound crystallizes in a cubic phase (space group $Pm\bar{3}m$) for T > 330 K (see Fig. 5-4b) and the cell parameters are $a = 6.92866(4)$ Å at 334 K. These values are very similar to those reported in literature[25] for $[(CH_3)_3(CH_2Cl)N]FeCl_4$, which shares the same symmetries and also undergoes a crystal-to-plastic-crystal phase transition.
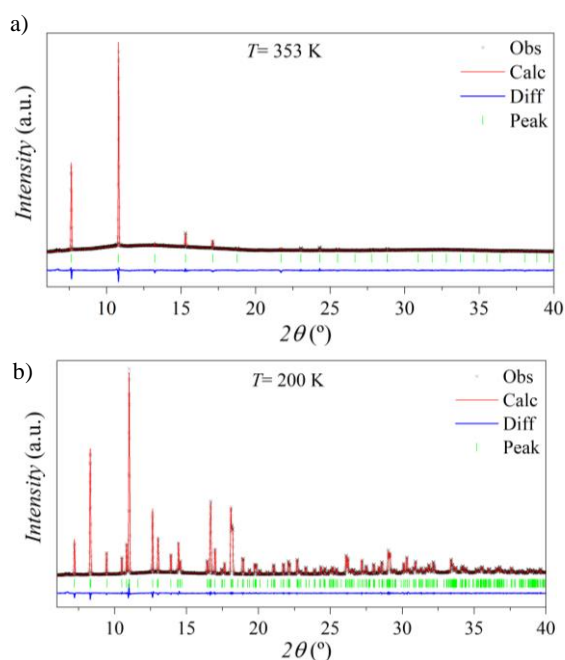

Figure 5-4. (a) Le Bail refinement of LT phase of $[(CH_3)_3(CH_2Cl)N]GaCl_4$. (b) Le Bail refinement of HT phase of $[(CH_3)_3(CH_2Cl)N]GaCl_4$.

In addition, the lattice parameters and volume of both phases were estimated as a function of temperature (see Fig. 5-5). Very interestingly, it is observed that the LT

phase exhibits an anomalous thermal evolution of the cell parameters.

The linear (α) and volumetric (β_V) coefficients of the thermal expansion (TE) were calculated from the obtained cell parameters data, and using the web-based tool PASCal (principal axis strain calculator)[32]. The HT phase exhibits the conventional positive TE, even the obtained values are colossal $\alpha = 141$ MK^{-1} and $\beta_V = 429$ MK^{-1}. The LT phase exhibits an anomalous TE, with positive TE values along the a and c-axis and a negative TE along the b-axis $\alpha_b = -76$ MK^{-1}.
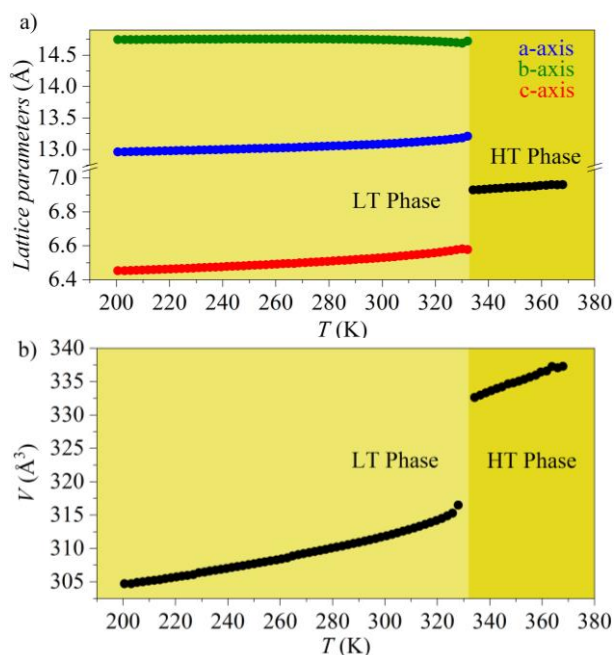
Figure 5-5. (a) Lattice parameters (a, b, and c axis) as function of temperature (T), at atmospheric pressure. (b) Cell volume (V) divided by Z as a function of T, at atmospheric pressure.

5.3.3. Thermal energy storage

The caloric parameters of this compound are very similar to those showed by other halometallates such as $[(CH_3)_3S]FeCl_4$[30] and $[(CH_3)_3(CH_2Cl)N]FeCl_4$[25] which were reported as promising compounds for thermal energy storage (TES). Then, it was decided to study $[(CH_3)_3(CH_2Cl)N]GaCl_4$ for this application. Taking into account the temperature of phase transition ($T = 326-330$ K), $[(CH_3)_3(CH_2Cl)N]GaCl_4$ has suitable operational temperatures for solar energy storage applications.[33]
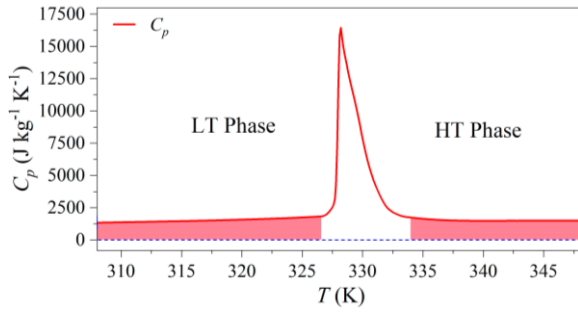
Figure 5-6. Specific heat capacity (C_p) as a function of temperature (T) on heating. Shaded area represents the TES capacity corresponding to C_p.

For TES with phase change materials, there is an additional contribution of the sensible heat in the temperatures under and above the phase transition.[13] It must be considered when calculating the TES capacity, E, which relates the operational temperatures (T_1 and T_2) with the latent heat (ΔH) of the phase transitions, the specific heat capacity before and after the phase transition temperature (T_t) and the mass of the heat storage medium (m). E was calculated using the equation 2:

$$E = m \left\{ \left[\int_{T_1}^{T_t} C_p^{LT} dT \right] + \Delta H + \left[\int_{T_t}^{T_2} C_p^{HT} dT \right] \right\} \quad (2)$$

In this context, the specific heat capacity C_p was measured as a function of temperature on heating (see Fig. 5-6), obtaining a value under the phase transition of $C_p^{LT} = 1280 - 1840$ J kg^{-1} K^{-1}; and above the phase transition, $C_p^{HT} = 1495 - 1515$ J kg^{-1} K^{-1}. In the peak of the endothermic phase transition, C_p achieves a maximum value of 16.43 kJ kg^{-1} K^{-1}.

In the temperature range of 305 to 345 K (employed for solar energy storage), $[(CH_3)_3(CH_2Cl)N]GaCl_4$ has a large value of TES capacity $E \sim 100$ kJ kg^{-1}. Another advantage of $[(CH_3)_3(CH_2Cl)N]GaCl_4$ as TES material is its density, ~ 1.60 g cm^{-1}, which is considerably higher than other TES compounds of organic nature such as polyalcohols[15,16] ($\leq$ 1 g cm^{-1}) or paraffins[17] (< 1 g cm^{-1}) and even other compounds of hybrid nature, such as $[(CH_3)_3S]FeCl_4$ and $[(CH_3)_3(CH_2Cl)N]FeCl_4$.

Furthermore, $[(CH_3)_3(CH_2Cl)N]GaCl_4$ has a small volume variation across the phase transition of a $\sim 5\%$. This value is the same as the experimented by polyalcohols like neopentylglycol[21] but much lower than the showed by paraffins (12-15 %)[17]. The high density of $[(CH_3)_3(CH_2Cl)N]GaCl_4$, in addition to smaller volume variation, means a higher compactability and a better energetic harnessing of the amount of material in a TES device.

5.3.4. Barocaloric cooling

Differential scanning calorimetry analysis were carried out under heating-cooling cycles at different isobaric pressures following the quasi-direct methodology.[34] Fig. 5-7a shows a systematic shift of the transition temperature

as pressure is increased. Pressure enhances the stability of the LT phase, which has lower volume/Z and density.
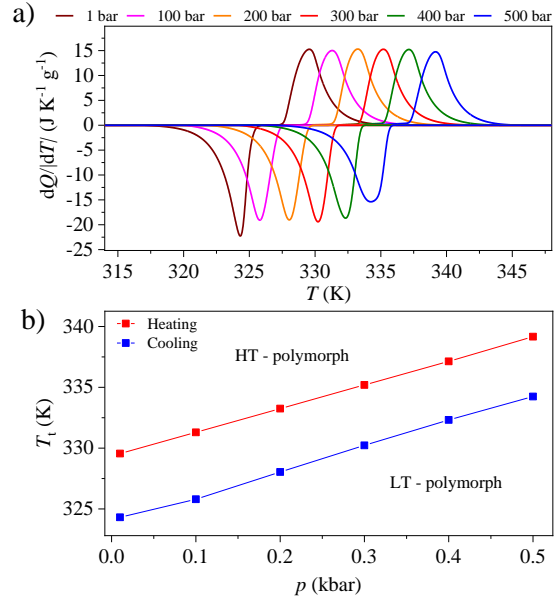
Figure 5-7. (a) Heat flow dQ/|dT| as a function of temperature, at finite applied pressures (p). (b) Transition temperatures versus pressure, identified using the peak in heat flow dQ/|dT|.

The barocaloric coefficient[35] (dT/dp) is an important barocaloric parameter, indicator of the sensitivity to pressure. It can be theoretically obtained by Clausius-Clapeyron (equation 3), where ΔV is the volume change between both phases obtained from the synchrotron data and ΔS is the entropy change in the phase transition at atmospheric pressure.

$$dT/dp = \Delta V/\Delta S \quad (3)$$

It was obtained a theoretical value of the barocaloric coefficient of ~ 26 K kbar^{-1}, which is very similar to the obtained experimental value of dT/d$p \sim 22$ K kbar^{-1}.

Additionally, it is worth to note that the obtained BC coefficient of $[(CH_3)_3(CH_2Cl)N]GaCl_4$ is very similar to those reported for related ionic plastic crystals, such as $[(CH_3)_3S]FeCl_4$ and $[(CH_3)_3(CH_2Cl)N]FeCl_4$, which exhibit a barocaloric coefficient of ~ 20 K kbar^{-1}.[36] It is also similar to the showed by hybrid perovskites, such as $[TPrA]Mn[dca]_3$ (23 K kbar^{-1})[35] and $[C_{10}H_{24}N]MnCl_4$ (21 K kbar^{-1})[37]

Isobaric entropy changes ΔS_{ib} were calculated by integrating the heat flow dQ/|dT| versus temperature curves. The results show that the value of $|\Delta S_{ib}| \sim 130$ J kg^{-1} K^{-1} at atmospheric pressure (average on heating and cooling) and decreases to ~ 125 J kg^{-1} K^{-1} at 500 bar. This decrease of $|\Delta S_{ib}|$ with applied pressure could be caused by a shrinking of the HT unit cell under the applied pressure, which provokes a decreasing of the degrees of freedom of the disordered ions. $|\Delta S_{ib}|$ is represented in Fig. 5-8 taking into account the C_p values below and above the

transition regions in order to show a more realistic behaviour considering the dependence of the volume with the temperature.
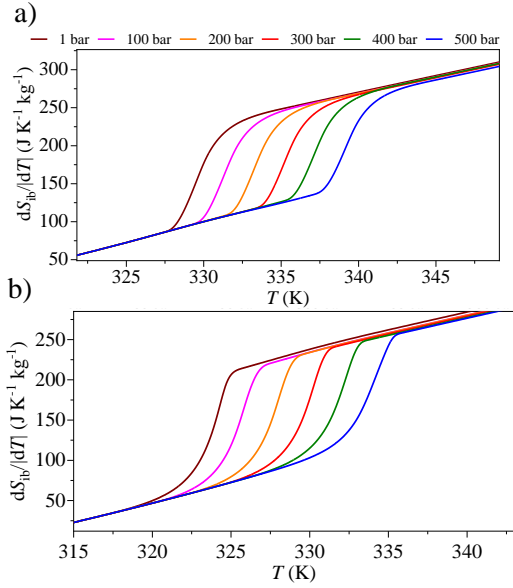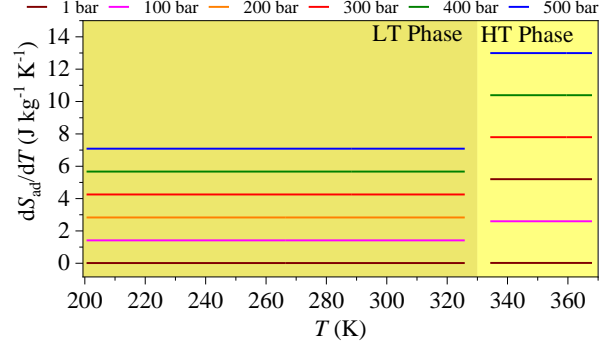

Figure 5-8. Thermally driven isobaric changes in entropy (a) on heating and (b) on cooling with respect to the LT phase for each pressure.

It must be mentioned that there are additional contributions to the entropy caused by the volumetric thermal expansion.[38] These additional entropy changes (ΔS_{ad}) were calculated taking into account the volume variation before and after the phase transition using the data obtained by synchrotron PXRD at atmospheric pressure using the equation 5:

$$\Delta S(p) = -[m^{-1} \left(\frac{\partial V}{\partial T} \right)_p]p \qquad (5)$$

The theoretical ΔS_{ad} as function of temperature is shown in Fig. 5-9. As it can be seen, for the LT phase ΔS_{ad} has a maximum value of ~7 J kg^{-1} K^{-1} at 500 bar. For the HT phase ΔS_{ad} increases up to a maximum of ~14 J kg^{-1} K^{-1} at 500 bar. This values, as expected, are a small contribution ≤ 15% of the total barocaloric effect. Furthermore, it must be noted that these values are calculated from data at atmospheric pressure and the compression effect caused by the pressure would reduce significantly this additional entropy change, so ΔS_{ad} is considerably overestimated.

After calculating the isobaric entropy changes ΔS_{ib} at each pressure, the barocaloric effect can be estimated in terms of isothermal entropy change ΔS_{it}. First, ΔS_{ib} was calculated by integrating the heat flow dQ/|dT| versus temperature curves (see Fig. 5-8). The results show that the value of |ΔS_{ib}| increases to a plateau of ~ 123 J kg^{-1} K^{-1} at atmospheric pressure and decreases to ~ 101 J kg^{-1} K^{-1} at 500 bar. This decrease of |ΔS_{ib}| with applied pressure could be caused by a shrinking of the HT unit cell under the applied pressure, which provokes a decreasing of the degrees of freedom of the disordered ions.


Figure 5-9. Additional changes in entropy at different pressures calculated from synchrotron PXRD structural data.

Then, the pressure-driven isothermal entropy changes ΔS_{it} were calculated as the difference between thermally-driven entropy changes at two different pressures (atmospheric pressure and the applied pressure) following the equation 4:

$$\Delta S_{it} = \Delta S_{ib}(p \neq 1, T) - \Delta S_{ib}(p = 1, T) \qquad (4)$$

Additional changes in entropy by the thermal expansion were added to the resulting graph of ΔS_{it}. For this purpose, it was considered the ΔS_{ad} of the LT-phase as its value was obtained on heating. The results of the sum (see Fig. 5-10) reveal colossal (≥100 J kg^{-1} K^{-1}) barocaloric effects that can be interestingly driven reversibly under the small pressure of 500 bar, ΔS_{it} ~105 J kg^{-1} K^{-1}. This value is in the same magnitude order than those reported for the ionic plastic crystals [(CH$_3$)$_3$S]FeCl$_4$ and [(CH$_3$)$_3$(CH$_2$Cl)N]FeCl$_4$ at 1000 and 800 bar, respectively.[36]
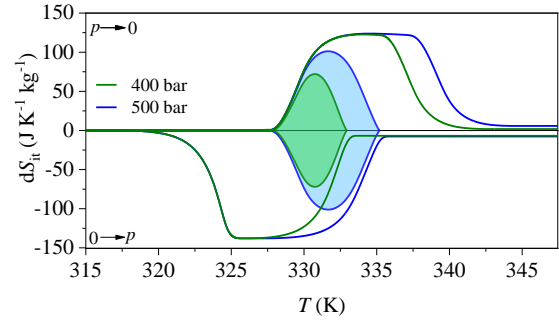
Figure 5-10. Pressure-driven isothermal entropy changes on applying ($0 \rightarrow p$) and removing ($p \rightarrow 0$) pressure. The shaded area represents the reversible barocaloric response at different pressures.

In addition to the barocaloric effect in terms of entropy, we also calculated the cooling power as the reversible adiabatic temperature change, ΔT_{rev}, achievable when pressure is applied. ΔT_{rev} (see Fig. 5-11) was obtained following the equation 6:

$$|\Delta T_{rev}(S;p_{atm} \leftrightarrow p)| = |T_C(S;p) - T_H(S;p_{atm})| \qquad (6)$$

Where $T_C(S;p)$ is each temperature of the cooling isobaric entropy change (see Fig. 5-8a) at the high pressure and

$T_H(S;p_{atm})$ is each temperature of the heating isobaric entropy change (see Fig. 5-8b) at the room pressure.

It was obtained a maximum value of ~4.2 K of temperature change on applying compression-decompression cycles of 500 bar. These value is similar to the observed in other hybrid compounds as the layered perovskites, which achieve a maximum value of ~4 K at 500 bar.[39]
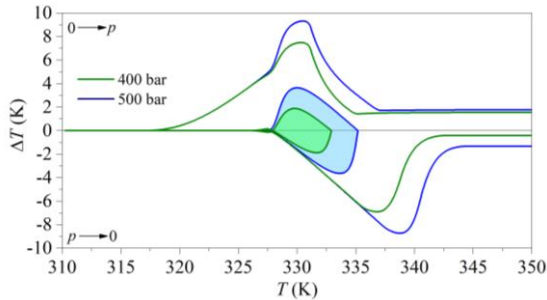
Figure 5-11. Reversible adiabatic temperature changes on applying ($0 \to p$) and removing ($p \to 0$) pressure at different pressures.

5.3.5 Dielectric switching properties

The real part of the complex dielectric permittivity (also called dielectric constant or real part of the relative permittivity, (ε_r') was measured as function of temperature under and above the phase transition temperature (see Fig. 5-12).
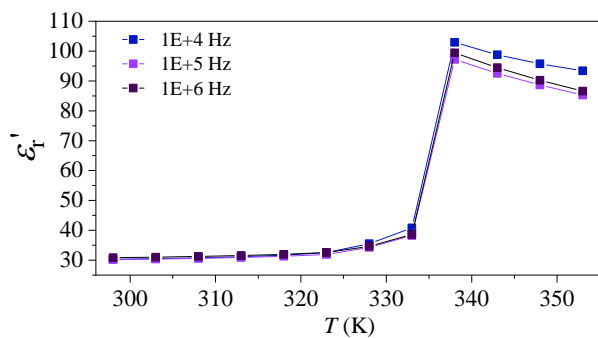
Figure 5-12. Relative permittivity (ε_r') as function of temperature measured at different frequencies.

Relative permittivity (ε_r') vs T data displays a sharp dielectric transition at $T \sim 335$ K, where the ε_r' (LT phase) values are ~30 at T ~ 320 K and the ε_r' (HT phase) values are ~100 at T ~ 340 K. This is a very large and sharp dielectric transition where the relative permittivity increases more than 3 times at dielectric transition temperature. This step-like change in the dielectric constant is consistent with a first order phase transition according to generalized Landau theory, and qualitatively resembles the dielectric behaviour of a ferroelectric-to-paraelectric transition, in other common ferroelectrics,

such as $BaTiO_3$.[40] This is consistent with the fact that the transition in $[(CH_3)_3(CH_2Cl)N]GaCl_4$ takes place between non-centrosymmetric *Cm* and paraelectric $Pm\bar{3}m$ structural phases.

Very remarkably, $[(CH_3)_3(CH_2Cl)N]GaCl_4$ shows higher values of the dielectric constant than other similar ionic PCs, such as $[(CH_3)_3S]FeCl_4$[30], which achieve a maximum value of ε_r' (HT phase) ~45; or $[(CH_3)_3(CH_2Cl)N]FeCl_4$[25], with a maximum value of ε_r' (HT phase) ~11. However, the value of ε_r' for the LT phase is considerably higher than the showed by these other plastic crystals. Two hypotheses were suggested for this. On the one hand, this could be provoked by the formation of an interphase in the electrode, that would affect to the magnitude of ε_r' but not the shape and behaviour across the phase transition, related to the intrinsic polarization of the material, which is consistent with literature.[25] On the other hand, this fact could be given by a more intense combination of polarization mechanisms because of the Ga as a substitute of Fe. A higher polarization is key to find new promising candidates for electrical energy storage in capacitors.[41] This could be related with a more polar nature of this compound given that the cation Ga^{3+} is more polarizing than Fe^{3+}. The more covalent nature of the anion $GaCl_4^-$ can provide less flexibility to the ion,[42] which can mean more intense polarization mechanisms, as it meant a more energetic phase transition than the Fe^{3+} analogue.

5.3.6. Polarization switching properties

Since the structure of $[(CH_3)_3(CH_2Cl)N]GaCl_4$ LT phase had no centre of symmetry the material was subjected to bipolar high electric field cycling in order to see if evidence of ferroelectric polarization switching could be observed. For this purpose, polarization(P)-electric(E) field hysteresis loops at 10 and 100 Hz with amplitudes from 40 to 200 kV cm^{-1} were carried out at room temperature. Fig. 5-13 shows the obtained P-E hysteresis loops. At the lowest test frequency, 10 Hz, the hysteresis loops indicate a non-ideal dielectric behaviour with contributions from electrical losses, evidenced by the oval shape (Fig. 5-13a). In such materials, poor resistivity allows mobile charge carriers to move through the material producing a leakage current which is almost indistinguishable from that produced by the electrical polarization of the material. The area inside the loop is thus, equivalent to the energy dissipated during each electric field cycle.[43,44]

The P-E loops at electric field cycles at 100 Hz show that the electrical loss is reduced consecutively with increasing frequency. This is a typical symptom for non-ideal dielectrics with leakage current contributions to the P-E loops. As a result, the remanent polarization (P_r), that is the polarization at zero electric field, also reduced as the field frequency increased and this was a symptom of the reduced electrical loss. The polarization at maximum electric field (P_{max}), however, remained consistent at approximately 0.25 µC/cm^2 for both frequencies at field

amplitude of 100 kV/cm. This suggests that this polarization response is likely representative of the material and not impacted by electrical losses.
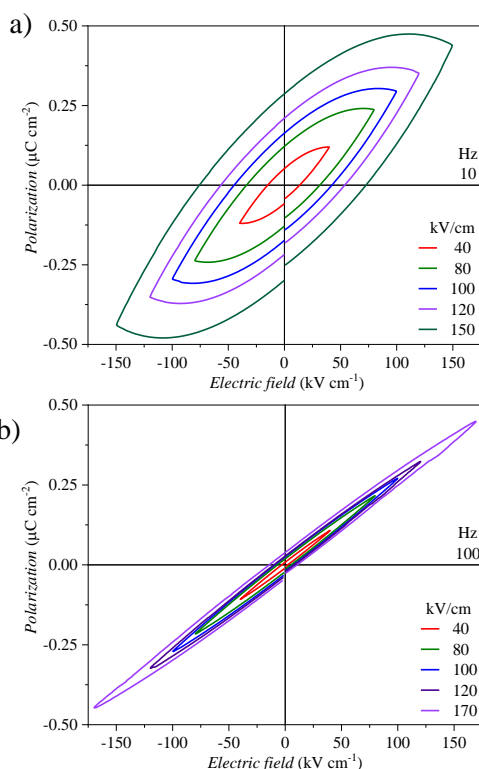
Figure 5-13. Polarization hysteresis loops at room temperature with electric field frequencies of (a) 10 Hz and (b) 100 Hz and field amplitudes between 40 and 170 kV cm^{-1}.

Despite the non-centrosymmetric structure of the material with *Cm* space group, the linear dielectric behaviour observed at frequency of 100 Hz, where the P_r was close to zero, show no evidence of ferroelectric domain switching. The P_{max} is also an order of magnitude smaller than that observed recently for some other HIPCs which suggests that contributions from ferroelectric domains is not likely.[29] This does not rule out the possibility for ferroelectric domain switching to occur in this material, but it does show that synthesis optimization to reduce leakage currents and further increases in the applied electric field are necessary to demonstrate ferroelectric domain switching.

5.4. Conclusions

Here, it is reported the synthesis of the compound [(CH$_3$)$_3$(CH$_2$Cl)N]GaCl$_4$, a novel multi-sensitive compound to different stimuli: temperature, pressure and electric field.

Given the properties shown by this compound around the phase transition provoked by temperature (high storable energy, small volume variation, high density and thermal stability, operational temperatures) it can be considered as a potential candidate for solar TES applications. It can suppose an attractive alternative to the current studied materials of organic nature, which have low density, high volume changes and low thermal stability.

In addition to this, the barocaloric behaviour of [(CH$_3$)$_3$(CH$_2$Cl)N]GaCl$_4$ was studied and reported. The interesting properties under pressure (high barocaloric coefficient, small thermal hysteresis, operational room temperature, low operational pressures and colossal barocaloric effect in terms of entropy change and adiabatic temperature variation) shown by this compound are very adequate for SSC applications. It is worth to note that it is very difficult to embrace all the ideal barocaloric properties in one single compound and even though there are other barocaloric compounds with higher entropy changes[39] or smaller operational temperatures[45]. [(CH$_3$)$_3$(CH$_2$Cl)N]GaCl$_4$ is a more equilibrated compound with similar operational pressures and higher temperature variation (which means a higher cooling power).

Also, the dielectric properties were studied. [(CH$_3$)$_3$(CH$_2$Cl)N]GaCl$_4$ has a sharp and intense dielectric transition for a hybrid plastic crystal. The finding of this behaviour in hybrid organic-inorganic plastic crystals opens the door to new studies for an interesting and more sustainable alternative to ceramic dielectric materials. Ferroelectric behaviour was not found in the conditions of the measurements. However, given the non-centrosymmetric nature of the compound, the possibility of ferroelectricity still exists. An optimization of the synthesis and modelling of the sample should be done in future research to confirm it.

As general conclusion, it was reported a multi-sensitive organic-inorganic plastic crystal. This diverse functionality, combined with remarkable caloric parameters as ecologic and more sustainable alternatives for solar TES and SSC applications encourages future studies on this promising family of solid plastic crystals.

5.5. References

1   S. Raoux, *Annu. Rev. Mater. Res.*, 2009, 39, 25–48.

2   K. Pielichowska and K. Pielichowski, *Prog. Mater. Sci.*, 2014, 65, 67–123.

3   Q. Wang, E. T. F. Rogers, B. Gholipour, C.-M. Wang, G. Yuan, J. Teng and N. I. Zheludev, *Nat. Photonics*, 2016, 10, 60–65.

4   F. Souayfane, F. Fardoun and P.-H. Biwole, *Energy Build.*, 2016, 129, 396–431.

5   S. Raoux, W. Wełnic and D. Ielmini, *Chem. Rev.*, 2010, 110, 240–267.

6   Y.-J. Jin, B. S.-I. Kim, W.-E. Lee, C.-L. Lee, H. Kim, K.-H. Song, S.-Y. Jang and G. Kwak, *NPG Asia Mater.*, 2014, 6, 137.

7   R. K. Sharma, P. Ganesan, V. V Tyagi, H. S. C. Metselaar and S. C. Sandaran, *Energy Convers. Manag.*, 2015, 95, 193–228.

8   N. Zhang, Y. Yuan, X. Cao, Y. Du, Z. Zhang and Y. Gui, *Adv. Eng. Mater.*, 2018, 20, 1700753.

9   M.-H. Kim, J. Pettersen and C. W. Bullard, *Prog. energy Combust. Sci.*, 2004, 30, 119–174.

10 EU, *Regul. No 517/2014*, 2014, 57, 216.

11 A. Fallahi, G. Guldentops, M. Tao, S. Granados-Focil and S. Van Dessel, *Appl. Therm. Eng.*, 2017, 127, 1427–1441.

12 P. Lloveras and J.-L. Tamarit, *MRS Energy Sustain.*, 2021, 1–13.

13 S. D. Sharma and K. Sagara, *Int. J. Green Energy*, 2005, 2, 1–56.

14 A. F. Regin, S. C. Solanki and J. S. Saini, *Renew. Sustain. Energy Rev.*, 2008, 12, 2438–2458.

15 K. P. Venkitaraj, S. Suresh, B. Praveen, A. Venugopal and S. C. Nair, *J. Energy Storage*, 2017, 13, 359–377.

16 S. Santos-Moreno, S. Doppiu, G. A. Lopez, N. Marinova, Á. Serrano, E. Silveira and E. Palomo del Barrio, *Materials (Basel).*, 2020, 13, 1162.

17 A. Serrano, M. Duran, J.-L. Dauvergne, S. Doppiu and E. P. Del Barrio, *Sol. Energy Mater. Sol. Cells*, 2021, 220, 110848.

18 J. Timmermans, *J. Phys. Chem. Solids*, 1961, 18, 1–8.

19 L. A. K. Staveley, *Annu. Rev. Phys. Chem.*, 1962, 13, 351–368.

20 D. Boldrin, *Appl. Phys. Lett.*, 2021, 118, 170502.

21 P. Lloveras, A. Aznar, M. Barrio, P. Negrier, C. Popescu, A. Planes, L. Mañosa, A. Avramenko, N. D. Mathur, X. Moya and J. Tamarit, *Nat. Commun.*, 2019, 10, 1803.

22 B. Li, Y. Kawakita, S. Ohira-Kawamura, T. Sugahara, H. Wang, J. Wang, Y. Chen, S. I. Kawaguchi, S. Kawaguchi, K. Ohara, K. Li, D. Yu, R. Mole, T. Hattori, T. Kikuchi, S. ichiro Yano, Z. Zhang, Z. Zhang, W. Ren, S. Lin, O. Sakata, K. Nakajima and Z. Zhang, *Nature*, 2019, 567, 506–510.

23 M. M. Umair, Y. Zhang, K. Iqbal, S. Zhang and B. Tang, *Appl. Energy*, 2019, 235, 846–873.

24 A. Aznar, P. Lloveras, M. Barrio, P. Negrier, A. Planes, L. Mañosa, N. Mathur, X. Moya and J. L. Tamarit, *J. Mater. Chem. A*, 2019, 8, 639–647.

25 D. Li, X. M. Zhao, H. X. Zhao, L. S. Long and L. S. Zheng, *Inorg. Chem.*, 2019, 58, 655–662.

26 J. Salgado-Beceiro, S. Castro-García, M. Sánchez-Andújar and F. Rivadulla, *J. Phys. Chem. C*, 2018, 122, 27769–27774.

27 P. Gonzalez-Izquierdo, O. Fabelo, L. Canadillas-Delgado, G. Beobide, O. Vallcorba, J. Salgado-Beceiro, M. Sánchez-Andújar, C. Martin Gandul, J. Ruiz-Fuertes, J. E. Garcia, M. T. Fernandez-Diaz and M. de Pedro, *J. Mater. Chem. C*, 2021, 9, 4453–4465.

28 J. Walker, R. Miranti, S. L. Skjærvø, T. Rojac, T. Grande and M. A. Einarsrud, *J. Mater. Chem. C*, 2020, 8, 3206–3216.

29 J. Harada, N. Yoneyama, S. Yokokura, Y. Takahashi, A. Miura, N. Kitamura and T. Inabe, *J. Am. Chem. Soc.*, 2018, 140, 346–354.

30 J. Salgado-Beceiro, J. M. Bermúdez-García, A. L. Llamas-Saiz, S. Castro-García, M. A. Señarís-Rodríguez, F. Rivadulla and M. Sánchez-Andújar, *J. Mater. Chem. C*, 2020, 8, 13686–13694.

31 B. H. Toby and R. B. Von Dreele, *J. Appl. Crystallogr.*, 2013, 46, 544–549.

32 PASCal, http://pascal.chem.ox.ac.uk/, (accessed 3 August 2021).

33 M. M. Farid, A. M. Khudhair, S. Ali and K. Razack, 2004, 45, 1597–1615.

34 X. Moya, S. Kar-Narayan and N. D. Mathur, *Nat. Mater.*, 2014, 13, 439–450.

35 J. M. Bermúdez-García, M. Sánchez-Andújar, S. Castro-García, J. López-Beceiro, R. Artiaga and M. A. Señarís-Rodríguez, *Nat. Commun.*, 2017, 8, 15715.

36 J. Salgado-Beceiro, J. M. Bermudez-García, E. Stern-Taulats, J. García-Ben, S. Castro-García, M. Sanchez-Andujar, X. Moya and M. A. Señarís-Rodríguez, *ChemRxiv*.

37 J. Mason, J. Seo, R. McGillicuddy, A. Slavney, S. Zhang, A. Yakovenko and S.-L. Zheng, *Nat. Portf.*

38 P. Lloveras, E. Stern-Taulats, M. Barrio, J. L. Tamarit, S. Crossley, W. Li, V. Pomjakushin, A. Planes, L. Mañosa, N. D. Mathur and X. Moya, *Nat. Commun.*, 2015, 6, 8801.

39 J. Li, M. Barrio, D. J. Dunstan, R. Dixey, X. Lou, J. Tamarit, A. E. Phillips and P. Lloveras, *Adv. Funct. Mater.*, 2021, 2105154.

40 M. E. Lines and A. M. Glass, *Principles and Applications of Ferroelectrics and Related Materials*, Oxford University Press, Oxford, 2001.

41 S. Bonardd, V. Moreno-Serna, G. Kortaberria, D. Díaz Díaz, A. Leiva and C. Saldías, *Polym.*, 2019, 11.

42 J. Binns, G. J. McIntyre, J. A. Barreda-Argüeso, J. González, F. Aguado, F. Rodríguez, R. Valiente and S. Parsons, *Acta Crystallogr. Sect. B Struct. Sci. Cryst. Eng. Mater.*, 2017, 73, 844–855.

43   H. Yan, F. Inam, G. Viola, H. Ning, H. Zhang, Q. Jiang, T. A. O. Zeng, Z. Gao and M. J. Reece, *J. Adv. Dielectr.*, 2011, 1, 107–118.

44   L. Jin, F. Li and S. Zhang, *J. Am. Ceram. Soc.*, 2014, 97, 1–27.

45   A. Aznar, P. Negrier, A. Planes, L. Mañosa, E. Stern-Taulats, X. Moya, M. Barrio, J.-L. Tamarit and P. Lloveras, *Appl. Mater. Today*, 2021, 23, 101023.

Chapter 6

Chapter 6

General conclusions

This doctoral thesis is focused on the search of *hybrid organic-inorganic materials* with *phase transitions* that make them suitable for *solid-state cooling (SSC)* and *solar thermal energy storage (TES)* applications. The synthesis, characterization and study of the properties of some selected compounds within this vast *hybrid organic-inorganic* family was carried out.

Chapter 2 consists of a study of the barocaloric properties of the hybrid perovskite $[(CH_3)_4N]Mn(N_3)_3$ for solid-state cooling. The giant barocaloric effect of the compound along its first-order structural transition from a cubic to a monoclinic phase at 305 K (heating) is reported. At ambient pressure, the transition exhibits a large entropy change of ~80 J kg-1 K-1 and a small thermal hysteresis of ~7 K, in addition to a volume change of ~1.5%. When pressure is applied near room temperature, the transition exhibits an entropy change of ~70 J kg-1 K-1, representing **a giant barocaloric response of the hybrid perovskite $[(CH_3)_4N]Mn(N_3)_3$**.

In Chapter 3 we report the synthesis and characterization of a new compound, $[(CH_3)_3S]FeCl_4$, a plastic crystal with multiple functional properties. The compound undergoes a first-order transition near room temperature with a high latent heat of ~40 kJ kg^{-1} and energy charge and discharge temperatures of 315 K and 302 K (respectively), well suited for solar thermal energy storage. In addition, dielectric properties, magnetization and electron spin resonance studies reveal that the material exhibits multifunctional properties with temperature-induced reversible changes in its dielectric, conductive and magnetic behavior associated with the phase transition. Furthermore, the dielectric permittivity increases dramatically up to 5-fold when the phase transition is induced, which could be exploited to store electrical energy in a capacitor. Therefore, it is reported that **$[(CH_3)_3S]FeCl_4$ is a very interesting new material with the coexistence of multi-functional properties that can be useful for both solar thermal and electrical energy storage.**

Chapter 4 consists of a barocaloric study of the new plastic crystal $[(CH_3)_3S]FeCl_4$ (characterized in the previous chapter) and $[(CH_3)_3(CH_2Cl)N]FeCl_4$ (chosen for the intense phase transition it exhibits). This represents the introduction of a new family of barocaloric materials: organic-inorganic hybrid plastic crystals. Calorimetric studies reveal large barocaloric effects of similar magnitude to those of other organic plastic crystals ($\Delta S > 100$ J K^{-1} kg^{-1}) near room temperature and under pressures below 1000 bar, leading to enhanced barocaloric strength. **These hybrid plastic crystals $[(CH_3)_3S]FeCl_4$ and $[(CH_3)_3(CH_2Cl)N]FeCl_4$ emerge as strong candidates as barocaloric materials to be used in solid-state cooling systems.**

In Chapter 5, extensive studies of the new plastic crystal $[(CH_3)_3(CH_2Cl)N]GaCl_4$ are carried out. This new compound presents a phase transition to plastic crystal at 330 K heating, with a 4 K hysteresis, with an associated latent heat of ~44 kJ kg^{-1}. These parameters, among others, make this hybrid material very interesting for solar thermal energy storage applications. In addition, the material exhibits a barocaloric effect of ~105 J kg^{-1} K^{-1} at 500 bar, which is very attractive for solid-state cooling applications. This compound also exhibits a dielectric transition as a function of temperature, increasing its dielectric constant 3 times above the transition temperature. The combination of properties offered by this hybrid plastic crystal implies that **the hybrid plastic crystal $[(CH_3)_3(CH_2Cl)N]GaCl_4$ is a new multi-sensitive material with multi-functional properties for energy applications.**

Table 6-1. Selected barocaloric parameters of the compounds reported in this thesis (yellow) in comparison with the most relevant barocaloric materials reported since the beggining of this research; the compounds are listed by date of report. T_h = transition temperature on heating; T_c = transition temperature on cooling; dT/dp = average barocaloric coefficient; $|\Delta S_{rev}|$ = reversible barocaloric effects obtained from quasi-direct methods; Δp = applied pressure required to induce the reversible barocaloric effect; $|\Delta S_{rev}|/\Delta p$ = barocaloric strength; T_{op} = operating temperature range at 1 kbar (for those compounds which were not studied at 1 kbar we suggest an approximation of a longer ranger than the reported at their pressure for reversibility); bntrz = 4-(benzyl)-1,2,4-triazole and tcnset = 1,1,3,3-tetracyano-2-thioethylepropenide; TPrA = tetrapropylammonium, dca = dicyanamide.

Compound	Date (mm/y y)	T_h (K)	T_c (K)	dT/dp (K kbar^{-1})	$|\Delta S_{rev}|$ (J K^{-1} kg^{-1})	Δp (bar)	$|\Delta S_{rev}|/\Delta p$ (J K^{-1} kg^{-1} kbar^{-1})	T_{op} at 1 kbar (K)
[TPrA]Mn[dca]$_3$ [1]	06/17	330	329	23.1	37.0	70	529	330 – 352 (22 K)
[TPrA]Cd[dca]$_3$ [2]	08/18	386	385	38.2	11.5	70	164	386 - 423 (37 K)
(CH$_3$)$_2$C(CH$_2$OH)$_2$ [3] (NPG)	04/19	311	296	10.3	445	2500	178	-
(CH$_3$)C(CH$_2$OH)$_3$ [4] (PG)	11/19	354	350	8.7	490	2400	204	354 – 359 (5 K)
(CH$_3$)$_3$C(CH$_2$OH) [4] (NPA)	11/19	231	211	17	290	2600	112	-
Fullerite C$_{60}$ [5]	07/20	257	254	17	25	1000	25	257 - 271 (14 K)
[(CH$_3$)$_4$N]Mn[N$_3$]$_3$ Chapter 2	09/20	305	298	12	70	900	78	305 – 310 (5 K)
Fe$_3$(bntrz)$_6$(tcnset)$_6$ [6]	02/21	318	316	25	80	550	145	316 - >326 (>10 K)
Br-Adamantane [7]	06/21	316	308	35	134	1000	134	316 - 343 (27 K)
Cl-Adamantane [7]	06/21	254	245	27	153	1000	153	254 - 272 (18 K)
[(CH$_3$)$_3$(ClCH$_2$)N]FeCl$_4$ Chapter 4	07/21	326	322	19.7	123	800	154	326 - 342 (16 K)
[(CH$_3$)$_3$S]FeCl$_4$ Chapter 4	07/21	315	302	19.9	125	1000	125	315 – 322 (7 K)
[(CH$_3$)$_3$(ClCH$_2$)N]GaCl$_4$ Chapter 5	08/21	330	326	20.0	105	500	210	328 – >337 (>9 K)
[C$_{10}$H$_{21}$NH$_3$]$_2$MnCl$_4$ [8]	08/21	312	303	26.5	230	500	460	305 – >326 (21 K)
[C$_{10}$H$_{24}$N]MnCl$_4$ [9]	08/21	310	307	21	75	150	500	306 – >311 (>5 K)
[C$_9$H$_{22}$N]CuBr$_4$ [9]	08/21	305	304	27	68	150	453	301 – >308 (>7 K)
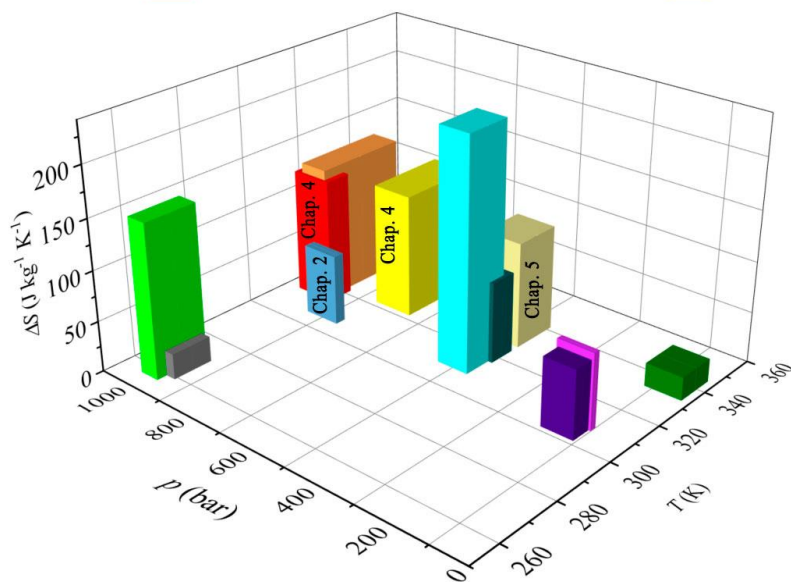
Figure 6-1. Operational temperature (thermal span), operational pressure and isothermal entropy change for different barocaloric materials from Table 6-1. The ideal region for commertial applications is shaded in red at low pressure and room temperature. The corresponding chapters of the materials studied in this thesis are indicated in the graph as Chapt. 2, 4 and 6.

References

1   J. M. Bermúdez-García, M. Sánchez-Andújar, S. Castro-García, J. López-Beceiro, R. Artiaga and M. A. Señarís-Rodríguez, *Nat. Commun.*, 2017, **8**, 15715.

2   J. M. Bermúdez-García, S. Yáñez-Vilar, A. García-Fernández, M. Sánchez-Andújar, S. Castro-García, J. López-Beceiro, R. Artiaga, M. Dilshad, X. Moya and M. A. Señarís-Rodríguez, *J. Mater. Chem. C*, 2018, **6**, 9867–9874.

3   P. Lloveras, A. Aznar, M. Barrio, P. Negrier, C. Popescu, A. Planes, L. Mañosa, A. Avramenko, N. D. Mathur, X. Moya and J. Tamarit, *Nat. Commun.*, 2019, **10**, 1803.

4   A. Aznar, P. Lloveras, M. Barrio, P. Negrier, A. Planes, L. Mañosa, N. Mathur, X. Moya and J. L. Tamarit, *J. Mater. Chem. A*, 2019, **8**, 639–647.

5   J. Li, D. Dunstan, X. Lou, A. Planes, L. Mañosa, M. Barrio, J.-L. Tamarit and P. Lloveras, *J. Mater. Chem. A*, 2020, **8**, 20354–20362.

6   M. Romanini, Y. Wang, K. Gürpinar, G. Ornelas, P. Lloveras, Y. Zhang, W. Zheng, M. Barrio, A. Aznar and A. Gràcia-Condal, *Adv. Mater.*, 2021, **33**, 2008076.

7   A. Aznar, P. Negrier, A. Planes, L. Mañosa, E. Stern-Taulats, X. Moya, M. Barrio, J.-L. Tamarit and P. Lloveras, *Appl. Mater. Today*, 2021, **23**, 101023.

8   J. Li, M. Barrio, D. J. Dunstan, R. Dixey, X. Lou, J. Tamarit, A. E. Phillips and P. Lloveras, *Adv. Funct. Mater.*, 2021, 2105154.

9   J. Mason, J. Seo, R. McGillicuddy, A. Slavney, S. Zhang, A. Yakovenko and S.-L. Zheng, *Nat. Portf.*

Annexes

Spanish Summary   Patents

Publications

Communications

Collaborations

Annexe I

Spanish summary | Resumen en español

Hay una evidencia innegable de que el modo de vida de nuestra sociedad, especialmente durante el último siglo, está teniendo un impacto considerable en el planeta en el que vivimos. Muchos de los cambios que estamos viendo en la atmósfera están directamente relacionados con el uso de la energía por parte de la sociedad. Sin embargo, el problema no parece ser solo el uso de la energía, sino también los sistemas empleados para generarla y almacenarla. Recientemente, la Agencia Internacional de la Energía ha señalado a los sistemas de calentamiento y enfriamiento como los responsables del ~40% y ~8% (respectivamente) de las emisiones globales de CO_2. El control de temperatura es siempre uno de los retos más importantes en muchas de las actividades tecnológicas. Un ejemplo reciente de esto es la batalla comercial por la vacuna contra el COVID-19, cuya cadena de frío representa alrededor del 80% del coste total del sistema de vacunación.

En general, la demanda global de **calefacción, ventilación, aire acondicionado y refrigeración** (CVACR) en asentamientos residenciales e industriales está creciendo rápidamente. La mayoría de estos sistemas utilizan tecnologías como resistencias eléctricas, combustión de gases o compresión de vapor. Las resistencias eléctricas son muy caras; y la combustión y compresión de gases suponen el uso de gases de efecto invernadero, tóxicos y/o inflamables cuya fuga supone un alto riesgo y un problema de seguridad para el usuario y el medio ambiente. En este contexto, la Agencia Internacional de la Energía ha publicado recientemente que los sistemas energéticos renovables (considerando calefacción y refrigeración) pueden suponer una reducción del ~90% de las emisiones de CO_2 relacionadas con la energía para el año 2050.

En los últimos años, los **materiales con cambios de fase sólido-sólido** (MCF-SS) han sido estudiados como una alternativa ecológica para la conversión y/o almacenamiento de energía en sistemas de CVACR. Los MCF-SS son compuestos que presentan transiciones de fase reversibles desde una fase en estado sólido a otra fase sólida diferente, inducidas por un estímulo externo (temperatura, presión, campo eléctrico y/o magnético). Estas transiciones de fase conllevan cambios térmicos que se pueden emplear en refrigeración, calefacción o almacenamiento térmico de energía.

La tecnología que utiliza MCF-SS para refrigeración se conoce comúnmente como **enfriamiento en estado sólido** y el proceso es similar al empleado en la compresión de vapor con materiales barocalóricos (aquellos que presentan transiciones de fase inducidas por presión). En una descripción esquemática de un ciclo de enfriamiento, cuando se aplica presión a un material, este sufre una transición de fase, liberando calor al medio (esto sería la parte trasera de una nevera, por ejemplo). Cuando se retira la presión, el material se vuelve de nuevo a la fase sólida inicial, absorbiendo calor del medio (este proceso ocurriría dentro de la nevera). Hoy en día, la mayoría de sistemas de refrigeración funcionan con transiciones de fase de gas a líquido, utilizando gases con un elevado número de problemas, como la contribución al efecto invernadero, toxicidad o inflamabilidad. La alternativa de trabajar con sólidos eliminaría estas desventajas, lo que hace que resulte una alternativa muy prometedora.

Por otro lado, la tecnología empleada para almacenar energía mediante MCF-SS se conoce como **almacenamiento de energía térmica** (AET). En esta tecnología, el calor latente asociado a una transición de fase se absorbe (carga) o se libera (descarga) cuando la temperatura aumenta o disminuye a lo largo de la temperatura de transición del material. Cuando la temperatura externa aumenta, el compuesto sufre una transición de fase, absorbiendo calor y enfriando el sistema.

Mientras la temperatura se mantiene por encima del punto de transición, la enrgía permanece almacenada. Cuando la temperatura exterior disminuye, el material vuelve a la fase inicial, liberando la energía almacenada y calentando el medio. El AET resulta muy atractivo para su uso en edificios porque la temperatura del interior puede ser regulada por las variaciones térmicas naturales del exterior. Sin embargo, en la actualidad, la mayoría de sistemas de AET funcionan con cambios de fase que parten de un estado líquido, lo que conlleva ciertos problemas, como riesgos de fugas y una mayor dificultad al operar con compuestos, así como una mayor complicación de almacenamiento debido a los grandes cambios de volumen. Una de las aplicaciones más ecológicas y sostenible del AET es aquella que utiliza los cambios de temperatura provocados por la energía solar, que es denominada AET solar.

En este contexto, se ha remarcado la importancia de estudiar MCF-SS en mayor profundidad, tanto sus propiedades físico-químicas como funcionales. Hasta la fecha, los materiales más estudiados para aplicaciones en CVACR son de naturaleza orgánica. Sin embargo, los materiales orgánicos que han demostrado tener propiedades adecuadas para aplicaciones energéticas presentan ciertas desventajas, como bajas temperaturas de descomposición, inflamabilidad o baja reversibilidad para aplicaciones de refrigeración. Estos problemas pueden solucionarse mediante la combinación de partes orgánicas e inorgánicas en los llamados materiales híbridos orgánicos-inorgánicos. La presencia de unidades inorgánicas, como metales de transición, puede dar una mayor estabilidad térmica y proporcionar nuevas propiedades funcionaes (dieléctricas, magnéticas, ópticas, etc.). De forma interesante, estas propiedades pueden combinarse en materiales multi-sensitivos, dotando a estos compuestos de multi-funcionalidad para un amplio rango de aplicaciones.

¿Y por dónde empezar?

El grupo de investigación **UDCSolids,** sección del grupo QUIMOLMAT, de la **Universidade da Coruña**, donde se llevó a cabo esta tesis doctoral, tiene una amplia experiencia en la química de estado sólido y materiales, con décadas de experiencia en el estudio de materiales basados en la estructura de perovskita, tanto las de sólidos metálicos como las híbridas orgánicas-inorgánicas. Éstas últimas perovskitas híbridas, con fórmula general ABX_3, combinan moléculas orgánicas (parte A) con átomos metálicos (parte B) unidos mediante ligandos orgánicos o inorgánicos (parte X). Justo antes de que esta tesis comenzase, el grupo descubrió la primera perovskita híbrida barocalórica, $[TPrA][Mn(dca)_3]$ (TPrA: tetra-propylamonio, dca: dicianamida), y publicó el gran potencial de esta familia de compuestos para la refrigeración en estado sólido.

En este contexto, la presente tesis doctoral se comenzó estudiando las propiedades barocalóricas de perovskitas híbridas como **primer objetivo**.

Durante el progreso de nuestras investigaciones, otros compuestos fueron publicados por otros grupos con interesantes propiedades barocalóricas: los llamados cristales plásticos (CP) orgánicos, como el neopentilglicol. Los PC son un grupo de compuestos caracterizados por experimentar transiciones de fase de un estado sólido a un estado de CP antes de fundir, manteniendo la cristalinidad, aunque con grados de libertad orientacional y conformacional. Entonces, aprovechando la experiencia de nuestro grupo en materiales híbridos, se decidió estudiar el efecto barocalórico de PC híbridos orgánicos-inorgánicos (formados por cationes orgánicos y aniones inorgánicos), que nunca habían sido investigados para refrigeración en estado sólido, lo que se propuso como **segundo objetivo** de tesis.

Además, los PC híbridos fueron recientemente reportados como materiales potenciales para AET debido a las energéticas transiciones de fase que experimentan. Por otra parte, la presencia de átomos metálicos siempre puede dotarlos de propiedades funcionales como dieléctricas, ferroeléctricas y/o magnéticas. Por lo tanto, como **tercer objetivo** de tesis, los CP híbridos fueron

estudiados para aplicaciones de AET, incluyendo el análisis de propiedades funcionales adicionales como dieléctricas, ferroeléctricas y magnéticas.

Con esta base, el principal objetivo de la presente tesis doctoral puede resumirse como el diseño, síntesis y caracterización de **materiales híbridos orgánicos-inorgánicos con transiciones de fase para refrigeración en estado sólido y aplicaciones de almacenamiento de energía térmica solar**. La memoria de este trabajo fue organizada teniendo en cuenta los resultados obtenidos para los objetivos marcados en el siguiente orden:

El **capítulo 1** contiene una introducción de toda la temática tratada en la tesis. Se describe un estado del arte de la refrigeración y el almacenamiento de energía, entrando más en detalle en el enfriamiento en estado sólido y el almacenamiento de energía térmica solar, además de la posible combinación con propiedades dieléctricas. Se hace una descripción y clasificación de las transiciones de fase, fenómeno responsable de las aplicaciones propuestas. En la última sección de la introducción se tratan y clasifican las dos familias de materials estudiadas en la tesis: perovskitas híbridas y cristales plásticos híbridos.

Los capítulos 2, 3 y 4 se presentan como publicaciones de los trabajos reportados. El capítulo 5 tiene el mismo formato, aunque todavía no se ha publicado.

El **capítulo 2** consiste en un estudio de las propiedades barocalóricas de la perovskita híbrida $[(CH_3)_4N]Mn(N_3)_3$ para refrigeración en estado sólido. Se reporta el efecto barocalórico gigante del compuesto a lo largo de su transición estructural de primer orden de una fase cúbica a monoclínica a 305 K (calentando). A presión ambiente, la transición presenta un gran cambio de entropía de ~80 J kg^{-1} K^{-1} y una pequeña histéresis térmica de ~7 K, además de un cambio de volumen de ~1.5%. Al aplicar presión cerca de temperatura ambiente, la transición presenta un cambio de entropía de ~70 J kg^{-1} K^{-1}, lo que representa una respuesta barocalórica gigante.

En el **capítulo 3** se comienzan a estudiar los cristales plásticos híbridos. En este capítulo se reporta la síntesis y caracterización de un nuevo compuesto, $[(CH_3)_3S]FeCl_4$, un cristal plástico con múltiples propiedades funcionales. El compuesto experimenta una transición de primer orden cercana a temperatura ambiente con un alto calor latente de ~40 kJ kg^{-1} y unas temperaturas de carga y descarga de energía de 315 K y 302 K (respectivamente), muy apropiadas para almacenamiento de energía térmica solar. Además, los estudios de propiedades dieléctricas, magnetización y resonancia de spin electrónico revelan que el material presenta propiedades multifuncionales con cambios reversibles inducidos por temperatura en su comportamiento dieléctrico, conductor y magnético asociado con la transición de fase. Además, la permitividad dieléctrica aumenta drásticamente hasta 5 veces cuando se induce la transición de fase, lo que podría se explotado para almacenar energía eléctrica en un capacitor. Por lo tanto, se reporta que el compuesto $[(CH_3)_3S]FeCl_4$ es un material muy interesante con la coexistencia de propiedades multi-funcionales que pueden ser útiles tanto para almacenamiento de energía térmica solar como de energía eléctrica.

El **capítulo 4** consta de un estudio barocalórico de dos cristales plásticos: $[(CH_3)_3S]FeCl_4$ (caracterizado en el capítulo anterior) y $[(CH_3)_3(CH_2Cl)N]FeCl_4$ (escogido por la intensa transición de fase que presenta). Este capítulo supone la introducción de una nueva familia de materiales barocalóricos: los cristales plásticos híbridos orgánicos-inorgánicos. Los materiales aquí reportados presentan una estructura compuesta por aniones ionrgánicos y cationes orgánicos con interacciones electrostáticas débiles. Los estudios calorimétricos revelan grandes efectos barocalóricos de similar magnitud a otros cristales plásticos orgánicos ($\Delta S > 100$ J K^{-1} kg^{-1}) cerca de temperatura ambiente y bajo presiones inferiores a 1000 bar, lo que lleva a una mayor fuerza

barocalórica. Esto es de gran interés desde que los materiales barocalóricos se han propuesto como fuertes candidatos como la alternativa a los actuales sistemas de refrigeración.

En el **capítulo 5** se lleva a cabo un estudio más amplio sobre el nuevo cristal plástico $[(CH_3)_3(CH_2Cl)N]GaCl_4$. En este capítulo se analizan las propiedades térmicas del compuesto para aplicaciones de almacenamiento de energía térmica solar; se hace un estudio barocalórico del material enfocado a aplicaciones de refrigeración en estado sólido; y, además, se analizan las propiedades dieléctricas y de polarización frente a campo eléctrico del material. Este nuevo compuesto presenta una transición de fase a cristal plástico a 330 K calentando, con 4 K de histéresis, con un calor latente asociado de ~44 kJ kg^{-1}. Estos parámetros, entre otros, hacen muy interesante a este compuesto para aplicaciones de almacenamiento de energía térmica solar. Además, el material presenta un efecto barocalórico de ~105 J kg^{-1} K^{-1} a 500 bar, lo que supone unos valores muy atractivos para aplicaciones de refrigeración en estado sólido. Por otro lado, el compuesto presenta también una transición dieléctrica en función de la temperatura, incrementando su constante dieléctrica 3 veces. La combinación de propiedades ofrecida por este cristal plástico híbrido implica que el $[(CH_3)_3(CH_2Cl)N]GaCl_4$ es un material multi-sensible con propiedades multi-funcionales para aplicaciones energéticas.

El **capítulo 6** consta de las conclusiones generales de la tesis. Cuenta, además, con una comparativa de los materiales barocalóricos más relevantes que se han publicado paralelamente a esta tesis durante los años de su realización. La gran actividad del campo de materiales barocalóricos implicó que la posición de los materiales aquí mostrados respecto a los materiales con un mejor efecto barocalórico a las condiciones más ideales fuse variando; por ello se consideró relevante hacer un análisis comparativo de los principales parámetros de los materiales reportados en esta tesis con los publicados en otros estudios.

Finalmente, se incluyen dos anexos con información relevante añadida:

El **Anexo I** es el presente y consta de un resumen de toda la tesis en castellano.

El **Anexo II** contiene las patentes, publicaciones en revistas científicas, comunicaciones en eventos especializados y colaboraciones realizadas por el doctorando Jorge Salgado Beceiro en el periodo de realización de la presente tesis doctoral.

Annexe II

1. Patents

Título: **Proceso y dispositivo de refrigeración/calefacción basados en compuestos híbridos orgánico-inorgánicos moleculares.**

Title: **Process and device for cooling/heating based on hybrid organic-inorganic hybrid molecular compounds.**

Número de solicitud | Application number: **P202130565**

Fecha de recepción | Reception date: **17/06/2021**

Authors: **Salgado-Beceiro, J.**; Bermúdez-García, J. M.; García-Ben, J.; Sánchez-Andújar, M.; Castro-García, S.; Señarís-Rodríguez, M. A.; Stern-Taulats, E.; Moya, X.
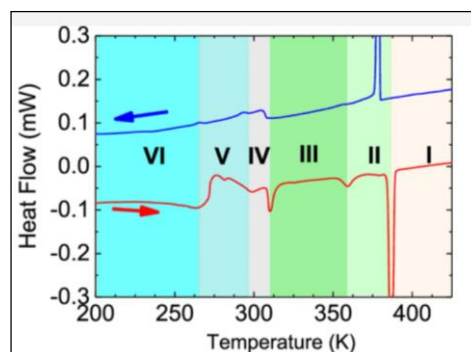
2. Publications

Title: **Motional Narrowing of Electron Spin Resonance Absorption in the Plastic-Crystal Phase of [(CH$_3$)$_4$N]FeCl$_4$.**

Authors: **Salgado-Beceiro, J.**; Castro-García, S.; Sánchez-Andújar, M.; Rivadulla, F.

Reference: *Journal of Physiscal Chemistry C*, **2018**, 122(48), 27769-27774.

DOI: **https://doi.org/10.1021/acs.jpcc.8b09367**

Title: **Near-Room-Temperature Reversible Giant Barocaloric Effects in [(CH$_3$)$_4$N]Mn[N$_3$]$_3$ Hybrid Perovskite.**

Authors: **Salgado-Beceiro, J.**; Nonato, A.; Xavier Silva, R.; Garcia-Fernandez, A.; Sanchez-Andujar, M.; Castro-Garcia, S.; Stern-Taulats, E.; Señarís-Rodríguez, M. A.; Moya, X.; Bermudez-García, J. M.

Reference: *Materials Advances*, **2020**, 1, 3167-3170.

DOI: **https://doi.org/10.1039/D0MA00652A**

Title: **Multifunctional Properties and Multi-Energy Storage in the [(CH₃)₃S][FeCl₄] Plastic Crystal.**

Authors: **Salgado-Beceiro, J.**; Bermúdez-García, J. M.; Llamas-Saiz, A. L.; Castro-García, S.; Señarís-Rodríguez, M. A.; Rivadulla, F.; Sánchez-Andújar, M.

Reference: *Journal of Materials Chemistry C*, **2020**, *8*, 13686–13694.

DOI: **https://doi.org/10.1039/D0MA00652A**
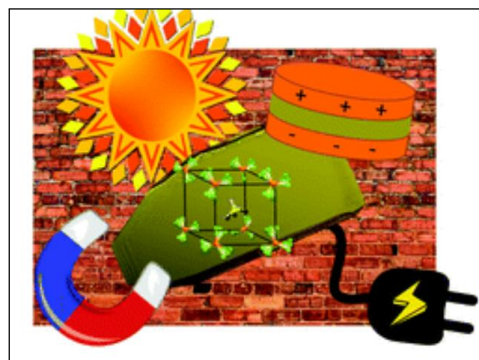
Title: **Raman Spectroscopy Studies on the Barocaloric Hybrid Perovskite [(CH₃)₄N][Cd(N₃)].**

Authors: Silva, R. X. D.; Paschoal, C. W. D. A.; Santos, C. C. D.; García-Fernández, A.; **Salgado-Beceiro, J.**; Señarís-Rodríguez, M. A.; Sanchez-Andujar, M.; Silva, A. N. A. D. A.

Reference: *Molecules* **2020**, 25 (20).

DOI: **10.3390/molecules25204754**
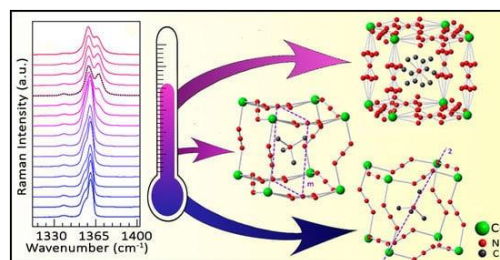
Title: **((R)-(−)-3-hydroxyquinuclidium)[FeCl₄]; A Plastic Hybrid Compound with Chirality, Multiaxial Ferroelectricity and Long Range Magnetic Ordering.**

Authors: Gonzalez-Izquierdo, P.; Fabelo, O.; Canadillas-Delgado, L.; Beobide, G.; Vallcorba, O.; **Salgado-Beceiro, J.**; Sánchez-Andújar, M.; Martin Gandul, C.; Ruiz-Fuertes, J.; Garcia, J. E.; Fernandez-Diaz, M. T.; de Pedro, M.

Reference: *J. Mater. Chem. C,* **2021**, 9(13).
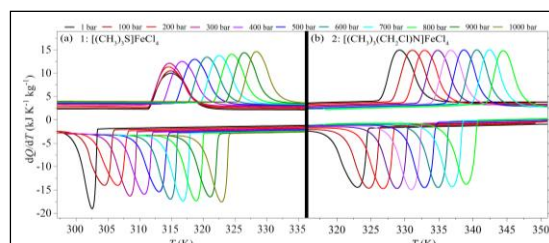
DOI: **https://doi.org/10.1039/D0TC05800A**
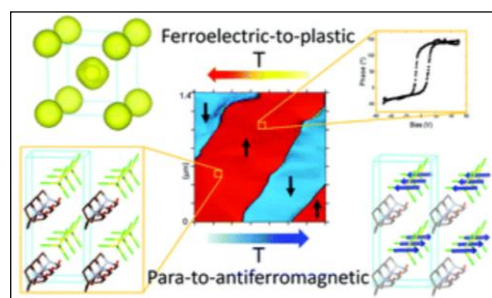
Title: **Hybrid ionic plastic crystals in the race for enhanced low-pressure barocaloric materials.**

Authors: **Salgado-Beceiro, J.**; Bermúdez-García, J. M.; Stern-Taulats, E.; García-Ben, J.; Castro-García, S.; Sánchez-Andújar, M.; Moya, X.; Señarís-Rodríguez, M. A.

Reference: *ChemRxiv ,* **2021** (pre-print).

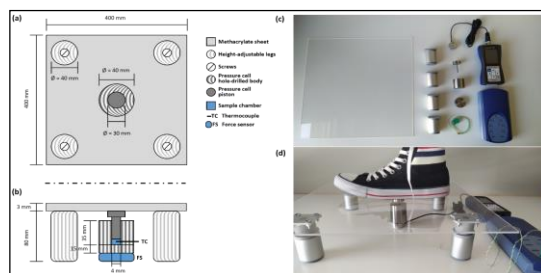DOI: **https://doi.org/10.33774/chemrxiv-2021-c4hx5**

Title: **Simple and low-cost footstep energy-recover barocaloric heating and cooling device.**

Authors: García-Ben, J.; Delgado-Ferreiro, I.; **Salgado-Beceiro, J.**; Bermúdez-García, J. M.

Reference: *Materials*, **2021**, 14(20), 5947

DOI: **http://dx.doi.org/10.3390/ma14205947** .

3. Communications

Poster communication: **Electron Spin Resonance: an Extreme Sensitivity Technique to Study the Phase Transitions of the Plastic-Crystals.**

Authors: **Salgado-Beceiro, J.**; Castro-García, S.; Sánchez-Andújar, M.; Rivadulla, F.

Event: National congress - XXXVII Reunión Bienal de la Real Sociedad Española de Química, 2019, May 26-30, Donostia-San Sebastián, Spain.

Oral communication: **Unprecedented stoichiometry and broad-band photoluminiscent emission in [(CH$_3$)$_2$NH$_2$]$_7$Pb$_4$X$_{15}$ 2D-perovskite related hybrids.**

Authors: García-Fernández, A.; Bermúdez-García, J. M.; **Salgado-Beceiro, J.**; Cuquejo-Cid, A.; Llamas-Saiz, A. L.; Castro-García, S.; Sánchez-Andújar, M.

Event: International congress – 6th International Conference on Multifunctional, Hybrid and Nanomaterials, 2019, March 11-15, Sitges, Spain.

Poster communication: **Spin crossover transition with a giant barocaloric effect in an organic-inorganic material.**

Authors: **Salgado-Beceiro, J.**; Bermudez-García, J. M.; Kim, J.; Moya, X.; Arnosa-Prieto, A. Garcia-Ben, J.; García-Fernández, A.; López-Beceiro, J.; Artiaga, R.; Castro-Garcia, S.; Sanchez-Andujar, M.; Señarís-Rodríguez, M. A.

Event: International congress – European Materials Research Society (E-MRS) Fall Meeting , 2019, September 15-19, Warsaw, Poland.

Poster communication: **Multiferroic hybrid organic-inorganic perovskites with giant barocaloric effects.**

Authors: **Salgado-Beceiro, J.**; Bermudez-García, J. M.; Moya, X.; Nonato, A.; Xavier Silva, R.; García-Fernández, A.; López-Beceiro, J.; Artiaga, R.; Castro-Garcia, S.; Sanchez-Andujar, M.; Señarís-Rodríguez, M. A.

Event: International congress – European Materials Research Society (E-MRS) Fall Meeting , 2019, September 15-19, Warsaw, Poland.

Oral communication: **Design, synthesis and characterization of hybrid organic-inorganic materials for ecologic refrigeration applications.**

Authors: **Salgado-Beceiro, J.**

Event: International congress – 3-minute thesis competition of the European Materials Research Society (E-MRS) Fall Meeting , 2019, September 15-19, Warsaw, Poland.

Oral communication: **Solid-state materials for ecologic refrigeration.**

Author: **Salgado-Beceiro, J.**

Event: International communication contest – IV International Research Pitches Contest of the Compostela Group of Universities, 2020.

Awarded with the II prize.

Oral communication: **Polar Ionic Plastic Crystals for Multi-Energy Storage Applications.**

Authors: **Salgado-Beceiro, J.**; Walker, J.; García-Fernández, A.; Bermudez-García, J. M.; García-Ben, J.; Delgado-Ferreiro, I.; Castro-Garcia, S.; Sanchez-Andujar, M.; Cappel, U. B.;; Einarsrud, M. A.; Señarís-Rodríguez, M. A.

Event: International congress – European Materials Research Society (E-MRS) Fall Meeting , 2021, September 20-23, virtual conference.

4. Collaborations

Group | Department: *Functional Materials and Materials Chemistry* (FACET).

Institution | Country: Norges Teknisk-Naturvitenskaplige Universitet (**NTNU**) of Trondheim, **Norway.**

Activity: Part of this thesis was developed in collaboration with the FACET group during a 3-month predoctoral stay from March 1st to June 1st 2021. It was a virtual stay, in the context of a special arrangement for the emergency due to de COVID-19 situation that occurred during the corresponding months in Norway and Spain. During this stay, electrical properties were measured and discussed. Part of the results are included in this doctoral thesis and, in addition to more results, are expected to be published in future works.

Chapter with results included: **5**.

Group | Department: BM01, *Swiss Norwegian Beam line* (SNBL).

Institution | Country: European Synchrotron Radiation Facility (**ESRF**), **France.**

Activity: X-ray powder diffraction measurements with variable temperature were carried out in the line used by the FACET group of the NTNU.

Chapter with results included: **5**.

Group | Department: BL04, *Materials Sience and Powder Diffraction* (MSPD) beamline.

Institution | Country: Synchrotron, **Spain**.

Activity: X-ray powder diffraction measurements with variable temperature were carried out in this line.

Chapter with results included: **2** .

Group | Department: *Department of Materials Science & Metallurgy.*

Institution | Country: **Cambridge University, United Kingdom.**

Activity: Differential scanning calorimetry measurements with variable pressure.

Chapters with results included: **2** and **4** .

Group | Department: *Condensed Matter and Materials Physics.*

Institution | Country: **Queen Mary University of London, United Kingdom.**

Activity: Differential scanning calorimetry measurements with variable pressure.

Chapters with results included: **5**.

Group | Department: *Coordenação de Ciências Naturais.*

Institution | Country: **Universidade Federal do Maranhão, Brazil.**

Activity: synthesis and discussion on hybrid organic-inorganic perovskites.

Chapters with results included: **2**.

Group | Department: *Network of Infrastructures to Support Research and Technological Development* (RIAIDT)*.*

Institution | Country: **Universidade de Santiago de Compostela, Spain.**

Activity: measurements and analysis of single-crystal x.ray diffraction data.

Chapters with results included: **3**.

Group | Department: *Physical Chemistry department.*

Institution | Country: **Universidade de Santiago de Compostela, Spain.**

Activity: measurements and analysis of electron spin resonance data and magnetic properties.

Chapters with results included: **3**.